*C*ontents

Articles

News Briefs

Journal of Research of the National Institute of Standards and Technology

System for Measuring Conditional Amplitude, Phase, or Time Distributions of Pulsating Phenomena

Richard J. Van Brunt and Eric W. Cernyar

National Institute of Standards and Technology, Gaithersburg, MD 20899

A detailed description is given of an electronic stochastic analyzer for use with direct "real-time" measurements of the conditional distributions needed for a complete stochastic characterization of pulsating phenomena that can be represented as random point processes. The measurement system described here is designed to reveal and quantify effects of pulse-to-pulse or phase-to-phase memory propagation. The unraveling of memory effects is required so that the physical basis for observed statistical properties of pulsating phenomena can be understood. The individual unique circuit components that comprise the system and the combinations of these components for various measurements, are thoroughly documented. The system has been applied to the measurement of pulsating partial discharges generated by applying alternating or constant voltage to a discharge gap. Examples are shown of data obtained for conditional and unconditional amplitude, time interval, and phase-of-occurrence distributions of partial-discharge pulses. The results unequivocally show the existence of significant memory effects as indicated, for example, by the observations that the most probable amplitudes and phases-of-occurrence of discharge pulses depend on the amplitudes and/or phases of the preceding pulses. Sources of error and fundamental limitations of the present measurement approach are analyzed. Possible extensions of the method are also discussed.

1. Introduction

There are many types of naturally occurring pulsating phenomena that have statistical properties which have not yet been adequately explained. Included in this category of phenomena are certain types of nerve impulses, pulsating fluid flow and droplet formation, bursts of electromagnetic radiation from extraterrestrial sources, geological disturbances such as earth tremors, and pulsating electrical discharges specifically considered in this work. These phenomena may exhibit complex chaotic behavior manifested by an apparent high degree of randomness in the time of occurrence and magnitude of the impulse events. For some phenomena, the complexity of the impulse behavior may, in part, be a consequence of memory propagation between successive events. In developing a better understanding of the physical bases for pulsating phenomena, it is essential to assess the effects of memory propagation.

In the case of pulsating partial-discharge phenomena, it has already been shown that effects of memory propagation are significant [1–4]. Partial-discharge (PD) phenomena are of special interest because they are types of localized electrical discharges that occur at defect sites in electrical insulation. Partial discharges are often the precursors

to insulation failure and represent undesirable electrical noise sources under some conditions. The detection of PD pulses has been used to assess insulation performance and integrity [5]. It is also known [6, 7] that PD phenomena exhibit stochastic properties that depend on the nature of the defect site such as characterized by the types of materials present as well as their geometrical configuration. Partial discharges also produce physical or chemical changes in the characteristics of the defect sites (PD – induced aging) that in turn produce changes in the stochastic behavior of the discharge [8–11].

Efforts have been underway in numerous laboratories to quantify statistically PD patterns using computer-assisted measurement and analysis techniques [12–22]. The incentive for this work has been the development of so called "smart" PD detectors that employ pattern recognition to help identify the type of defect at which the PD occurs, e.g., to distinguish between a cavity in solid insulation and a metal particle in liquid or gaseous insulation. Unfortunately, progress in the development of reliable automated methods for PD pattern recognition has been hampered by a failure to understand the physical mechanisms that determine the stochastic properties of PD phenomena. In general, present computer assisted PD-measurement systems simply do not provide enough refined information about the stochastic properties of PD pulses for a meaningful analysis.

The purpose of the present work is to describe a real-time stochastic analyzer that can be used to quantify the stochastic behavior of a train of electrical pulses that may or may not be correlated with a periodic time varying excitation source, e.g., a sinusoidal voltage. The instrument described here is an extended version of one that was used to investigate the stochastic behavior of pulsating negative-corona discharges generated by applying a constant voltage to a point-plane electrode gap [1, 24, 25]. In addition to the conditional pulse-amplitude and time-separation distributions that could be measured with the previous system, the present system also allows measurement of a set of phase-restricted pulse-amplitude and phase-of-occurrence distributions. This latter capability makes the instrument suitable for investigating the stochastic behavior of partial discharges generated using alternating voltages. The data acquired from this system provide immediate determinations of the existence of pulse-to-pulse or phase-to-phase memory propagation effects.

The measurement system described here can be thought of as a type of electronic filter that is inserted between the impulse source and a computer-driven multichannel analyzer (MCA) in which data on the desired conditional or unconditional pulse distributions are accumulated. The unique features of the circuitry of this filter are documented here in enough detail to allow replication. The present system design incorporates standard commercially available nuclear-instrumentation components, where possible, such as time-to-amplitude converters and linear pulse amplifiers. Although the present system can be employed to investigate any type of pulsating phenomenon that can be converted to electrical signals, it was designed primarily for the measurement of relatively stationary PD-pulse phenomena generated by a constant or low-frequency alternating voltage. The system may not be well suited for investigations of impulses that have repetition rates much greater or less than the PD-phenomena considered here; and it will not perform well for phenomena that exhibit highly nonstationary behavior, i.e., phenomena for which the stochastic properties change rapidly with time.

The range of phenomena to which the present system can be applied is considered and the system's inherent limitations and sources of error are analyzed. Extensions of the technique and alternative approaches that rely primarily on analysis using computer software are discussed. Examples are presented of results obtained for partial discharges generated in a point-to-solid dielectric electrode gap.

2. Definitions

In this section we introduce the parameters that define the types of stochastic processes which can be investigated with the electronic measurement system described here. We also define the various conditional and unconditional distributions that are measured with this system and indicate how the measured distributions can be used to gain insight into the physical bases for the process under investigation.

2.1 Random Point Processes

The types of pulsating phenomena to be considered here are those that can be represented by a *marked random point process* as defined by Snyder [26]. In order to represent the phenomenon as a point process, the pulses must occur at discrete times that can be readily defined. In the case of a periodic time-varying excitation, the events of

interest must occur at discrete phases. This requires that an occurrence time (or phase) can be meaningfully associated with a particular property of the pulse such as its amplitude. Difficulties can be encountered in satisfying the criterion for a point process if, for example, there is significant variability in the shapes of the pulses or if there is the possibility that successive pulses can overlap or otherwise become indistinguishable. Ideally there should be a reasonable uniformity in pulse shapes and the mean spacing between pulses should be much greater than the pulse widths. The types of pulsating partial-discharge phenomena to which the present measurement system have been applied generally satisfy the requirements for a point process.

It is also assumed that the point process can be *marked* by some property of the pulse such as its amplitude, width, shape parameters, or area under the pulse. In order to consider the mark as a property of the pulse measured with the present system, it is necessary that the mark be converted to an electrical signal with a voltage that is proportional to the "size" of the mark. For reasons previously discussed [1, 27], the partial-discharge pulse amplitude has been selected here as an appropriate mark which is a measure of discharge magnitude. Since PD can be detected by different methods, e.g., optical, acoustical, and electrical [5], it is necessary to convert the observed response to an electrical signal as is normally done for purposes of recording data.

If the occurrence of the pulsating phenomenon is correlated with an externally controlled time-varying excitation process such as a chopped light beam or, as is sometimes the case for PD pulses, a sinusoidal voltage, then it may be more convenient to specify the time of pulse occurrence relative to the times of the external excitation processes. For PD-pulses generated with an alternating sinusoidal voltage, it is desirable to consider the *phase-of-occurrence* of a pulse as defined by the phase of the corresponding applied voltage at the time of PD-initiation.

The point processes under consideration here are assumed to be *random* in the sense that both the times-of-occurrence and the marks can exhibit statistical variability, e.g., it is not possible to predict precisely when a given pulse will occur or what its amplitude will be. For processes excited by a well-defined controllable periodic source, it is also possible to define point processes that are fixed in time or phase but exhibit statistical variability in the mark. Such a process might be, for example,

the sum of the areas under all PD pulses that occur in a specified phase interval of the applied voltage. The sum could be recorded at a fixed phase immediately following the time lapse of the phase interval. The measurement system described in this work allows determination of such phase-restricted sums of pulse areas or amplitudes.

2.2 Measurable Quantities for a PD Process (Random Variables)

The type of marked random point process under consideration here is a stochastic process specified by a countable set of discrete *random variables* of which time-of-occurrence (or equivalently phase-of-occurrence) is one of the variables. In this section we define the sets of random variables that apply to the measurement of pulsating partial discharges generated either with a constant applied voltage (dc) or an alternating (sinusoidal) applied voltage (ac).

2.2.1 Random Variables for a dc-Excited PD Process

A diagrammatic representation of a dc-generated PD process is shown in Fig. 1. As previously discussed [1, 24, 25], this process can be specified by the finite set $\{q_i, t_i\}_n$, $i = 1, 2, ..., n$ where q_i is the amplitude of the ith PD pulse (usually expressed in units of picocoulombs) and t_i is the time at which this pulse occurs. The measurement system described here records time separations between successive PD events rather than actual occurrence times. It is therefore more convenient to specify the process in terms of the set of random variables $\{q_1, q_i, \Delta t_{i-1}\}_n$, $i = 2, ..., n$, where $\Delta t_{i-1} = t_i - t_{i-1}$ is the time separation between the $(i-1)$th and ith events. To satisfy the requirements for a point process, it is desirable that the mean duration of the PD events, as measured, for example, by the pulse widths, δt_i, be much smaller than the mean time separation between successive events, i.e., $\langle \Delta t_i \rangle \gg \langle \delta t_i \rangle$ for all values of i. If all time intervals are recorded, the time-of-occurrence of any pulse can simply be determined from the sum

$$t_i = \sum_{j=1}^{i-1} \Delta t_j. \qquad (1)$$

As will be seen from the discussion below, data on the time separations between events are needed to assess pulse-to-pulse memory propagation effects. If memory effects are important, the random variables associated with the amplitudes and time

separations of successive pulses are not independent, e.g., the amplitude of any given pulse can depend on the time separation between that pulse and the previous pulse.
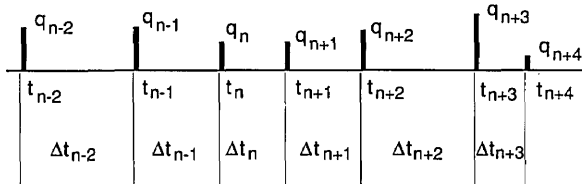
Fig. 1. Diagrammatic representation of a marked random point process. Shown are pulses "marked" with amplitudes $q_j, j = n - 2, n - 1, ...$, that occur at discrete times t_j with corresponding time separations Δt_j.

2.2.2 Random Variables for an ac-Excited PD Process

If the PD process is generated with an alternating voltage, it becomes more convenient to specify the *phase-of-occurrence* of the PD pulse rather than the time-of-occurrence. An example of an ac-generated PD process is shown by the diagram in Figs. 2a and 2b. The excitation voltage indicated in Fig. 2a is assumed to be sinusoidal and is given by

$$V_a(t) = V_0 \sin(\omega t) = V_0 \sin[\phi(t)] , \qquad (2)$$

where $\omega/2\pi$ is the frequency, $\phi(t) = \omega t$ the phase, and V_0 is the amplitude. The individual PD events are specified by the set of random variables

$$\left\{ q_{ij}^{\pm}, \phi_{ij}^{\pm} \right\}_{n,m} , \quad i = 1,2,...,n; \quad j = 1,2,...,m , \text{ where}$$

q_{ij}^{+} and q_{ij}^{-} are the amplitudes of the ith pulses to appear respectively in the jth positive and negative half-cycles of the applied voltage and ϕ_{ij}^{+} and ϕ_{ij}^{-} are their corresponding phases-of-occurrence. The phases $\phi_{ij}^{\pm}$ are restricted by definition to lie within the interval $(0, 2\pi)$ for arbitrary j and are thus related the phase at time t by $\phi(t) = \phi_{ij}^{\pm} + 2\pi(j - 1)$.

The amplitudes for q_{ij}^{+} and q_{ij}^{-} are observed to be of opposite signs as indicated in Fig. 2b. In some cases, as previously explained [3, 4], the occurrence of positive and negative PD pulses may be phase shifted relative to the positive and negative half-cycles, e.g., it may be possible for negative pulses to occur before the zero-crossing where the voltage is still positive. This is phyiscally a consequence of a fluctuating phase lag in the local electric-field strength at the discharge site. The phase shift will

be denoted here by $\delta\phi$, and is arbitrarily adjusted to a value such that

$$\phi_{ij}^{+} \in (-\delta\phi, \pi - \delta\phi), \quad \phi_{ij}^{-} \in (\pi - \delta\phi, 2\pi - \delta\phi) \qquad (3)$$

for all values of i and j.
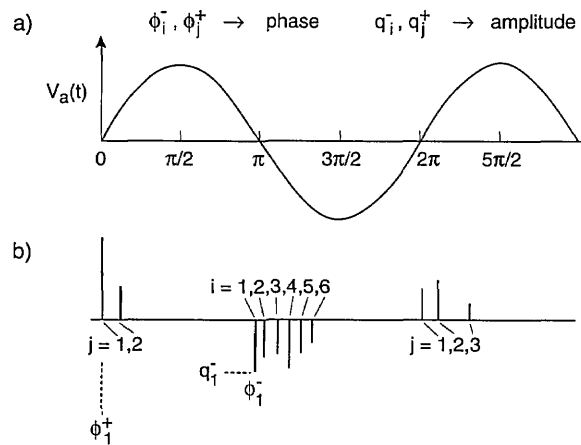
Fig. 2. Diagrammatic representation of an ac-excited partial discharge process: a) sinusoidal excitation voltage, b) phase-correlated PD pulses.

As in the case of dc-generated PD pulses, it may also be useful to specify the phase differences between successive events within a half-cycle. These phase differences will be denoted by $\Delta\phi_{i,i-1,j}^{\pm} \equiv \phi_{i,j}^{\pm} - \phi_{i-1,j}^{\pm}$ where $i \geq 2$.

For some types of ac-generated PD processes, especially those that occur in the presence of solid dielectric surfaces, it is valuable in assessing phase-to-phase memory propagation effects to know the accumulated PD charge associated with each half-cycle as defined by

$$Q_j^{\pm} = \sum_i q_{ij}^{\pm} , \qquad (4)$$

where the summation is over amplitudes of all pulses that occur within a given half-cycle as specified by their phases-of-occurrence defined in Eq. (3).

It is possible with the system described here, and sometimes necessary, to record the number of individual voltage cycles. This is necessary if an assessment is to be made of memory propagation that extends back beyond the previous cycle. For most types of measurements described here however,

this information is not recorded. If no attempt is made to record the number of a given cycle, then the subscript j can be dropped from the specification of the random variables that define the stochastic process for ac-generated PD. In this case, the appropriate designation of the random variables is $q_i^\pm$, $\phi_i^\pm$, $\Delta\phi_{i,i-1}^\pm$, and $Q^\pm$. A failure to include the subscript on the variable $Q^\pm$ will imply by default that the sum given by Eq. (4) applies to the half-cycle immediately preceding that in which the variables $q_i^\pm$, $\phi_i^\pm$, are measured.

In performing the measurement of an ac-generated PD process, it is assumed that the excitation voltage given by Eq. (2) is instrumentally filtered out or otherwise subtracted from the PD signals. This is necessary to ensure that the recorded pulse amplitude is a true measure of the discharge intensity.

2.3 Measurable Conditional and Unconditional Distributions

2.3.1 Unconditional Distributions

Because the variables such as pulse amplitude and phase-of-occurrence that describe the pulsating phenomenon (PD process) of interest are random, they can only be specified quantitatively in terms of statistical probability distributions. The unconditional probability distribution $p_\xi(x)$ (sometimes referred to as the probability density function [28]) for a random variable, ξ, is defined such that $p_\xi(x)$ dx is the probability that ξ will assume a value that lies in the interval x to $x + dx$. Here ξ can be any of the random variables that were defined in the previous section.

Consistent with our earlier work [1, 24], we shall adopt the abbreviated notation for distribution functions whereby $p_\xi(x)$ dx is replaced by $p_0(\xi)$ dξ. Thus, for example, $p_0(q_n)$ dq_n is the probability that the nth pulse has amplitude between q_n and $q_n + dq_n$. There is no ambiguity in this notation if it is understood that the symbol used to designate the value of a random variable is the same as that used to define the variable.

The distribution $p_0(\xi)$ is *unconditional* in the sense that it gives the probability that the random variable will have a particular value independent of the past history of the process, e.g., independent of values for random variables associated with previous events. The random variables, as defined here, correspond to particular discrete events in time associated with the random point process, i.e., $\xi = q_n$, Δt_{n-1}, ϕ_n, where the subscript n is assigned

to the nth event. In cases where the events are not actually counted by the measurement process, the distributions such as $p_0(q_n)$ and $p_0(\Delta t_n)$ are assumed to apply to arbitrary n. If events are counted relative to a specified time, then n is assigned a value, e.g., $p_0(q_2^+)$ is the amplitude distribution of the second pulse to appear in an arbitrary positive half-cycle of the excitation voltage.

2.3.2 Conditional Distributions

If memory effects are important in a pulsating process, then the probabilities that the random variables associated with a particular event will have specific values depend in general on the values for these variables that were assumed by previous events. The probability that the jth PD pulse will have values for amplitude and time separation that lie in the ranges q_j to $q_j + dq_j$ and Δt_{j-1} to $\Delta t_{j-1}+d(\Delta t_{j-1})$ can depend on values of all previous q_i and Δt_{i-1} where $i <j$. The existence of memory effects can be established by the measurement of *conditional* probability distributions. The system to be described here allows measurement of a set of conditional distributions for such variables as pulse amplitude and phase-of-occurrence.

The conditional distribution $p_1(q_j|\Delta t_{j-1})$ is defined such that $p_1(q_j|\Delta t_{j-1})$ is the probability that the jth pulse has an amplitude in the range q_j to $q_j + dq_j$ if its time separation from the previous pulse has a *fixed* value Δt_{j-1}. With the system described here, it is also possible to measure higher order conditional distributions such as $p_2(q_j|\Delta t_{j-1},\Delta t_{j-2})$, where $p_2(q_j|\Delta t_{j-1},\Delta t_{j-2})dq_j$ is the probability that the amplitude of the jth pulse is in the range q_j to $q_j + dq_j$ if *both* Δt_{j-1} and Δt_{j-2} are fixed. Lists of the conditional distributions that can be measured for dc and ac-generated PD pulses are given respectively in Tables 1 and 2.

Table 1. Measurable conditional and unconditional pulse-amplitude and time-separation distributions for a constant excitation process (dc-generated PD)

Distribution type	Amplitude distribution	Time-separation distribution
Unconditional	$p_0(q_j)$	$p_0(\Delta t_j)$
First-order conditional	$p_1(q_j\|\Delta t_{j-1})$ $p_1(q_j\|q_{j-1})$ $p_1(q_j\|\Delta t_{j-k}),k>1$	$p_1(\Delta t_j\|\Delta t_{j-1})$ $p_1(\Delta t_j\|q_j)$
Second-order conditional	$p_2(q_j\|\Delta t_{j-1},q_{j-1})$ $p_2(q_j\|\Delta t_{j-1},\Delta t_{j-2})$	

Table 2. Measurable conditional and unconditional pulse-amplitude and phase distributions for a periodic, time varying excitation process (ac-generated PD)

Distribution type	Amplitude distribution	Phase distribution	Pulse number and cycle specifications
Unconditional (unspecified event)	$p_0(q_i^{\pm})$	$p_0(\phi_i^{\pm})$	all, $i \geq 1$
Unconditional (specified event)	$p_0(q_i^{\pm})$	$p_0(\phi_i^{\pm})$	$i = 1,2,3,\ldots$
First-order conditional	$p_1(q_i^{\pm} \mid \Delta\phi^{\pm})$ $p_1(q_i^{\pm} \mid \phi_i^{\pm})$ $p_1(q_{ij}^{\pm} \mid Q_k^{\pm})$ $p_1(q_i^{\pm} \mid \Delta\phi_{i,j-1}^{\pm})$	$p_1(\phi_i^{\pm} \mid \phi_{i-1}^{\pm})$ $p_1(\phi_{ij}^{\pm} \mid Q_k^{\pm})$	$\phi_i^{\pm} \in \Delta\phi^{\pm}$, all, $i \geq 1$ $i = 1,2,3\ldots$ $i = 1,2,3\ldots$ $+ \rightarrow k = j, j-1,\ldots$ $- \rightarrow k = j-1, j-2,\ldots$ $i = 2,3,4,\ldots$
Second-order conditional	$p_2(q_i^{\pm} \mid \phi_{i-1}^{\pm}, q_{i-1}^{\pm})$ $p_2(q_{ij}^{\pm} \mid \phi_{ij}^{\pm}, Q_k^{\pm})$	$p_2(\phi_i^{\pm} \mid \phi_{i-1}^{\pm}, q_{i-1}^{\pm})$	$i = 2,3,4,\ldots$ or all $i \geq 2$ $i = 1,2,3,\ldots$ $+ \rightarrow k = j, j-1,\ldots$ $- \rightarrow k = j-1, j-2,\ldots$
Third-order conditional	$p_3(q_i^{\pm} \mid \phi_i^{\pm}, q_{i-1}^{\pm}, \phi_{i-1}^{\pm})$	$p_3(\phi_{ij}^{\pm} \mid \phi_{i-1,j}^{\pm}, q_{i-1,j}^{\pm}, Q_k^{\pm})$	$i = 2,3,4\ldots$ $+ \rightarrow k = j, j-1,\ldots$ $- \rightarrow k = j-1, j-2,\ldots$

Determination of the conditional distributions such as $p_1(q_j \mid \Delta t_{j-1})$ provides an indication of the dependence of the random variable q_j on Δt_{j-1}. If memory effects are important, then the probability that q_j will assume a particular value can depend on the value chosen for Δt_{j-1}. In this case, the conditional distribution, $p_1(q_j \mid \Delta t_{j-1})$, will not equal the unconditional distribution, $p_0(q_j)$, for at least some allowed values of Δt_{j-1}.

A quantitative assessment of memory propagation can be made from calculation of *expectation values* using measured conditional distributions. For example, the expectation value for the phase-of-occurrence of the third pulse in a negative half-cycle of the applied excitation voltage conditioned on a fixed value for the sum of all PD pulse amplitudes in the previous positive half-cycle is defined by

$$\langle \phi_3^-(Q^+) \rangle = \int_{\pi-\delta\phi}^{2\pi-\delta\phi} \phi_3^- p_1(\phi_3^- \mid Q^+) \, d\phi_3^- , \quad (5)$$

where it is assumed that ϕ_3^- must be confined to the interval defined by Eq. (3). In general,

$$\langle \xi_i(\{a_k\}_n) \rangle = \int_R \xi_i p_n(\xi_i \mid \{a_k\}_n) \, d\xi_i, \quad (6)$$

where ξ_i is any random variable associated with the ith pulse and $\{a_k\}_n$ is a set of fixed values for n random variables associated with one or more pulses that occurred at earlier times. The integral in Eq. (6) is over all allowed values of ξ_i that are assumed to lie within a range R, i.e., $\xi_i \in R$.

If memory effects are important, the value of $\langle \xi_i(\{a_k\}_n) \rangle$ will change as one or more of the values a_k are changed. If the value of $\langle \xi_i(\{a_k\}_n) \rangle$ increases as $a_l \in \{a_k\}_n$ increases within a particular range $(a_l \in A_l)$, then ξ_i is said to be *positively dependent* on a_l in that range for fixed values of a_k $(k \neq l)$. Consistent with our earlier notation [1], this dependence is denoted by $(a_l \uparrow \Rightarrow \xi_i \uparrow, \{a_k, k \neq l\})$ when $a_l \in A_l$. Likewise ξ_i can be *negatively dependent* on a different variable or on a_l in a different range A_l'. In this case, the negative dependence is denoted by $(a_l \uparrow \Rightarrow \xi_i \downarrow, \{a_k, k \neq l\})$ when $a_l \in A_l'$. The dependence of the expectation values for random variables on the values of random variables associated with prior events can often be predicted from physical models of the process as has been done for the case of negative corona (Trichel) type partial-discharge pulses [1].

If memory effects are important in the pulsating phenomenon, then the various distributions listed in Tables 1 and 2 are not necessarily independent. It can be shown, for example, from the law of probabilities that the distributions $p_0(q_j)$, $p_0(\Delta t_{j-1})$, and $p_1(q_j|\Delta t_{j-1})$ are related by the integral expression

$$p_0(q_j) = \int_0^\infty p_0(\Delta t_{j-1}) p_1(q_j|\Delta t_{j-1})\, d(\Delta t_{j-1}). \quad (7)$$

Similarly the distributions $p_0(\phi_i^\pm)$, $p_0(Q^\pm)$, and $p_1(\phi_i^\pm|Q^\mp)$ are related by

$$p_0(\phi_i^\pm) = \int_0^\infty p_0(Q^\mp) p_1(\phi_i^\pm|Q^\mp)\, dQ^\mp. \quad (8)$$

It has previously been shown [1] that there may be many other integral expressions that connect the different conditional and unconditional measurable distributions. Equations (7) and (8) can be used to check the consistency among the various measured distributions. For example, if data are obtained on the three distributions $p_0(q_j)$, $p_0(\Delta t_{j-1})$, and $p_1(q_j|\Delta t_{j-1})$, then one should, if possible, verify that they satisfy Eq. (7). There may be some cases, however, where it is not possible to obtain enough data at high enough resolution to perform this analysis.

In the process of measuring a conditional distribution it is generally not possible to select a single value for the "fixed" variable. This variable can only be specified experimentally to lie within a finite window. In the case of the distribution $p_1(\phi_i^-|Q^+)$, for example, one really measures an approximation to this distribution given by

$$P_1(\phi_i^-|Q^+) = \int_{Q^+ - \delta Q^+}^{Q^+ + \delta Q^+} p_0(Q'^+) p_1(\phi_i^-|Q'^+)\, dQ'^+ \quad (9)$$

where Q'^+ is defined by the measurement to lie within the window corresponding to the interval $(Q^+ - \delta Q^+, Q^+ + \delta Q^+)$. The measured conditional distribution approaches the "true" conditional distribution as the window is made smaller, e.g.,

$$P_1(\phi_i^-|Q^+) = \lim_{\delta Q^+ \to 0} p_1(\phi_i^-|Q^+ \pm \delta Q^+).$$

The errors associated with finite window size have previously been noted [24] and will be discussed again later in this work.

All conditional distributions satisfy the normalization requirement

$$\int_R p_n(\xi_i|\{a_k\}_n)\, d\xi_i = 1. \quad (10)$$

Measured data for conditional distributions are generally normalized according to this requirement by numerical integration. In some cases, it may be convenient for display purposes to normalize to the maximum of the distribution.

3. Measurement System

In this section we describe the general features of the system for measuring the conditional and unconditional distributions listed in Tables 1 and 2. The system can be configured to investigate either a continuous train of pulses produced by a constant excitation process, e.g., dc-generated PD or pulses generated by periodic, time-varying process, e.g., ac-generated PD. Thus, the system is an extended version of that previously described for measurement of dc-generated PD [1, 24, 25], and, in fact, includes all of the features of the earlier system. We shall treat the ac and dc measurement configurations separately even though they both utilize some of the same individual circuit components.

3.1 Configurations for a Continuous Excitation Process (dc-Generated PD)

The configurations of the electronic system used to measure the distributions listed in Table 1 for a dc-generated PD process have been described previously [1, 24, 25], a block diagram indicating the circuit components utilized for this case is shown in Fig. 3. The configurations of the components that are required for the measurement of each distribution are specified by the various switch configurations listed in Table 3 where $S1$–$S7$ are the switches designated in Fig. 3 and the notation $a1 = b1$ implies, for example, that position $a1$ of $S1$ is connected to position $b1$ of $S1$.

The system indicated in Fig. 3 differs from that used previously mainly in the design of the individual circuit components that will be described in the next section. The most significant changes have been in the design of the Δt control logic circuits (parts A and B). Although their basic function and operation are the same as previously described [1, 24], changes were made that reduce errors,
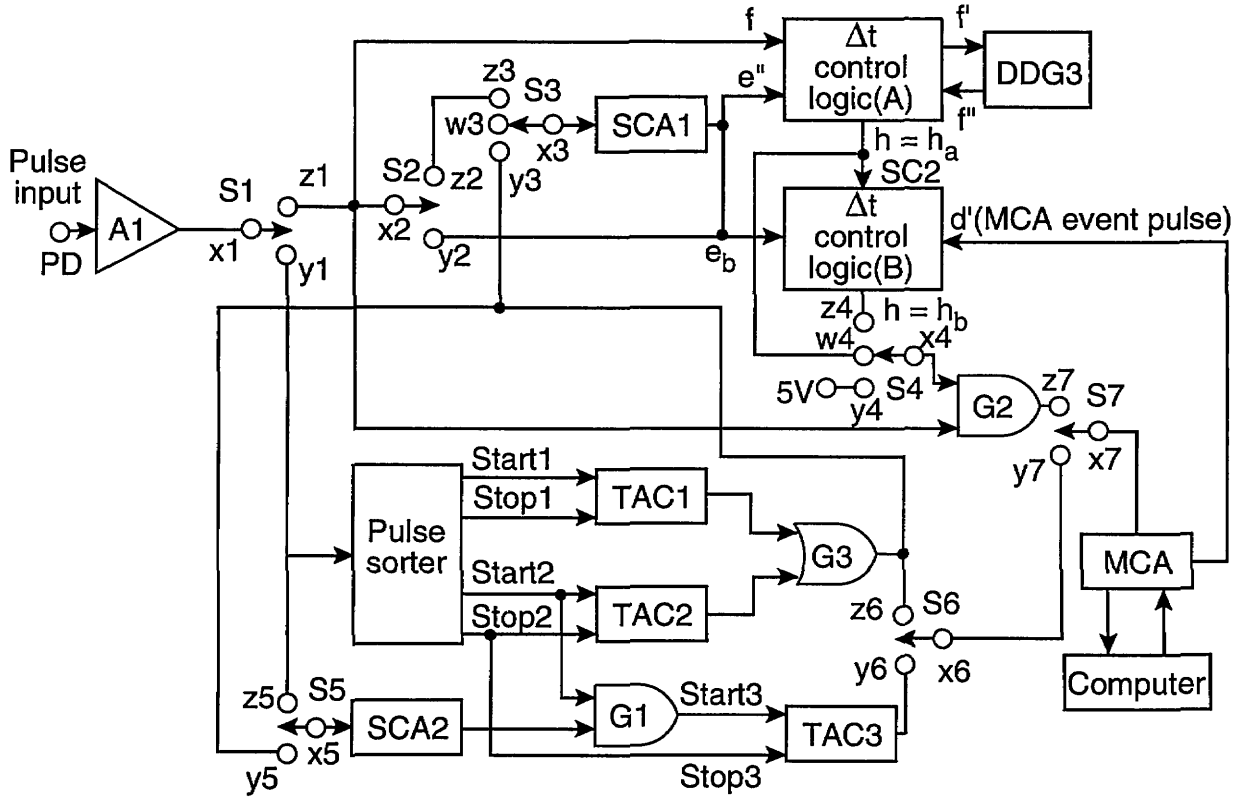
Fig. 3. System for measuring unconditional and conditional pulse-amplitude and time-separation distributions for a continuous or dc excited point process such as shown in Fig. 1. A = amplifier, DDG = digital delay generator, TAC = time-to-amplitude converter, SCA = single-channel analyzer, MCA = multichannel analyzer, G = gate, S = switch.

Table 3. Configuration of switch connections for the system shown in Fig. 3 that are required for measurement of the various conditional and unconditional pulse-amplitude and time-interval distributions for a constant excitation process

Distribution	S1	S2	S3	Switch S4	S5	S6	S7
$p_0(q_j)$	x1=z1	*	*	x4=y4	*	*	x7=z7
$p_1(q_j\|\Delta t_{j-1})$	x1=z1	x2=y2	x3=w3	x4=x4	*	*	x7=z7
$p_1(q_j\|\Delta t_{j-k}),k>1$	x1=z1	x2=y2	x3=w3	x4=z4	*	*	x7=z7
$p_2(q_j\|\Delta t_{j-1},q_{j-1})$	x1=z1	x2=z2	x3=z3	x4=w4	*	*	x7=z7
$p_2(q_j\|\Delta t_{j-1},\Delta t_{j-2})$	x1=z1	x2=z2	x3=y3	x4=w4	*	*	x7=z7
$p_0(\Delta t_j)$	x1=y1	*	*	*	*	x6=z6	x7=y7
$p_1(\Delta t_j\|\Delta t_{j-1})$	x1=y1	*	*	*	x5=z5	x6=y6	x7=y7
$p_1(\Delta t_j\|q_j)$	x1=y1	*	*	*	x5=y5	x6=y6	x7=y7

* Switch position irrelevant.

improve performance, and eliminate redundancies. Some of these changes have already been utilized in the investigation of Trichel pulses [1], but have never been documented in detail.

The pulse sorter circuit that drives the time-to-amplitude converters (TACs) and the analog gate G3 that accepts the outputs of the TACs remain unchanged. The TACs, digital-delay generator (DDG) and the 256-channel multichannel analyzer (MCA) are commercially available instruments. The commercial single-channel analyzers (SCAs) have been replaced with a circuit to be described in the next section.

The operating principles of the system shown in Fig. 3 have been discussed already in previous publications. This configuration allows the recording of either pulse amplitudes or pulse time separations with a computer controlled MCA. The MCA employs a fast analog-to-digital converter to digitize the voltage amplitude of pulses received at its input provided the amplitude is above a preset discrimination level. If the MCA is set by switch S7 to measure pulse amplitudes, then the input signals are derived from a linear pulse amplifier, A1, after passing through the analog gate G2. This gate is a built-in feature of the MCA. If time intervals are recorded, then the MCA input is derived from the output of one or more TACs. The output of the TAC is a narrow pulse with an amplitude that is directly proportional to the time between the start and stop pulses that are applied respectively to the "start" and "stop" inputs. For the measurement of the unconditional amplitude and time separation distributions ($p_0(q_j)$ and $p_0(\Delta t_j)$), the gate G2 is held continuously open by positioning switch S4 such that x4 = y4.

The measurement of conditional pulse-amplitude distributions requires the use of the Δt control logic circuits and the digital-delay generator DDG3. For the measurement of the first-order conditional distribution $p_1(q_j|\Delta t_{j-1})$, the gate, G2, to the MCA is enabled by the output of the Δt control logic (part A) for a time interval $\Delta t_{j-1} \pm \delta(\Delta t_{j-1})$ after the $j-1$ th pulse, provided no pulse from A1 occurs within the interval $2\delta(\Delta t_{j-1})$ starting from the $j-1$ th pulse. The time delay, Δt_{j-1} and window $\pm\delta(\Delta t_{j-1})$ are determined respectively by the settings of the DDG3 delay and pulse width. The $j-1$ th pulse essentially triggers DDG3 after passing through the Δt control logic (part A). The DDG3 then returns a 5 V logic pulse of preset delay and width which is in turn transferred to G2 if no other pulses have appeared at the input f. Details of the Δt control logic circuit operation are given in the next section.

The measurement of the distributions $p_1(q_j|\Delta t_{j-i})$, where $i > 1$ and Δt_{j-i} is the interval between the $j-i$ th and $j-i+1$ th events, requires the use of both parts A and B of the Δt control logic circuit. The value of i is determined by a selectable pulse counter inherent to the Δt control logic (part B) as described in the next section. The time interval Δt_{j-i} is selected by part A of the Δt control logic in conjunction with DDG3 as in the case of the $p_1(q_j|\Delta t_{j-1})$ measurement. The output of part A is then used to trigger part B. If a pulse appears at the input e_b of part B within the time

interval $\Delta t_{j-i} \pm \delta(\Delta t_{j-i})$, then the gate G2 to the MCA is enabled either immediately for measurement of $p_1(q_j|\Delta t_{j-2})$ or after $i-2$ pulses have been counted for measurement of $p_1(q_j|\Delta t_{j-i})$, $i > 2$. The next pulse to appear after G2 is enabled will be recorded by the MCA which then returns an "event pulse" to reset part B of the Δt control logic. The next input pulse time interval to lie within the range $\Delta t_{j-i} \pm \delta(\Delta t_{j-i})$ will start the process over again.

The second-order conditional pulse-amplitude distributions, $p_2(q_j|\Delta t_{j-1},q_{j-1})$ and $p_2(q_j|\Delta t_{j-1},\Delta t_{j-2})$ can be measured by using a single-channel analyzer, SCA1, the output of which is connected to input e" of the Δt control logic circuit (Part A). Depending on the position of switch S1, SCA1 receives a pulse either directly from amplifier A1 or from the output of TAC1 for measurement of $p_2(q_j|\Delta t_{j-1},q_{j-1})$ and $p_2(q_j|\Delta t_{j-1},\Delta t_{j-2})$ respectively. In the first case, the Δt control logic and subsequently DDG3 are only triggered if the amplitude of q_{j-1} lies within a narrow range selected by SCA1. In the second case, it is triggered only if the output pulse of TAC1, the amplitude of which is proportional to Δt_{j-2}, lies within a narrow range corresponding to $\Delta t_{j-2} \pm \delta(\Delta t_{j-2})$ as selected again by SCA1.

The first-order distribution $p_1(q_j|q_{j-1})$ can be measured using the configuration for measurement of $p_2(q_j|\Delta t_{j-1},q_{j-1})$ and selecting the time window $\delta(\Delta t_{j-1})$ from DDG3 to be large compared to the mean time separation between pulses, i.e., $\delta(\Delta t_{j-1}) \gg \langle \Delta t_{j-1} \rangle$. Although it is possible to measure directly other types of conditional amplitude distributions with this system [24] such as $p_1(q_j|\Delta t_{j-1} + \Delta t_{j-2})$, these are derivable from the distributions listed in Table 1, hence are considered difficult to interpret and less useful in revealing stochastic properties of the process.

Measurement of the unconditional time-separation distribution, $p_0(\Delta t_j)$, requires use of two time-to-amplitude converters (TAC1 and TAC2) connected to a pulse sorter. As previously shown, [24] this arrangement allows measurement of all successive time separations if all the time separations are greater than the TAC reset time. The reset time for the TACs used in the present measurement system is 50 μs. Failure to sample all time separations can lead to errors in the measurement of $p_0(\Delta t_j)$ under some conditions as will be discussed later [24].

Measurement of the conditional time-separation distributions involves use of the single-channel analyzer SCA2 that is either connected at S5

directly to A1 for measurement of $p_1(\Delta t_j | q_j)$ or to the output of TAC1 for measurement of $p_1(\Delta t_j | \Delta t_{j-1})$. The output of SCA2 enables gate G1 for measurement of Δt_j with TAC3 provided either q_j or Δt_{j-1} lie within the windows selected by SCA2. The gate G1 is actually a built-in feature of the time-to-amplitude converter circuit used in the present system.

3.2 Configuration for a Periodic Time-Varying Excitation Process (ac-Generated PD)]

A diagram of the system configuration used for measurement of the distributions listed in Table 2 is shown in Fig. 4. Although it is assumed here for convenience and simplicity that the excitation process for the observed pulses is sinusoidal as given by Eq. (2), this is not a requirement for the measurement method. It is only required that the excitation process have a well defined periodicity

so that phase position and intervals can be meaningfully specified. Thus, excitation processes that can be represented by a Fourier expansion are also acceptable, e.g., voltages of the form

$$V_a(t) = C_0 + \sum_{n=1}^{\infty} A_n \cos(n\omega t) + \sum_{n=1}^{\infty} B_n \sin(n\omega t),$$

(11)

where C_0 is a constant and A_n and B_n are the usual Fourier expansion coefficients.

One of the major differences between the measurement system shown in Fig. 3 and that shown in Fig. 4 is that, in the latter configuration, the measurement of pulse occurrence times are always made relative to a fixed reference phase. This reference is provided by the output of a zero-crossing detector similar to that used in our earlier

Fig. 4. System for measuring unconditional and conditional pulse-amplitude, amplitude-sum, and phase-of-occurrence distributions for a point process excited by an alternating voltage. The individual circuit units are defined as in Fig. 3.

work [29] which generates a positive 5 V pulse with a width of 2 μs whenever the excitation voltage changes sign from negative to positive. The output of the zero-crossing detector is fed to a pulse counter. The output of the pulse counter triggers two digital-delay generators DDG1 and DDG4 used to define the phase intervals over which measurements are made. Depending on the setting of the pulse-counter output, DDG1 and DDG4 are triggered either at the beginning of every cycle of the excitation voltage or at the beginning of every n th cycle, where n is an integer greater than 1.

The MCA, TAC, gate G1, Δt control logic (part A), SCAs and DDG3 are the same components used for the system configuration shown in Fig. 3. The other digital-delay generators DDG1, DDG2, and DDG4 are essentially identical in their operating characteristics to DDG3. The gated integrator and pulse selector are specifically designed for the system configuration shown in Fig. 4 and are described in the next section. The absolute-value

selector circuit is similar in design to a circuit used for previous PD measurements [30]. It provides a positive pulse to amplifier A2 independent of the sign of the input pulse. It can be operated to select either positive input pulses, negative input pulses, or pulses of both signs. This feature is needed because ac-generated PD pulses are either positive or negative depending on the half-cycle of the applied voltage in which they occur. The amplifier A2 is a commercial linear pulse amplifier that has a constant adjustable dc offset at the output. It delivers a rectangular negative pulse to the gated integrator with a constant width of 2 μs and with an amplitude proportional to the peak amplitude of the input pulse. It has output characteristics required for proper operation of the integrator. Shown in Tables 4 and 5 are the combinations of switch connections for S1-S5 in Fig. 4 that are required to configure the system for measurement of the various conditional and unconditional distributions given in Table 2.

Table 4. Configuration of switch connections for the system shown in Fig. 4 required for measurement of the various conditional and unconditional amplitude or total charge distributions for a periodic time-varying excitation process

Distribution	Switch					
	S1	S2	S3	S4	S5	S6
$p_0(q_i^{\pm}), i \geq 1$	*	*	x3=y3	x4=z4	*	x6=z6
$p_0(q_1^{\pm})$	x1=z1	x2=y2	x3=w3	x4=y4	x5=z5	*
$p_0(q_i^{\pm}), i=2,3,...$	x1=z1	x2=y2	x3=w3	x4=y4	x5=w5	*
$p_1(q_i^{\pm}|\Delta\phi^{\pm})$	*	*	x3=w3	x4=z4	*	x6=z6
$p_1(q_1^{\pm}|\phi_1^{\pm})$	x1=z1	x2=y2	x3=w3	x4=w4	x5=z5	*
$p_1(q_i^{\pm}|\phi_i^{\pm}), i=2,3,...$	x1=z1	x2=y2	x3=w3	x4=w4	x5=w5	*
$p_1(q_1^{\pm}|Q^{\mp})$	x1=z1	x2=z2	x3=w3	x4=y4	x5=z5	*
$p_1(q_i^{\pm}|Q^{\mp}), i=2,3,...$	x1=z1	x2=z2	x3=w3	x4=y4	x5=w5	*
$p_2(q_1^{\pm}|\phi_1^{\pm},Q^{\mp})$	x1=z1	x2=z2	x3=w3	x4=y4	x5=z5	*
	x1=z1	x2=z2	x3=w3	x4=y4	x5=z5	*
$p_2(q_i^{\pm}|\phi_i^{\pm},Q^{\mp}), i=2,3,...$	x1=z1	x2=z2	x3=w3	x4=w4	x5=w5	*
$p_1(q_i^{\pm}|\Delta\phi_{i,i-1}^{\pm}), i=2,3,...$	x1=z1	x2=y2	x3=w3	x4=y4	x5=w5	*
$p_2(q_i^{\pm}|\phi_{i-1}^{\pm},q_{i-1}^{\pm}), i \geq 2$	*	*	x3=w3	x4=y4	x5=y5	*
$p_3(q_i^{\pm}|\phi_i^{\pm},\phi_{i-1}^{\pm}q_{i-1}^{\pm}), i \geq 2$	*	*	x3=w3	x4=y4	x5=y5	*
$p_0(Q^{\pm})$	*	*	x3=z3	x4=z4	*	x6=y6

* Switch position irrelevant.

Table 5. Configuration of switch connections for the system shown in Fig. 4 required for measurement of conditional phase distributions for a periodic, time-varying excitation process

Distribution	Switch					
	S1	S2	S3	S4	S5	S6
$p_0(\phi_i^{\pm}), i=1,2...$	x1=z1	x2=y2	x3=y3	x4=z4	*	x6=y6
$p_1(\phi_i^{\pm}|Q^{\mp}), i=1,2,...$	x1=z1	x2=z2	x3=y3	x4=z4	*	x6=y6
$p_1(\phi_i^{\pm}|\phi_{i-1}^{\pm}), i=2,3...$	x1=y1	x2=y2	x3=y3	x4=x4	x5=y5	x6=y6
$p_2(\phi_i^{\pm}|\phi_{i-1}^{\pm},q_{i-1}^{\pm}), i=2,3...$	x1=y1	x2=y2	x3=y3	x4=z4	x5=y5	x6=y6
$p_3(\phi_i^{\pm}|\phi_{i-1}^{\pm},q_{i-1}^{\pm},Q^{\mp}), i=2,3,...$	x1=y1	x2=z2	x3=y3	x4=z4	x5=y5	x6=y6

* Switch position irrelevant.

An understanding of the system operation can be obtained with the aid of the pulse diagrams shown in Figs. 5–8. Consider first the measurement of the unconditional amplitude distribution, $p_0(q_i^{\pm})$, of the ith pulse in a particular half-cycle. Figure 5 shows the time sequence of signals that appear at the various indicated circuit locations in the system shown in Fig. 4 for the measurement of $p_0(q_1^-)$, i.e., the first pulse to appear on the negative half-cycle.
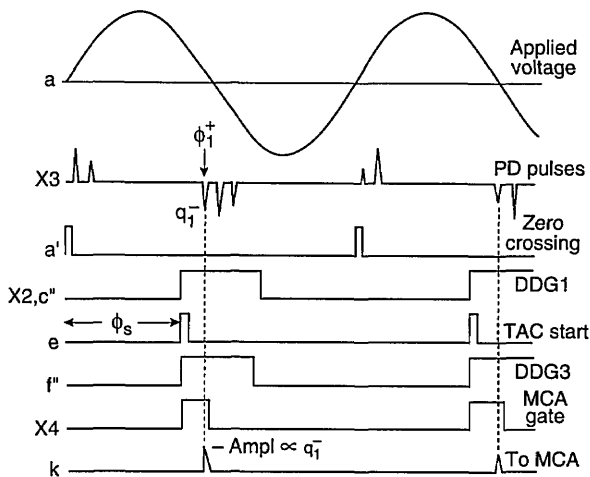
Fig. 5. Pulse timing diagram for indicated signal locations in the system configuration (Fig. 4) for measurement of the amplitude distribution, $p_0(q_1^-)$, of the first pulse to appear on the negative half-cycle of the applied voltage.
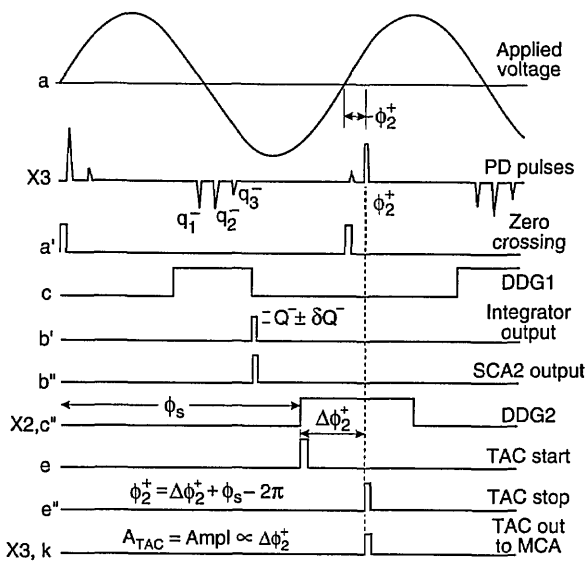
Fig. 6. Pulse timing diagram for indicated signal locations in the system configuration (Fig. 4) for measurement of the conditional distribution $p_1(\phi_2^+|Q^-)$.
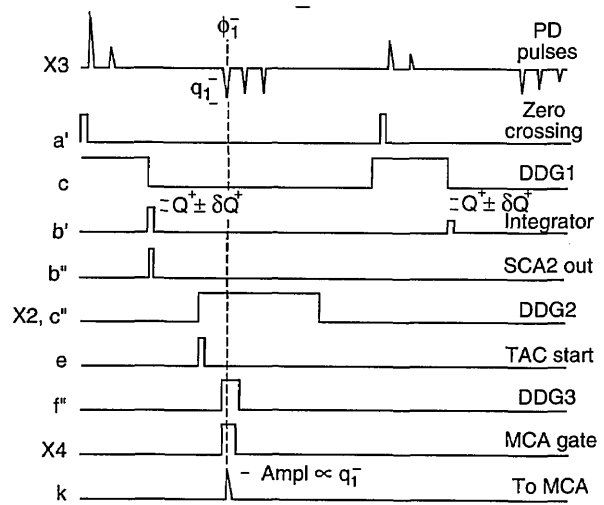
Fig. 7. Pulse timing diagram for indicated signal locations in the system configuration (Fig. 4) for measurement of the conditional distribution $p_2(q_1^-|\phi_1^-,Q^+)$.
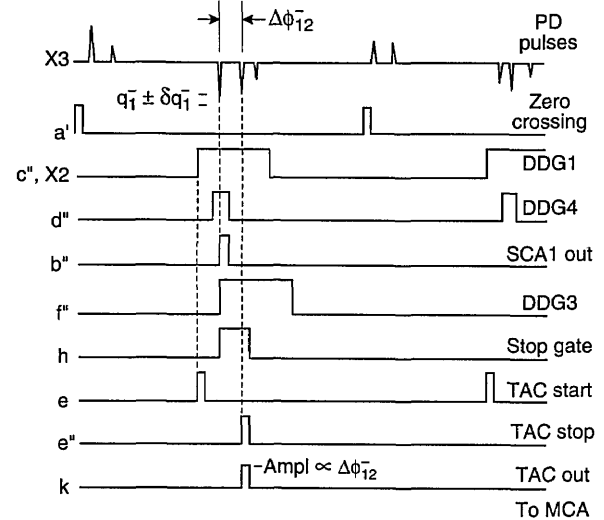
Fig. 8. Pulse timing diagram for indicated signal locations in the system configuration (Fig. 4) for measurement of the conditional distribution $p_2(\phi_2^-|\phi_1^-,q_1^-)$.

The cycle selector is assumed here to be set such that every pulse a' from the zero-crossing detector triggers the digital-delay generator DDG1. The output pulse from DDG1 is delayed relative to the zero-crossing pulse and its width is adjusted to encompass the entire phase region within which the negative pulses occur. This pulse is fed through switch S2 to the pulse-selector circuit which also receives pulses at location f from the pulse amplifier plus absolute value circuit. The pulse selector always generates a "start" pulse at e which is

coincident with the leading edge of the DDG1 pulse at a fixed phase ϕ_s. The start pulse triggers the Δt control logic circuit (part A) at e' which in turn triggers DDG3. The position and width of the DDG3 output pulse is adjusted in this case to be approximately the same as the DDG1 pulse. The output from the Δt control logic opens gate G2 to the MCA. It disables this gate after the next pulse appears at the f input (in this case the first negative pulse at ϕ_1^-). The amplitude of the first negative PD pulse is then recorded by the MCA shortly before G2 closes.

Measurement of $p_0(q_i^\mp)$ for values of i greater than 1 requires that the Δt control logic be triggered by the $(i-1)$th pulse. This is achieved by connecting e' to e through switch S5 (x5 = z5). The pulse selector will produce a pulse at e coincident in time (or equivalently in phase) with a selected pulse that occurs within the range defined by the DDG1 pulse. For example, if $p_0(q_3^-)$ is to be measured, then the second pulse is selected to appear at e. This pulse triggers the Δt control logic which in turn allows passage of the third pulse to the MCA.

The measurement of phase-of-occurrence distributions requires that the output of the time-to-amplitude converter, TAC1, be recorded by the MCA. The TAC1 circuit is triggered by the outputs from the pulse-selector circuit. The diagram in Fig. 6 shows the sequence of signals at the indicated circuit locations associated with the measurement of the conditional phase distribution $p_1(\phi_2^+|Q^-)$. Again, it is assumed that the cycle selector allows every zero-crossing detector pulse to trigger DDG1. In this case, the output pulse from DDG1 is used to control a gated integrator. The width and position of the DDG1 pulse is set to encompass all possible negative pulses that could occur in the negative half-cycle.

The integrator returns a pulse at the end of the DDG1 pulse that has an amplitude proportional to the sum, $\sum_i q_i^-$, of the amplitudes of all negative pulses contained within the phase window defined by the DDG1 pulse. If this sum has a value that lies within the window $Q^- \pm \delta Q^-$ defined by the single-channel analyzer SCA2, then SCA2 triggers DDG2 which controls the pulse selector. The pulse selector produces a TAC start pulse at the leading edge of the DDG2 pulse at a fixed phase ϕ_s. For the example shown in Fig. 6, the pulse selector is set to select the second positive pulse to appear in the window defined by DDG2. This pulse is used to stop TAC1 which then produces a pulse of amplitude directly proportional to $\Delta\phi_2^+ = \phi_2^+ - \phi_s$. The

actual phase-of-occurrence of the second pulse relative to the zero crossing is given by

$$\phi_2^+ = \phi_s - 2\pi + \kappa A_{TAC}, \qquad (12)$$

where A_{TAC} is the amplitude of the TAC output pulse and κ is a scale factor determined from a calibration of the TAC. By this process, ϕ_2^+ is recorded only if the sum of negative pulse amplitudes in the previous half-cycle lie within a restricted range thus yielding the conditional distribution $p_1(\phi_2^+|Q^-)$.

Figure 7 shows the sequence of signals associated with the measurement of the second-order amplitude distribution, $p_2(q_1^-|\phi_1^-,Q^+)$. As in the case of the $p_0(q_1^-)$ measurement indicated by the diagram in Fig. 5, this measurement requires use of both the pulse selector and Δt control logic circuits. Unlike the measurement of $p_0(q_1^-)$, the amplitude, q_1^-, is recorded only if the phase of this pulse and the sum of amplitudes on the previous half-cycle have values that lie within restricted ranges. The phase, ϕ_1^-, is restricted to lie within a range specified by the delay and width of the DDG3 pulse. As in the case for measurement of $p_1(\phi_i^\mp|Q^\mp)$, $Q^\mp$ is specified by the SCA2 window.

There are two switch configurations that can be used to measure $p_2(q_1^\mp|\phi_i^\mp,Q^\mp)$. The diagram in Fig. 7 corresponds to the first set of switch connections for this distribution listed in Table 4. The second set of switch connections are required for measurement of $p_2(q_i^\mp|\phi_i^\mp,Q^\mp)$ if $i \geq 2$. The phase, $\phi_i^\mp$, in this case is restricted not by DDG3, but rather by DDG4 that controls gate G3. The gate G3 is actually a built-in feature of the Δt control logic circuit (part A) as will be shown later.

The case for $p_2(\phi_2^-|\phi_1^-,q_1^-)$ is shown in Fig. 8. This measurement also requires use of both the pulse selector and Δt control logic circuits. The Δt control logic is used to enable a gate in the pulse selector that controls passage of the TAC stop pulse. The amplitude q_1^- is restricted by the window setting for SCA1. The phase, ϕ_1^-, is restricted by the DDG4 pulse which controls SCA1. If q_1^- lies within the specified range, SCA1 will produce a pulse at the end of the DDG4 pulse that triggers the Δt control logic. The Δt control logic uses DDG3 to open the pulse selector gate. If the next pulse to occur is indeed the second pulse, it will cause a stop pulse to be transmitted to TAC1. If the next pulse is not the second pulse, then the stop pulse output of the pulse selector will simply be disabled. Thus only the phase of ϕ_2^- can be recorded provided the previous pulse satisfies the specified conditions for amplitude and phase.

The measurement of unconditional amplitude sum distributions, $p_0(Q^{\mp})$, is simply obtained by transferring the output of the gated integrator directly to the MCA through amplifier A3 and gate G2. For this measurement, G2 is kept open continuously by proper positioning of S4. The amplifier A3 can be a combination of the amplifier built into the integrator and an external pulse amplifier. The gain of A3 is adjusted to give the desired range acceptable to the MCA, e.g., so that the maximum pulse amplitude is below 8 V.

The distinction between the distributions $p_1(q^{\mp}|\Delta\phi^{\pm})$ and $p_1(q^{\mp}|\phi_i^{\mp})$ in Table 4 is that $\Delta\phi^{\pm}$ is an *arbitrary* fixed phase window selected by DDG1 whereas $\phi_i^{\mp}$ is a fixed phase associated with the occurrence of ith pulse. The measurement of $p_1(q^{\mp}|\phi_i^{\mp})$ is like that for $p_2(q^{\mp}|\phi_i^{\mp},Q^{\mp})$ except that $Q^{\mp}$ is not specified. In cases where specification of $Q^{\mp}$ is not required, the pulse selector circuit can be controlled directly by the output pulse from DDG1 as for the case considered in Fig. 5.

The measurement of $p_1(q^{\mp}|Q^{\mp})$ is like that for $p_2(q^{\mp}|\phi_i^{\mp},Q^{\mp})$ except $\phi_i^{\mp}$ is not specified. The measurement of $p_3(\phi_i^{\mp}|\phi_{i+1}^{\pm},q_{i+1}^{\pm},Q^{\mp})$ is like that for $p_2(\phi_i^{\mp}|\phi_{i+1}^{\pm},q_{i+1}^{\pm})$ considered in Fig. 8 with an additional specification on the value for $Q^{\mp}$, which is achieved by controlling the pulse selector circuit with DDG2 rather than DDG1. The measurement of $p_1(q^{\mp}|\Delta\phi_{i,i-1}^{\mp})$ is like that for $p_1(q_i|\Delta t_{j-1})$ in the constant excitation case with the exception that the Δt control logic is triggered by a particular pulse selected from the pulse selector circuit so that i has a specified value, i.e., it is not arbitrary as in the constant excitation case. For the measurements of the conditional distributions $p_2(q^{\mp}|\phi_i^{\mp},q_{i+1}^{\pm})$ and $p_3(q^{\mp}|\phi_i^{\mp},\phi_{i+1}^{\pm},q_{i+1}^{\pm})$, the values of $\phi_{i+1}^{\pm}$ and $q_{i+1}^{\pm}$ are restricted by the windows defined respectively by DDG4 and SCA1 as for the measurement of $p_2(\phi_i^{\mp}|\phi_{i+1}^{\pm},q_{i+1}^{\pm})$ shown in Fig. 8.

It is obvious that the system in Fig. 4 can be configured to measure other types of conditional distributions such as $p_4(q^{\mp}|\phi_i^{\mp},\phi_{i+1}^{\pm},q_{i+1}^{\pm},Q^{\mp})$. However, the operation of the system has only been tested for distributions like those listed in Tables 4 and 5. The cycle selector allows triggering of DDG1 and DDG4 only after n cycles have occurred. By using this feature it is possible to check for memory propagation from half-cycles that occurred prior to the most recent half-cycle such as would be indicated by the conditional distributions $p_1(\phi_{ij}^{\pm}|Q_k^{\mp})$ with $k>j$.

4. Measurement System Components

This section provides detailed information about the individual circuits that were designed for use with the measurement configurations shown in Figs. 3 and 4. Some of the circuits, such as the pulse-sorter circuit in Fig. 3 used for measurement of $p_0(\Delta t_j)$ have previously been described [24] and remain unchanged. These circuits are not covered in this section. Some such as the Δt control logic circuits (parts A and B) have been revised and are included here. Circuits that have features specific to the measurement of phase-correlated distributions such as the gated integrator, pulse selector, and gated single-channel analyzer in Fig. 4 have not previously been described and are covered here. Some circuits such as the zero-crossing detector, pulse counter-cycle selector, and absolute-value selector are considered to have well known design and operating characteristics [31] and are not included here. Other circuits not considered here are those that are commercially available such as the digital-delay generators, time-to-amplitude converters, linear pulse amplifiers, and multi-channel analyzer. The description of each circuit given below includes both circuit and associated pulse diagrams.

4.1 Time-Interval Control Logic (Parts A and B)

The Δt control logic circuits described in this section have replaced the circuits previously shown in Figs. 2 and 4 of Ref. [24]. The designs have been improved to extend the measurement capabilities of the system and to eliminate or reduce errors previously noted [1].

4.1.1 Part A The function of the Δt control logic (part A) is to control a digital-delay generator (DDG3 in Figs. 3 and 4) to enable either the gate to the MCA (G2 in Figs. 3 and 4) or the gate for the stop pulse in the pulse-selector circuit of Fig. 9. The operation of the circuit can be understood with the aid of the pulse diagram shown in Fig. 10.

Unlike the circuit previously described in Ref. [24], the buffer amplifiers defined by the transistors T1 and T2 are connected to separate inputs (f and e"). For some applications, such as the measurement of $p_1(q_j|\Delta t_{j-1})$, the inputs f and e" are connected together, and in other applications, such as the measurement of $p_2(q_j|q_{j-1},\Delta t_{j-1})$, these inputs are connected to different locations, e.g., by switch S2 and Fig. 3. The gain of these

(CO1) - 7493 counter
(SR1-SR3) - 74164 shift register
(OS1-OS3) - 74123 one shot
(T1-T5) - 2N2219A
(G1-G12) - 7400 NAND, 7402 NOR
(I1-I6) - 7404
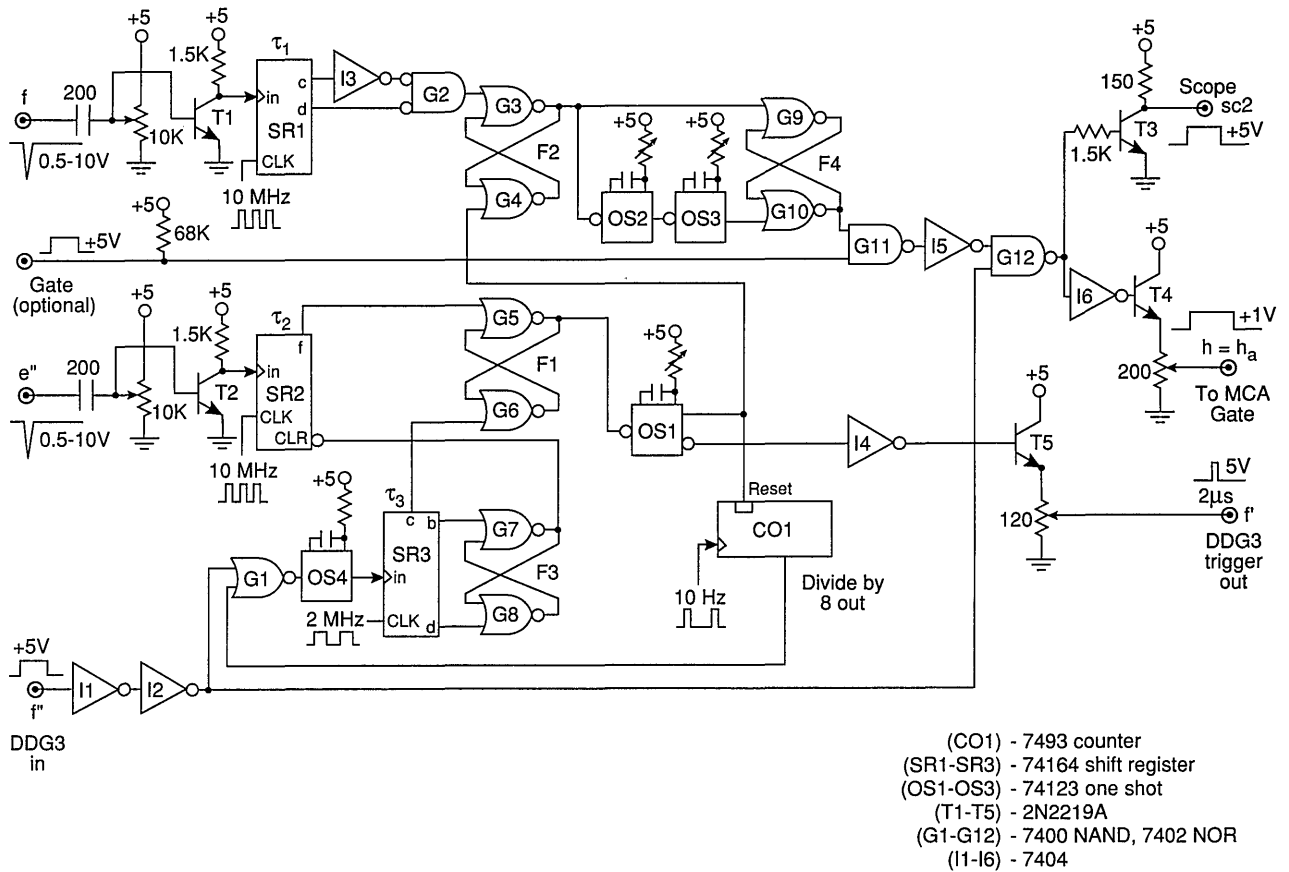
Fig. 9. Diagram of the time interval (Δt) control-logic circuit, part A. The individual integrated circuit components are specified in the legend.
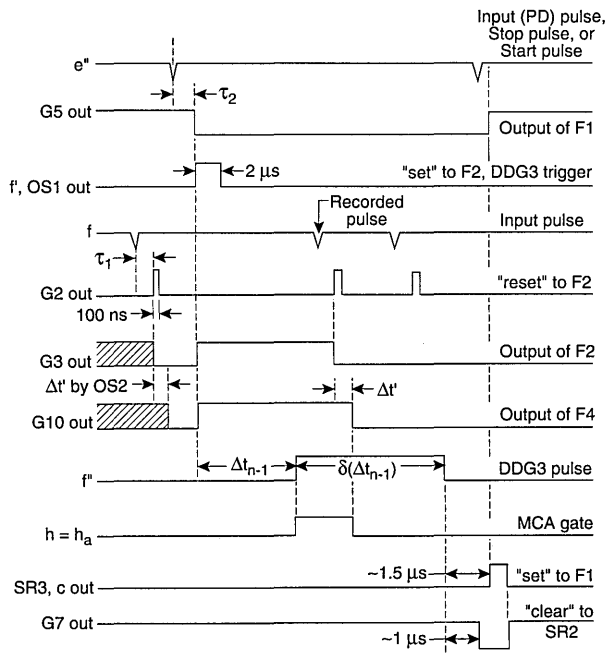
Fig. 10. Pulse timing diagram for the different indicated circuit locations in the Δt control logic circuit (part A) shown in Fig. 9.

buffers is adjusted so that their output is a 5 V logic pulse independent of the peak voltage of the input pulse. Ideally the input pulse voltage should lie within the range of 0.3 to 10 V corresponding to the range accepted by the MCA. For the systems shown in Figs. 3 and 4, the range of input pulse voltages is usually determined by the gain setting of the input amplifier A1.

The outputs of the buffer amplifiers (T1 and T2 in Fig. 9) trigger the 10-MHz serial shift registers SR1 and SR2 that serve the purpose of delaying the pulses by the times τ_1 and τ_2 respectively. A pulse appearing at e″ is allowed to trigger the digital-delay generator (DDG3) at output f″ if the flip-flop circuit F1 defined by gates G5 and G6 is in the proper "initial-condition" state. If it is in this state, then the output of SR2 will cause it to change state after a delay of $\tau_2 = 600$ ns, and the output of G5 will drop to zero thus triggering the one shot OS1. The one-shot produces a 2 μs pulse for triggering DDG3 and also sets flip-flop F2 which indirectly results in the enabling of gate G12. If G12 is enabled, the returning pulse from DDG3

which appears at the f'' input will be allowed to pass to the output h that is used to control the gate to the MCA or the gate of the pulse selector.

A pulse appearing at the f input will disable G12 and prevent transfer of the DDG3 output pulse to h. In Fig. 10, the DDG3 pulse is indicated to have a delay Δt_{n-1} and a width $\delta(\Delta t_{n-1})$. The circuit is thus designed not to record a pulse in the MCA if that pulse follows the pulse which triggered DDG3 within a time less than $\Delta t_{n-1} + \tau_2$. This feature ensures proper measurement of distributions conditioned on a fixed time separation, e.g., $p_1(q_j|\Delta t_{j-1})$, where it is required that Δt_{j-1} fall within the range Δt_{j-1} to $\Delta t_{j-1} + \delta(\Delta t_{j-1})$ defined by DDG3.

If a pulse appears at f, it will cause F2 to be reset after a delay of $\tau_1 = 300$ ns set by SR1. The delay τ_1 must be less than τ_2 in order to prevent immediate resetting of F2 for coincident inputs at f and e''. The pulse, generated by OS3, that initiates the disabling of gate G12 is delayed by a short interval defined by one-shot OS2. This small added delay ($\Delta t'$ in Fig. 10) is necessary to ensure that the MCA gate stays enabled long enough to allow recording of any pulse that appears within the desired time interval.

The circuit is reset by the pulse returned to input f'' by DDG3. The one-shot OS4 is triggered by the trailing edge of the DDG3 pulse independent of whether or not the gate G12 was disabled before time $\Delta t_{n-1} + \delta(\Delta t_{n-1})$ by an intermediate or recorded input pulse. The output of OS4 is delayed by the shift register SR3. Two of the outputs from SR3 control flip-flop F3 (gates G7 and G8) which in turn clears the contents of SR2 to prevent simultaneous setting and resetting of F1. Another output of SR3 then sets F1 to the initial condition which allows DDG3 to be triggered at output f' by the next pulse to appear at e''. Generally, any pulse that appears at e'' will also appear at f so that F2 will also be reset in the event that it was not already reset.

The circuit has an additional, optional "gate" input which allows the output pulse at h to be gated by an independent source. This gate is also designated by G3 in Fig. 4 and used for the measurement of $p_2(q\ \overline{\tau}\ |\phi\overline{\tau}, Q\ \overline{\tau})$. The present Δt control logic circuit has an auto-reset capability similar to that described previously [24] so that a reset pulse will appear at G1 to initialize F1 within a time of 0.8 s if for some reason a pulse is not returned from DDG3. If it is necessary to record

times longer than 0.8 s, then the 10 Hz auto-reset clock can be replaced with one of lower frequency.

4.1.2 Part B Part B of the Δt control logic is required together with part A when measurements of the conditional pulse-amplitude distributions $p_1(q_j|\Delta t_{j-i})$ are made for $i > 1$ as discussed in Sec. 3.1. The version of the circuit shown in Fig. 11 differs from that described in our earlier work (Fig. 4 of Ref. [24]) which only enabled measurement of $p_1(q_j|\Delta t_{j-2})$ corresponding to the case where $i = 2$. The present circuit incorporates a pulse counting feature that allows determination of distributions for $i > 2$.

The operation of the circuit shown in Fig. 11 can be understood from a consideration of the pulse diagram shown in Fig. 12. The pulse time separation between the $(j - i + 1)$ and $(j - i)$th events (see Fig. 1) is restricted by the delay and pulse width settings of DDG3. The output of DDG3 is controlled by part A as described in the previous section so as to ensure that Δt_{j-i} is properly defined as a time separation between adjacent pulses. The operation of the Δt control logic (part B) is thus initiated by the simultaneous occurrence of an event (PD) pulse at input $e_b = e''$ and a pulse from the $h = h_a$ (or equivalently SC2) output of the Δt control logic (part A) at input SC2. An event occurring in coincidence with the SC2 input sets flip-flop F5 (gates G14 and G15) which in turn allows the counter CO2 to count subsequent event pulses. When the output of the counter corresponds to a binary number equal to $i - 2$, as determined by the settings of switches S1-S4, the comparator C1 triggers the one-shot OS5. The output of OS5 sets flip-flop F6 (gates G17 and G18) which enables the gate (G2 in Fig. 3) of the MCA at output $h = h_b$. It also triggers the one-shot OS6 which in turn resets F5 and consequently also the counter CO2. The MCA will record the next (j th) event to occur after G3 is opened independent of its time separation from the preceding $(j - 1)$th event. Immediately after this event is recorded, the MCA sends a 5 V "event pulse" to the input d'. After a short delay determined by the one-shots OS7 and OS8, the event pulse resets F6 and thereby disables the MCA gate. The circuit is then ready to be triggered by the next coincidence to occur at inputs SC2 and $e_b = e''$. If for any reason the MCA fails to return an event pulse, e.g., the j th pulse was too small to be recorded, then the counter CO3 automatically provides a reset for F6 after 8 successive coincident pulses have appeared at SC2 and $e_b = e''$.
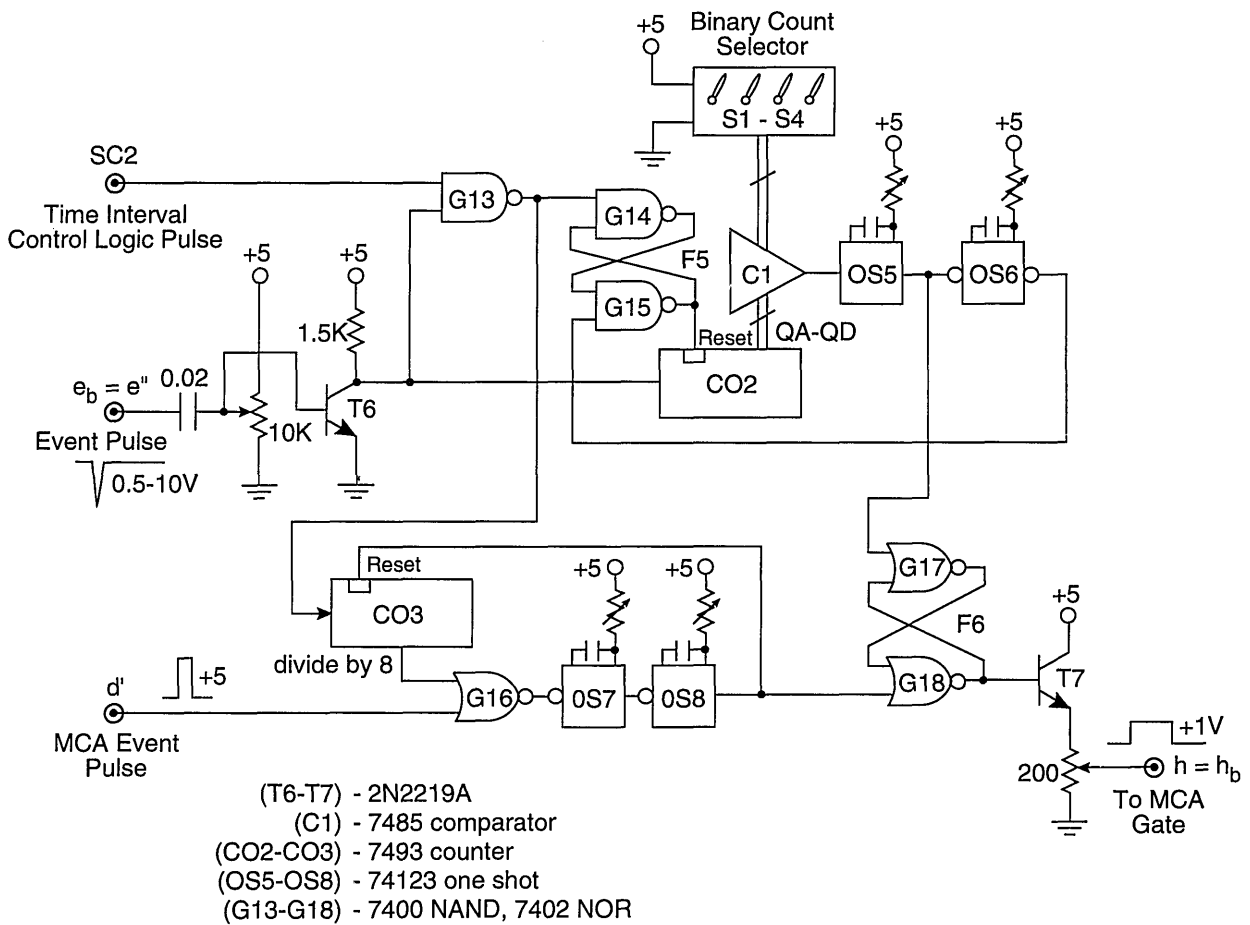
Fig. 11. Diagram of the Δt control logic circuit, part B. The individual integrated-circuit components are specified in the legend.

Count selector set at 5
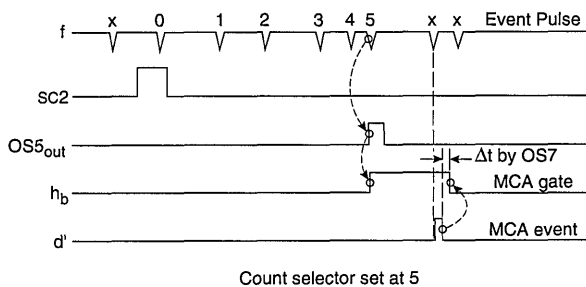
Fig. 12. Pulse timing diagram for the Δt control logic (part B) shown in Fig. 11. It is assumed in this example that the binary count selector is set by switches S1-S4 to the value 5.

4.2 Pulse Selector

A diagram of the pulse-selector circuit is shown in Fig. 13. The associated pulse diagram is shown in Fig. 14. This circuit is used to select a particular numbered event that occurs after a specified time or phase. It is used in the system shown in Fig. 4 to measure the conditional phase or amplitude distributions of specific pulses that occur within well-defined phase windows of the excitation voltage, e.g., $p_1(\phi_i^{\pm} | Q^{\mp})$, $i = 1, 2, 3 ...$

The pulse selector produces a -2 V "start" pulse at output e that is coincident with the rising edge off a $+5$ V digital-delay generator pulse applied to input c". This DDG pulse is assumed to define a fixed phase or time window, and therefore the output at e occurs at a known phase or time, i.e., it provides the appropriate phase reference point. The circuit is designed to produce -2 V "stop" pulses at outputs e" (Stop 1) and SC1 (Stop 2) that are coincident with the i th pulse to occur after the phase-reference point, i.e., after the "start" pulse. The value of i is determined by the setting of the binary count selector (switches S1$-$ S8).
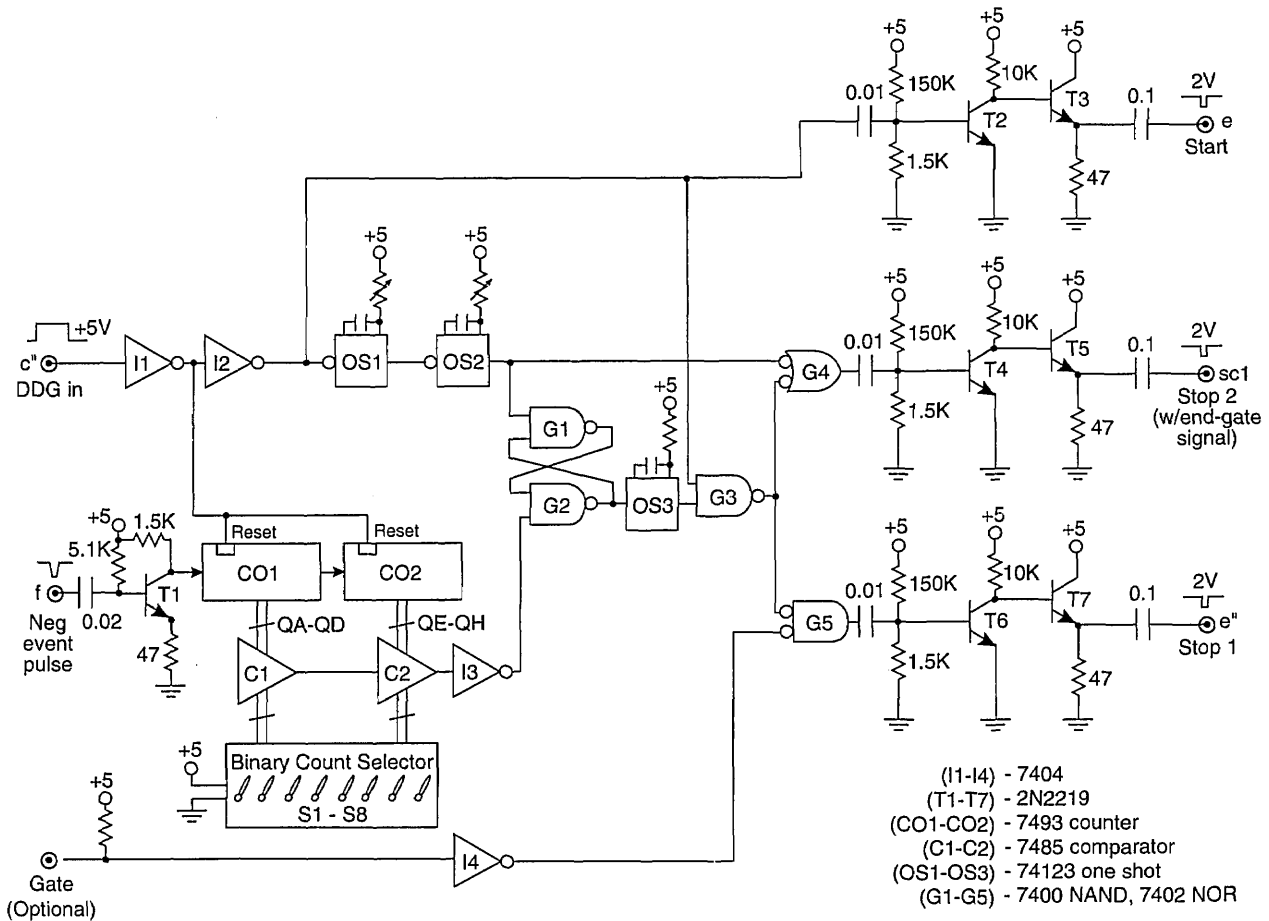
Fig. 13. Diagram of the pulse-selector circuit used for the measurement system shown in Fig. 4. The individual circuit components are specified in the legend.

(I1-I4) - 7404
(T1-T7) - 2N2219
(CO1-CO2) - 7493 counter
(C1-C2) - 7485 comparator
(OS1-OS3) - 74123 one shot
(G1-G5) - 7400 NAND, 7402 NOR

Count selector set at 3
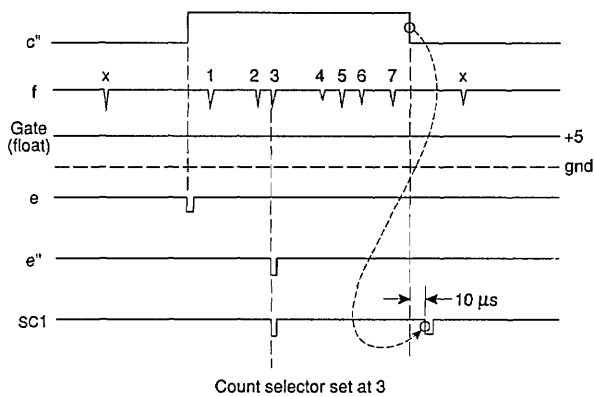
Fig. 14. Pulse timing diagram for the pulse-selector circuit shown in Fig. 13. It is assumed here that the binary count selector is set to select the third pulse to occur within the time interval defined by the duration of the pulse appearing at input c".

In the operation of this circuit, the pulse counters CO1 and CO2 are enabled by the DDG window. The negative event pulses that appear at input f are then counted by CO1 and CO2. The binary outputs of these counters are sensed by the comparators C1 and C2. If and when the binary number presented by the counter outputs equals the 8-bit binary number selected by the terminal switches, i.e., for $i = 1$ to 256 pulses, the output of C2 goes from 0 to $+5$ V and sets the flip-flop defined by gates G1 and G2. This flip-flop triggers the one-shot OS3 that produces the "stop" pulses that ultimately appear at e" and SC1.

At the falling edge of the DDG pulse, the counters CO1 and CO2 are reset and the one-shots OS1 and OS2 are triggered. The output of OS2 resets the flip-flop and delivers a "stop" pulse to SC1 in

coincidence with the end of the DDG window. This pulse does not appear at the e" output. The "end-of-window" stop pulse provides another phase mark that may be useful in some applications.

The appearance of the stop pulse at e" can also be controlled by another external pulse applied to the "gate" input. This option is used for the system shown in Fig. 4 for the measurement of various conditional phase distributions as indicated in Table 5.

4.3 Single-Channel Analyzer

The single-channel analyzer circuit designed for the measurement systems shown in Figs. 3 and 4 is presented in Fig. 15. The operation of this circuit is indicated by the pulse diagrams shown in Figs. 16 and 17. If the amplitude of the input pulse at b' lies within a selectable voltage window, then the SCA delivers both a -2 V and $+5$ V pulse to the indicated output points at b".

The circuit is capable of either gated or ungated operation. For ungated operation, output pulses are generated at b" for any input pulse that has an amplitude within the selected window independent of its time of occurrence. For gated operation, output pulses are generated only if the input pulse occurs within a time interval defined by the width of a 5 V gate pulse applied to input d". Depending on the setting of the switch S2, the output pulses for the gated operation will either appear at a time approximately coincident with the input pulse (with a slight delay) or at a time coincident with the end of the gate pulse. The three possible modes of operation are identified in Fig. 16.

In the operation of this circuit, the event pulse is sensed by amplifier A1, the output of which either follows or inverts the signal depending on the position of switch S1. The output of this amplifier then proceeds to the analog comparators C1 and C2. The other inputs to the comparators are derived from that part of the circuit (amplifiers A2-A5)

Switch Positions	Selections
$a_0 = a_2$	positive input
$a_0 = a_1$	negative input
$b_0 = b_2$	END SYNCH operation
$b_0 = b_1$	GATED operation

(T1-T3) - 2N2219
A1 - OP17
(A2-A5) - LF356
(C1-C2) - CMP01
(OS1-OS4) - 74123
(G1-G7) - 7400
(I1-I2) - 7404
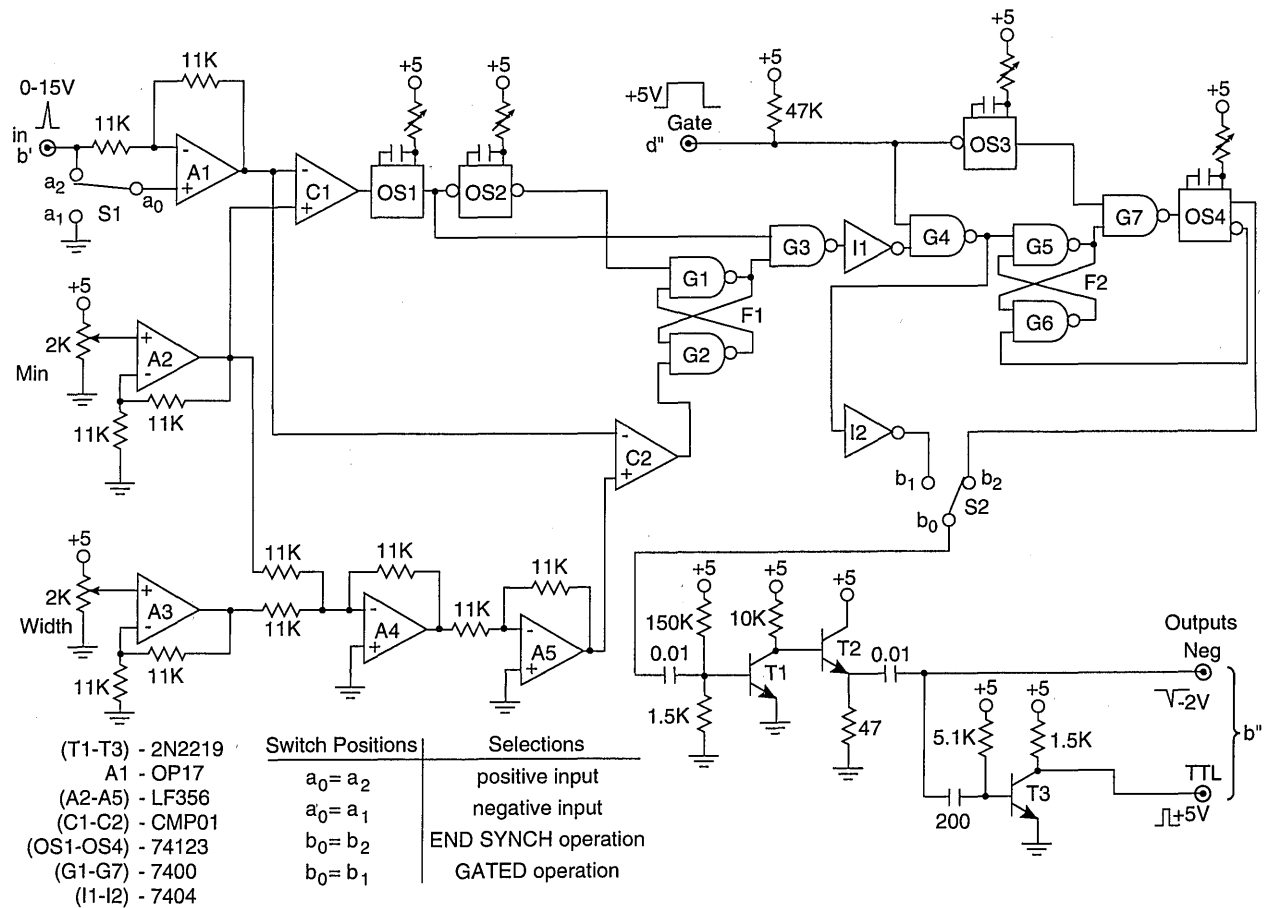
Fig. 15. Circuit diagram for the gated single-channel analyzer. The individual integrated-circuit components and switch configurations of the different modes of operation are shown in the legend.
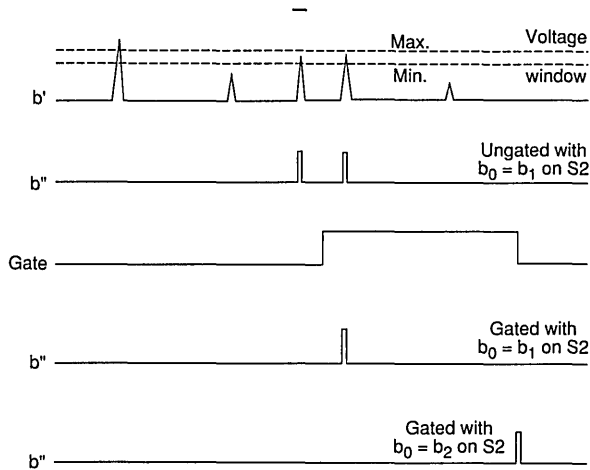
Fig. 16. Pulse timing diagram corresponding to the different possible operating modes for the single-channel analyzer shown in Fig. 15.
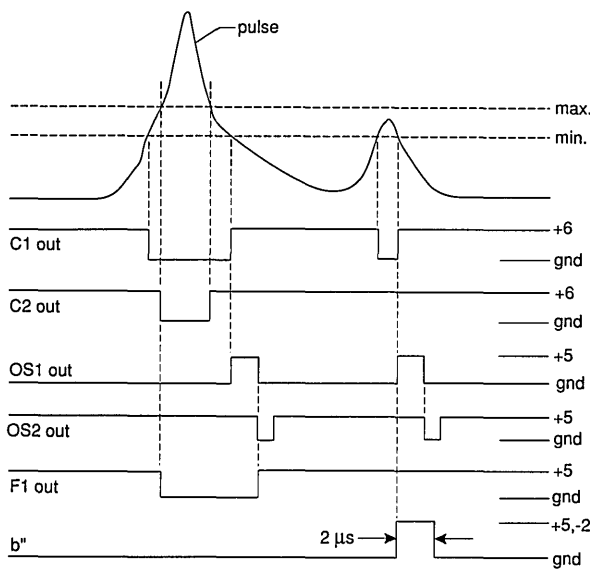
Fig. 17. Pulse timing diagram for the indicated circuit locations of the single-channel analyzer shown in Fig. 15.

that define the minimum voltage and width of the window. Voltages in the range of 0 to +5 V are selected by the two 2 kΩ resistors denoted by "min" and "width" in Fig. 15. These voltages are doubled by amplifiers A2 and A3. Amplifier A4 sums and inverts the outputs of A2 and A3, and amplifier A5 in turn inverts the output of A4. Consequently, the positive input of C1 is a voltage between 0 and +10 V corresponding to twice the "min" value and the positive input of C2 is a voltage between 0 and +15 V equal to twice the value of the "min" plus "width" voltages.

As indicated in Fig. 17, the outputs of C1 and C2 are normally high (+6 V) and go negative when the negative input exceeds the positive input. The circuit is designed so that input event pulses with amplitudes below the "min" value are ignored while those exceeding the maximum value ("min" plus "window") are inhibited. In the latter case, the inhibition results from the setting of flip-flop F1 (gates G1 and G2) by the output of C2 which in turn disables G3. If the input event pulses fall within the window, then the output of the one-shot OS1 triggered by C1 passes through the gate G3 and becomes the source for the 2 μs output pulse at b". The output of OS1 also triggers OS2 which resets F1 after a delay sufficient to prevent passage of any pulses through G3 that exceed the maximum value as illustrated in Fig. 17.

For normal gated operation, the switch S2 is set so that $b_0 = b_1$. This allows G4 to be enabled by a +5 V gate pulse at d" and thereby permits passage of the pulse from G3 to the output buffer amplifiers (transistors T1-T3). If it is desired to have the output pulses appear at a fixed time corresponding to the end of the gate pulse, then $b_0 = b_2$ at S2. In this mode, the output of OS1 passes through G3 and G4 and ultimately triggers flip-flop F2 (gates G5 and G6) which in turn enables G7. The one-shot OS3 is triggered by the falling edge of the gate pulse and thus produces a pulse that passes through G7 and triggers OS4. The output of OS4 resets F2 and also becomes the source of the output pulses at b".

4.4 Gated Integrator

The integrator circuit used for the measurement system in Fig. 4 is shown in Fig. 18 and the corresponding pulse diagram is shown in Fig. 19. The output of the integrator is a pulse with an amplitude in the range of 0 to 12 V directly proportional to the sum of the areas under all pulses that occur within the gate time interval denoted by Δt_1 in Fig. 19. If all pulses have the same shape so that their amplitudes are proportional to their areas, then the height of the integrator output pulse is also proportional to the sum of the amplitudes of all pulses occurring within Δt_1.

For the circuit in Fig. 18, the input pulses to the integrating amplifier A1 are assumed to be of constant width ($\sim 1 \mu$s) with amplitudes in the range of 0 to -12 V. In the absence of a 5 V gate pulse at input c, the flip-flop defined by gates G1 and G2 keeps the field-effect transistors (FET's) T1 and T2 turned on so that the 0.01 μF integrating capacitor is effectively shorted. The application of a pulse at
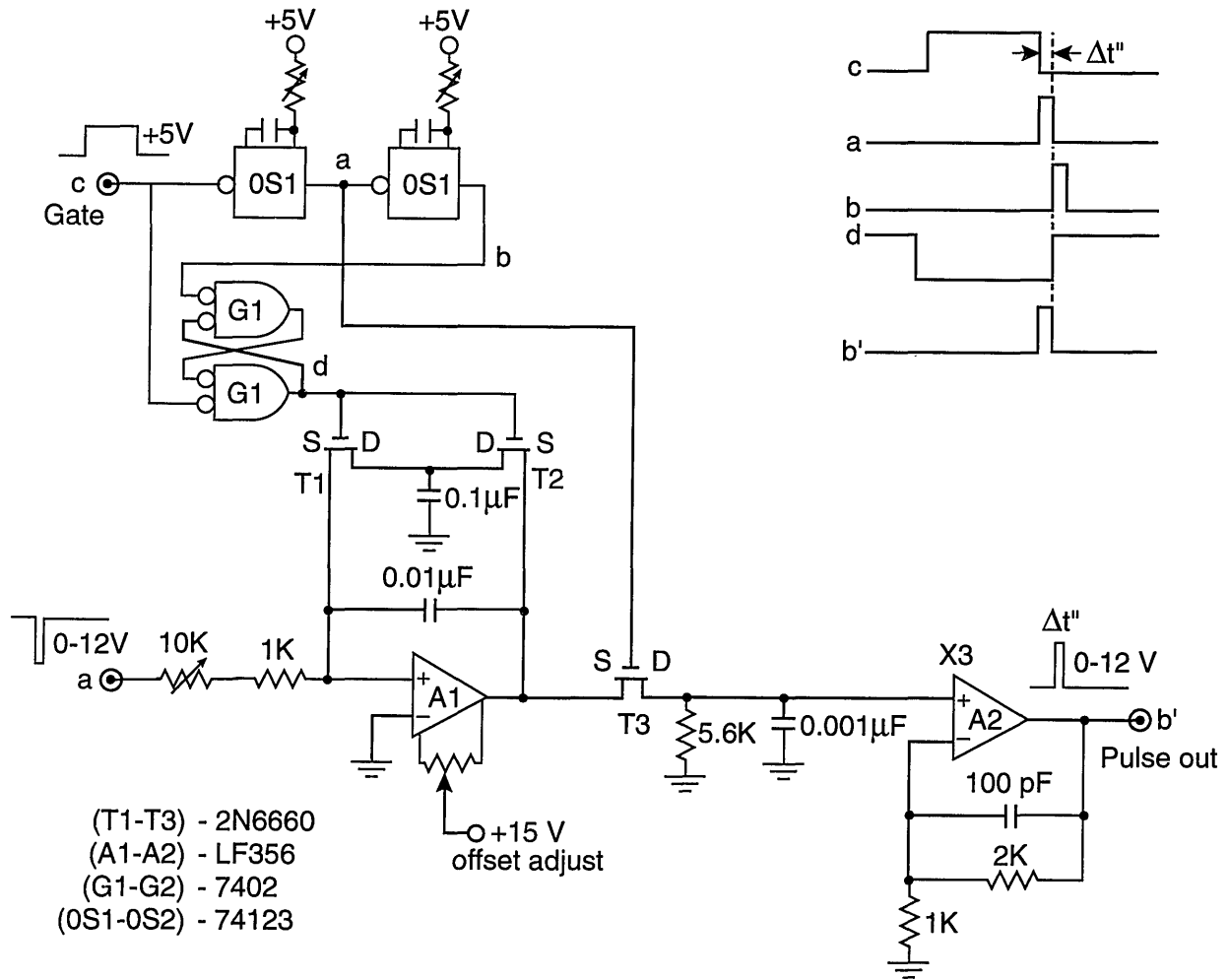
Fig. 18. Circuit diagram for the gated integrator.
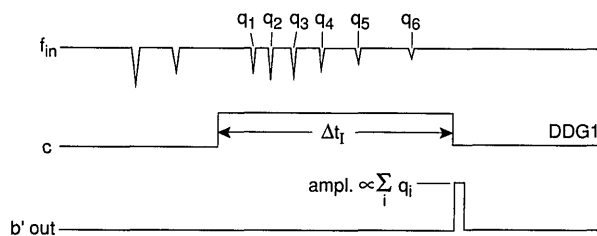
Fig. 19. Pulse timing diagram for the gated integrator circuit shown in Fig. 18.

c changes the state of the flip-flop which then turns off T1 and T2 thus allowing charge to accumulate on the integrating capacitor. At the end of the gate pulse, the one-shot OS1 is triggered and its output momentarily turns on T3 which allows transfer of the integrator amplifier output voltage to amplifier A2 and thereby to the output terminal b'. The trailing edge of the OS1 output pulse also triggers OS2 that generates a pulse to reset the flip-flop which in turn turns on T1 and T2 thereby discharging the integrating capacitor.

5. Examples of Results

The purpose of this section is to show examples of data on conditional and unconditional distributions that have been obtained using the systems shown in Figs. 3 and 4 respectively for measurement of dc and ac excited pulsating PD. A detailed discussion of the physical bases for the observed stochastic properties of PD phenomena goes beyond the scope of this paper and can be found in other works [1–4].

5.1 Continuous Excitation Process (dc-Generated PD)

Shown in Fig. 20 are examples of the measured unconditional and conditional pulse-amplitude distributions $p_0(q_n)$, $p_1(q_n|\Delta t_{n-1})$, and $p_2(q_n|\Delta t_{n-1},q_{n-1})$ for negative corona (Trichel) pulse discharges generated with a point-plane electrode gap in a neon-oxygen gas mixture at atmospheric pressure (100 kPa). The unconditional and first-order conditional distributions are plotted on a logarithmic scale and normalized to the maximum values to facilitate comparisons of the various distributions. The pulse amplitudes are expressed in units of (pC) as explained in previous work [1,27] (also see Sect. 6.1). The dependence of the first-order distributions $p_1(q_n|\Delta t_{n-1})$ on Δt_{n-1} implies a strong positive dependence of q_n on Δt_{n-1}, i.e., $(\Delta t_{n-1}\uparrow \Rightarrow q_n \uparrow)$. This behavior can be explained in terms of the expected influence of the
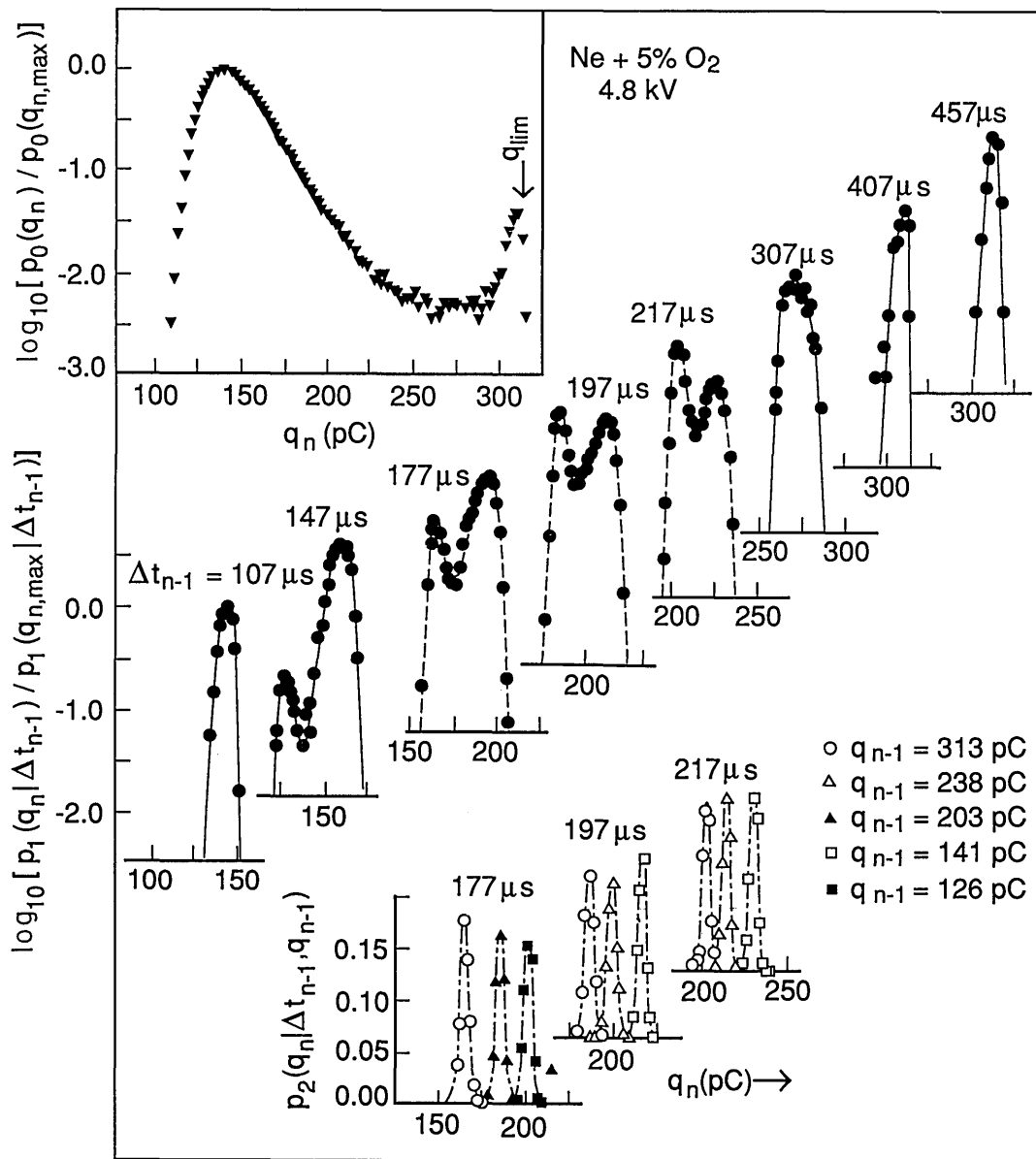
Fig. 20. Measured unconditional and conditional pulse-amplitude distributions $p_0(q_n)$, $p_1(q_n|\Delta t_{n-1})$, and $p_2(q_n|q_{n-1},\Delta t_{n-1})$ at the indicated "fixed" values for Δt_{n-1} and q_{n-1} for negative-corona discharge pulses generated using a point-plane electrode gap in a Ne+5% O_2 gas mixture (see Ref. [1]).

moving negative-ion space-charge cloud from the previous pulse on the electric field in the gap and consequently also on the growth of the next discharge pulse [1].

The dependence of the distributions $p_2(q_n|\Delta t_{n-1},q_{n-1})$ on q_{n-1} for a fixed Δt_{n-1} implies a negative dependence of q_n on q_{n-1}, i.e., $(q_{n-1}\uparrow \Rightarrow q_n \downarrow,\Delta t_{n-1}$). This behavior can be explained from consideration of the *size* of the space-charge cloud from the previous event on the growth of a discharge pulse. The data for both the first and second order pulse-amplitude distributions clearly demonstrate the importance of memory effects in determining the stochastic behavior of this discharge phenomenon.

The dashed lines shown for the first-order distributions at $\Delta t_{n-1}=177$, 197, and 217 μs were calculated using the integral expression [1]

$$p_1(q_n|\Delta t_{n-1})=p_0(\Delta t_{n-1})^{-1}\int_0^{\infty} p_0(q_{n-1})$$

$$p_1(\Delta t_{n-1}|q_{n-1})p_2(q_n|q_{n-1},\Delta t_{n-1})dq_{n-1} \qquad (13)$$

with numerical data obtained for the distributions shown in the right-hand side. Data for the conditional time-interval distribution, $p_1(\Delta t_n|q_n)$, used in the integral are shown in Fig. 21. It is interesting to note that in this case $\langle \Delta t_n(q_n)\rangle$ increases as q_n increases, i.e., $(q_n \uparrow \Rightarrow \Delta t_n \uparrow)$. This means that the larger the previous event, the longer on average will be the time spacing between this event and the next event. This has been explained in terms of the influence of the electric field generated by space charge from earlier discharge pulses in suppressing the release of electrons from the cathode needed to initiate subsequent pulses [1].

It is evident from the results shown here that it would be impossible to find a physical interpretation of measured unconditional pulse-amplitude distributions without information about the memory effects revealed by the conditional distributions. The unconditional amplitude distribution is related to the time-interval distribution $p_0(\Delta t_n)$ and the conditional distribution $p_1(q_n|\Delta t_{n-1})$ through Eq. (7). The first-order conditional distribution is in turn related to higher order distributions through Eq. (13). An unraveling of memory effects is a required step toward understanding the observed stochastic properties of random point processes such as reported here for the Trichel-pulse discharges.

5.2 Periodic Time Varying Excitation Process (ac-generated PD)

Data were obtained in this case for partial discharges generated by applying a sinusoidal alternating voltage to a point-dielectric discharge gap in air. Preliminary results from these measurements have recently been reported [2, 4, 32]. Figure 22 shows examples of measured unconditional and conditional pulse-amplitude distributions of the first negative pulse to appear in each cycle. Also shown are the unconditional and conditional phase-of-occurrence distributions for this pulse. These results were acquired after observing the discharge pulses for many thousands of cycles of the applied voltage.

The data shown in Fig. 22 were obtained using a stainless-steel point electrode positioned over a large, flat polytetrafluoroethylene (PTFE) dielectric surface in room air at a temperature of 23 °C. The tip of the stainless-steel electrode had a radius-of-curvature of 0.05 mm and was separated from the PTFE surface by a gap of 1.2 mm. A 200 Hz, 3.0 kV rms sinusoidal voltage was applied to the gap.

All distributions shown in Fig. 22 have been arbitrarily normalized to the maximum values. The indicated values for Q^+ correspond to the integrated charge associated with all positive PD events in the previous half-cycle [see Eq. (4)] and define the type of line used to represent the data. In the case of the second-order distributions, $p_2(q_1^-|\phi_1^-,Q^+)$, the fixed phase windows are defined directly under the data to which they apply.

There are clear indications from these data of the significance of memory propagation in determining the stochastic behavior of the phenomenon. The data for $p_1(\phi_1^-|Q^+)$ indicate that the larger the value of Q^+, the smaller is the value of the mean phase-of-occurrence of the first negative PD pulse. This means that ϕ_1^- has a negative dependence on Q^+, i.e., $(Q^+\uparrow \Rightarrow \phi_1^- \downarrow)$. The data for $p_2(q_1^-|\phi_1^-,Q^+)$ show that q_1^- is positively dependent upon Q^+ for a fixed phase-of-occurrence ϕ_1^-, i.e., $(Q^+\uparrow \Rightarrow q_1^- \uparrow,\phi_1^-)$. The data for $p_1(q_1^-|\phi_1^-)$ show that the mean value of the first negative pulse amplitude increases with its phase-of-occurrence. This distribution is related to the unconditional distribution $p_0(Q^+)$ and the other conditional distributions shown in Fig. 22 by the expression

$$p_0(\phi_1^-)p_1(q_1^-|\phi_1^-)=\int_0^{\infty} p_0(Q^+)$$

$$p_1(\phi_1^-|Q^+)p_2(q_1^-|\phi_1^-,Q^+)dQ^+ . \qquad (14)$$
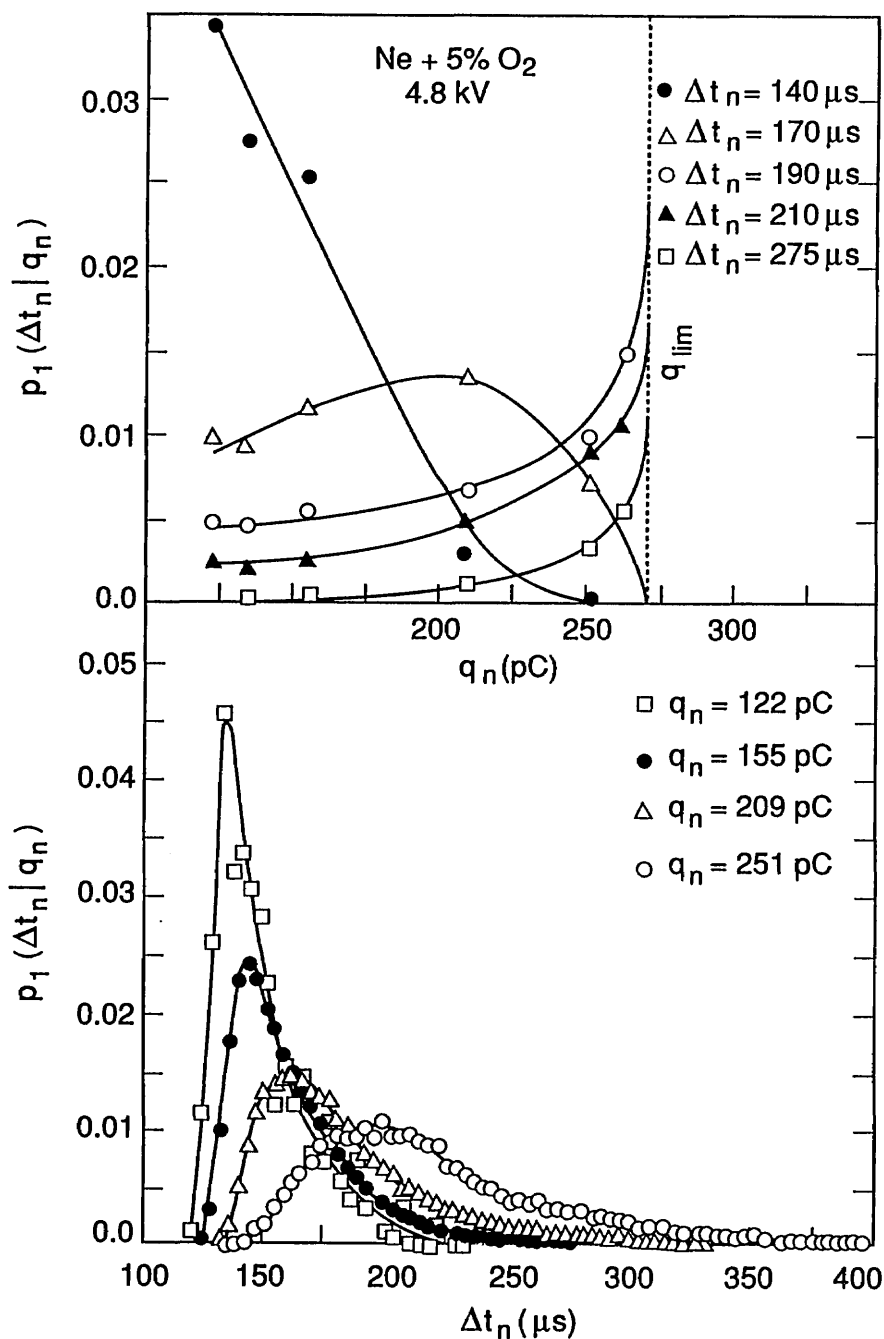
Fig. 21. Measured conditional time-separation distributions $p_1(\Delta t_n | q_n)$ at the indicated values for Δt_n or q_n for negative-corona discharge pulses generated using a point-plane electrode gap in a Ne + 5% O_2 gas mixture under conditions similar to those that yielded the data shown in Fig. 20 (see Ref. [1]).

The corresponding data for $p_0(Q^+)$ are not shown. At present, it has not been possible to obtain enough data on the required distributions under stationary discharge conditions to verify that Eq. (14) is indeed consistent with the experimental results.

It has recently been shown [33] that the types of stochastic behavior for ac-generated PD reported here are consistent with theoretical predictions derived from a Monte-Carlo simulation of the phenomenon. The primary long-term (cycle-to-cycle) mechanism for memory propagation is that due to
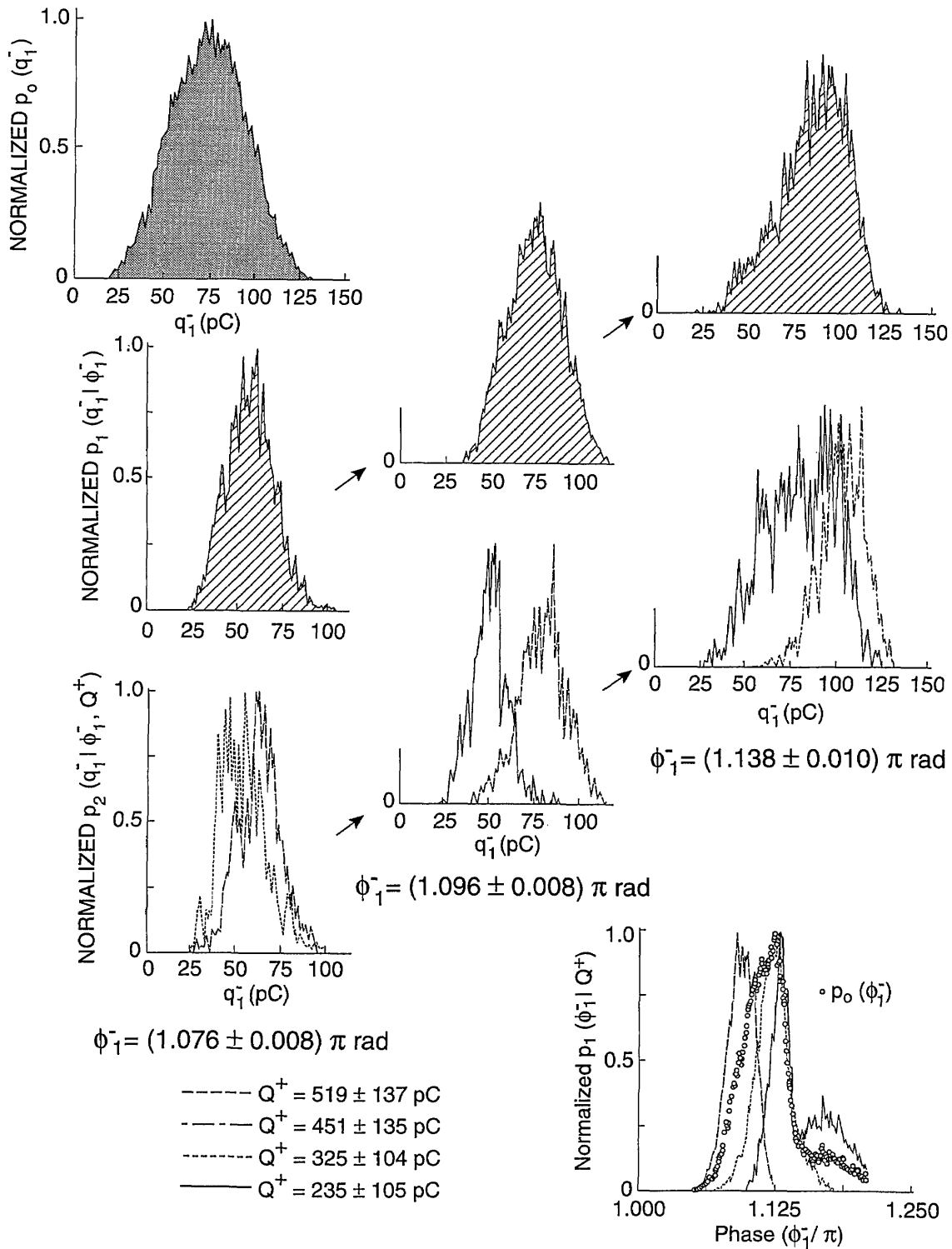
Fig. 22. Measured conditional and unconditional amplitude distributions of the first negative PD pulse at the indicated values of ϕ_1^- and Q^+ for a point-to-dielectric discharge gap spacing of 1.2 mm and an applied alternating voltage of 3.0 kV rms at a frequency of 200 Hz. Also shown are the conditional and unconditional phase-of-occurrence distributions for the same pulse. All distributions have been arbitrarily normalized to the maximum values.

electric charge accumulation on the dielectric surface during a PD event. It is well known that a quasi-permanent surface-charge distribution can exist on a solid insulating surface for times that are long compared to typical periods of the excitation voltage [34]–[37]. A significant fraction of the charge deposited on a dielectric surface by a PD event will remain to affect the local electric-field strength at the site where the next PD event is initiated. Both the probability for PD initiation and the distribution of the PD amplitudes depends at any given time on the local instantaneous electric-field strength. As in the case of dc-generated Trichel pulses, short-term pulse-to-pulse memory propagation can also exist for ac-generated PD. Mechanisms for memory propagation in this case could include moving ion space charge [1, 38], diffusion of metastable excited species [39], or a rapid redistribution of charge on a dielectric surface following a PD event [2, 40].

6. Calibrations and Sources of Error

In the discussion about the earlier version of the stochastic analyzer [24], several sources of systematic error were considered. These were primarily errors associated with the finite digital-delay generator time window and the finite reset time of the time-to-amplitude converter. These among other sources of error need to be considered in making interpretations of the measured distributions and in judging the validities of consistency analyses performed using relationships like Eqs. (7), (8), and (13). It is, for example, important in considering the use of Eq. (7) in checking consistency among the measured distributions $p_0(q_j)$, $p_0(\Delta t_j)$, and $p_1(q_j|\Delta t_{j-1})$ to know the extent to which $p_1(q_j|\Delta t_{j-1})$ represents the true conditional distribution for a fixed Δt_{j-1} [see Eq. (9)]. It is also important that measurements of Δt_j using a TAC and the determination of Δt_{j-1} using the combined DDG and Δt control logic yield identical time separations. Any error in one of these circuits relative to the other can cause difficulties in performing the integration implied by Eq. (7). Thus, for example, it is generally necessary to make corrections for the delay τ_2 introduced by the Δt control logic circuit (see Fig. 10). In this section we consider the possible sources of error in the measurement of various amplitude, phase-of-occurrence, time-separation, and integrated pulse (charge) distributions that can be measured with the system described above. Methods for calibration and testing of system performance are also discussed.

6.1 Amplitude Distributions

6.6.1 Pulse Shape Considerations

The method for calibration of pulse amplitudes for PD has been described previously [27]. One could, in the simplest case, directly apply pulses of a known amplitude to the input of the system (amplifier A1 of Figs. 3 and 4) and then record the MCA channel numbers corresponding to pulses of different amplitude. In most cases, however, it is desirable that the simulated input pulses used for calibration be similar in shape to those observed for the phenomenon of interest. This is especially required in the case of partial-discharge measurements where the amplitude of the recorded PD event is supposed to be proportional to the discharge intensity. It has been shown [1, 27] that, for the types of PD phenomena considered in the previous section, the recorded pulse amplitude is proportional to the net charge generated during the pulse provided the width of the impulse response for the detection system is very large compared to the intrinsic width of a typical discharge pulse. Under this condition, the shape of the recorded pulse is governed primarily by the impulse response of the detection circuit. The width of the impulse response for the detection system used to obtain the data in Figs. 20–22 is approximately 1.5 μs compared to a typical intrinsic PD pulse width of 1 to 11 ns.

Pulses for some types of PD phenomena such as pulsating corona in air are known to have tails that are long compared to the 1.5 μs impulse response width corresponding to the conditions under which the data in the previous section were taken. In such cases, not only is the measured pulse amplitude no longer directly proportional to the total charge generated by the PD event, but there may also exist the possibility that the system will sample the tail of the pulse one or more times in addition to its peak value. As noted in our earlier work [27], this problem can occur if the system sampling rate, governed primarily by the dead time of the MCA, is sufficiently high. (The MCA dead time is approximately 2 μs for the system used in this work). If this problem occurs, the measured amplitude distribution will be artificially enhanced at the low-amplitude end due to recording of the tails. A similar problem of pulse amplitude distribution distortion is known to occur in cases where the PD occurs as bursts of pulses in which: 1) the spacing between pulses is comparable to or shorter than the detector impulse response time or MCA dead-time, i.e., the system sampling time; 2) the duration of the burst is comparable to or longer than the system sampling time; and 3) there is a high degree

of correlation among the amplitudes of pulses within a burst. Such short-duration, burst-type PD pulses for which pulse amplitudes are highly correlated are known to occur under some conditions [4, 27, 41].

The accidental sampling of pulse tails can also be a problem when measuring conditional pulse-amplitude distributions as discussed in our earlier work [24]. In this case, a problem arises if the MCA is gated on by the Δt control logic at precisely the time when an event pulse is decaying, i.e., after a peak has occurred. The problem has been minimized in the present system by a combination of shaping the pulses that enter the MCA and by minimizing the delay time $\Delta t'$ indicated in Fig. 10 as determined by the one shots OS2 and OS3 in Fig. 9. These adjustments were sufficient to yield acceptable results for the types of PD phenomena considered in this work. Complete elimination of this problem is difficult, but can be at least partially achieved by modification of the Δt control logic so that it senses if a pulse has occurred within a short time of approximately one pulse width before the DDG3 pulse is returned to input f'' in Fig. 9. If a pulse does occur within that time, then a condition can be set to force a delay in the opening of the MCA gate at output h.

6.1.2 Effect of Amplifier Nonlinearities

Another possible source of distortions in measured conditional or unconditional pulse-amplitude distributions is that associated with nonlinearities in the gains of pulse amplifiers used in the detection circuitry or elsewhere in the measurement system, e.g., amplifier A1 in Figs. 3 and 4. Figure 23 shows typical examples of calibration curves used in analyzing the data on pulse-amplitude distributions such as those shown in Figs. 20 and 22. Shown are plots of amplitude in charge (pC) versus MCA channel number for two different ranges of amplitude and for two different gain settings (g_1 and g_2) of the amplifier A1 for the same input amplitude range. The onset of gain saturation in the preamplifier that detects a pulses is indicated by the vertical arrow pointing to a place on the curve corresponding to the highest gain and highest amplitude range.

It is desirable that the response of the pulse amplifier be as linear as possible. Deviations from linearity introduce complications in determining the true amplitude distribution from the measured data as will be shown below. The data recorded by the MCA can be represented by the array of numbers $N(k)$ where k is the channel number and $N(k)$ is the number of events stored in k. For a 256
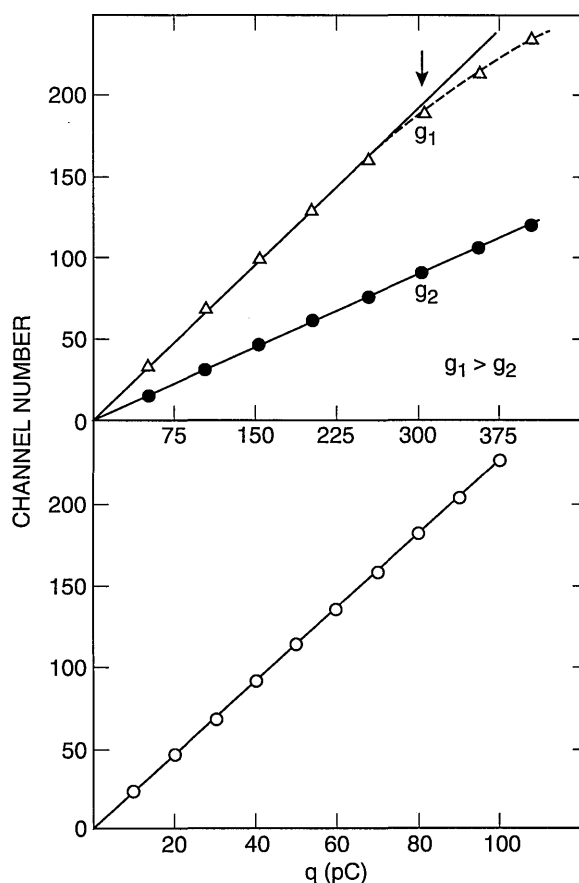
Fig. 23. Examples of amplitude-calibration curves for two different ranges of amplitudes and two different amplifier gains, g_1, and g_2, that apply to the measurement of PD pulse-amplitude distributions. The vertical arrow indicates the onset of gain saturation for the highest range and gain g_1.

channel MCA, k is restricted to integer values between 1 and 256. From calibration data such as shown in Fig. 23, one can relate the $N(k)$ data to the true amplitude distribution by

$$N(k)\Delta k = N_0 \int_{q(k_L)}^{q(k_U)} p_j(q)\,dq \qquad (15)$$

where N_0 is a normalization constant and $p_j(q)$ denotes a "true" jth order conditional amplitude distribution. If a single channel width is assumed so that $\Delta k = 1$, then $q(k_U)$ and $q(k_L)$ are defined here to correspond respectively to the values $k_U = k + \frac{1}{2}$ and $k_L = k - \frac{1}{2}$.

If the pulse amplification is linear, we can write

$$k = \alpha_0 + \alpha_1 q, \qquad (16)$$

where α_0 and α_1 are constants. If $p_j(q)$ is slowly varying over the interval $[q(k_U), q(k_L)]$ so that

$$\frac{p_j(q(k_U)) - p_j(q(k_L))}{p_j(\bar{q})} \ll 1, \qquad (17)$$

where $\bar{q} \equiv [q(k_U) + q(k_L)]/2$, then in the linear case

$$N(k) \approx N_0 p_j(\bar{q})[q(k_U) - q(k_L)] \qquad (18)$$

$$= N_0 \left(\frac{1}{\alpha_1}\right) p_j(\bar{q}). \qquad (19)$$

Equations (18) and (19) imply that $N(k)$ versus k is a discretized approximation to the true distribution $p_j(q)$.

For cases where the response is nonlinear, Eq. (19) is not valid and even Eq. (18) may fail to be a good approximation. If a quadratic dependence is included in Eq. (16) by adding a term $\alpha_2 q^2$ to the right-hand side, then the factor of $(1/\alpha_1)$ in Eq. (19) must be replaced with the factor $[1/(\alpha_1 + 2\alpha_2 \bar{q})]$ which depends on $\bar{q}$. For a sufficiently large quadratic contribution, it is necessary to consider this $\bar{q}$ dependent factor in attempts to estimate the $p_j(\bar{q})$ distribution from the raw $N(k)$ versus k data.

Under conditions of severe nonlinearity, it may become impossible to extract meaningful information about $p_j(q)$ from the MCA data. One such case is that encountered when the input amplifier gain approaches saturation. As an example of this case we consider an amplifier that begins to saturate for $q \geq q_s$. The calibration curve for this case is represented mathematically by:

$$k = \alpha_0 + \alpha_1 q, q < q_s \qquad (20)$$

$$k = \alpha_0 + \alpha_1'[1 - \exp(-\beta q)], q > q_s, \qquad (21)$$

where α_1' and β are constants and the gain is assumed to be linear for $q < q_s$. In order that both k and dk/dq be continuous at $q = q_s$, the coefficients must satisfy the relationships

$$\alpha_1' = \frac{\alpha_1 q_s}{[1 - \exp(-\beta q_s)]} \qquad (22)$$

and

$$(\beta q_s + 1)\exp(-\beta q_s) = 1. \qquad (23)$$

In the region of saturation $(q \geq q_s)$ we have

$$\frac{dk}{dq} = \alpha_1 \exp[-\beta(q - q_s)]. \qquad (24)$$

Equation (24) implies that for a fixed increment of channel number, e.g., $\Delta k = 1$, the difference between $q(k_U)$ and $q(k_L)$ increases exponentially with q, i.e.,

$$q(k_U) - q(k_L) \sim \exp[\beta(q - q_s)]. \qquad (25)$$

In this case, Eq. (18) may not hold and, in general, one must resort to Eq. (15) to relate $N(k)$ to $p_j(q)$. The range of q values over which Eq. (15) must be integrated can become large enough under some conditions to prevent the determination of reasonable estimates for $p_j(q)$ from the MCA data. Generally, the effect of amplifier saturation is to cause $N(k)$ to become artificially enhanced at large values of k. The problems associated with saturation can usually be avoided by making careful adjustments of amplifier gain.

A reasonable estimate of the true amplitude distribution also requires that the amplitude increment, $q(k_U) - q(k_L)$, associated with the width of a single channel be small compared to the characteristic width of the distribution. This can usually be assured by appropriate adjustment of the amplifier gain and MCA pulse discrimination level that respectively determine the parameters α_1 and α_0 in Eq. (16). There may exist cases, however, where the ability to make a precise determination of conditional or unconditional distributions is severely limited by the inherent resolution of the MCA.

6.1.3 Noise Broadening Under low signal-level conditions, distortion of the measured amplitude distributions can result from effects of noise. Specific sources of noise are not identified here, but they could simply be those associated with normal amplifier operation. The type of noise considered in the present discussion is often referred to as "white noise." The noise is assumed to have constant statistical characteristics during the time of a typical measurement, i.e., it is assumed to be stationary.

Not considered in this discussion are erratic or time-dependent noise such as might appear as random or phase correlated pulses generated by

pick-up from sources external to the system of interest. In cases where such externally produced impulses cannot be eliminated by adjusting the amplifier or MCA discrimination levels, it is possible that these impulses will introduce severe distortions, especially if they are narrowly distributed in amplitude, phase, or frequency. Elimination of interference from impulse noise sources can be achieved under some conditions by using shielding or digital-filtering techniques [42, 43]. Discussion of these techniques goes beyond the scope of the present work.

The imposition of a constant background noise on the detected impulse signals introduces a broadening in the amplitude distributions recorded by the MCA. The broadening effect can be estimated from the convolution

$$P_j(\overline{q}) = \int_{-\infty}^{+\infty} p_j(q')f(\overline{q} - q')dq', \qquad (26)$$

where $P_j(\overline{q})$ is the broadened distribution and $f(\overline{q} - q')$ is a function that represents the statistical distribution about a mean value, $\overline{q}$, due to noise. In cases where the noise is inherent in the measurement system, the form of $f(\overline{q} - q')$ can sometimes be estimated from the calibration data. Figure 24 shows an example of a set of calibration data recorded by the MCA under conditions where pulses of known amplitude, $\overline{q}_i (i = 1,2,...)$, are injected from the calibration source during fixed intervals of time. If noise were not present, counts would be recorded in only one channel of the MCA for each value of q_i. The fact that counts appear in 12 or more channels for the data shown in Fig. 24 means that there is some broadening due to the presence of noise. In most cases like that shown in Fig. 24, the noise can be approximated by a Gaussian function, i.e.,

$$f(\overline{q} - q') = (\pi w)^{-\frac{1}{2}} \exp[-(\overline{q} - q')^2/w], \qquad (27)$$

where the width, w, is independent of $\overline{q}$. Broadening due to noise can be significant if the condition $\Delta q \gg w$ is not satisfied, where Δq is the characteristic width of $p_j(q)$. If noise broadening is determined to be significant, then it may be possible to develop a deconvolution procedure using Eqs. (26) and (27) to obtain an improved estimate of $p_j(q)$ from the measured data recorded by the MCA. No attempts have been made to implement noise deconvolution procedures in the present work.
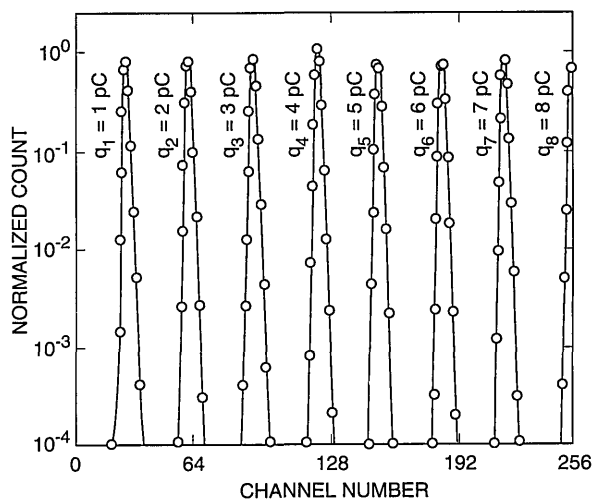
Fig. 24. Amplitude-calibration data recorded by the MCA that show broadening due to noise.

6.2 Amplitude Sum (Integrated-Charge) Distribution

The measurement of integrated-charge distribution, $p_0(Q^\pm)$, for a specified phase region (positive or negative half-cycle) is subject to the same errors considered above for pulse-amplitude distribution, e.g., effects of amplifier nonlinearities and noise broadening. In addition to these, there are other mechanisms for introducing systematic errors that can result from the operating characteristics of the gated integrator and its associated input amplifier. These possible sources of error are examined here. Methods for calibration of the integrator that can reveal systematic errors and precautions that can be taken to ensure proper operation of this circuit are also considered.

It should first be realized that the output of the pulse amplifier (A2 in Fig. 4) is a rectangular pulse of constant width independent of the shape of the input pulse. The amplitude of the output pulse is directly proportional to the amplitude of the input pulse provided the input pulse lies above a critical value q_d (discrimination level). The output of the amplifier, q, is related to the input, q', by

$$q = g_{A2}q', q' > q_d' \qquad (28)$$

$$q = 0, q' < q_d', \qquad (29)$$

where g_{A2} is a constant corresponding to the gain of A2.

The input amplifier A2 essentially acts like a peak detector. By using this type of amplifier as an

input to the integrator, the output pulse of the integrator is forced to be proportional in amplitude to the sum of the *amplitudes* of the pulses appearing at the input to A2 consistent with Eq. (4). The integrator, therefore, does not yield an output that is a true measure of the integrated current associated with the event pulses as given by

$$Q^{\pm} = \sum_j \int_{t-\tau_j}^{t+\tau_j} I_j^{\mp}(t') dt', \qquad (30)$$

where $I_j^{\mp}(t')$ is the instantaneous current of the jth pulse and τ_j is the duration of the pulse defined such that $I_j^{\mp}(t') \neq 0$ only for times in the interval $t + \tau_j > t' > t - \tau_j$. The value of $Q^{\pm}$ is directly proportional to that given by Eq. (4) only if all pulses have the same shape. The error in the determination of true integrated charge is approximately given by the difference

$$\Delta Q^{\pm} = \sum_j \left[q_j^{\mp} - \int_{t-\tau_j}^{t+\tau_j} I_j^{\mp}(t') dt' \right], \qquad (31)$$

where the values for $q_j^{\mp}$ are determined by the calibration of amplitude in terms of charge-per-pulse under conditions where pulse shape is governed by the detector impulse response (see previous section).

For cases where there may be events having pulse durations, τ_j, that exceed the width of the impulse response, the sign of the error $\Delta Q^{\pm}$ is most likely negative, i.e., the measurement preferentially tends to underestimate the integrated charge. An additional contribution to a negative error can occur if there are events with amplitudes lower than the discrimination level q_d^i defined in Eq. (28). The integrated charge for these events is simply not included in the sum of amplitudes, Eq. (4).

Calibration of the integrator requires the use of a gated pulse generator that produces a burst of pulses only during the time that the integrator is gated on as shown in Fig. 25. If N_1 calibration pulses of known amplitude q_c are applied during the gate interval, then the output pulse of the integrator should ideally have an amplitude directly proportional to the product $N_1 q_c$. This means that the output should be independent of the number of pulses used if q_c is maintained at a value of V_c/N_1

where V_c is constant. Thus, if N_1 is increased by a factor of two, the integrator should give the same output provided q_c is correspondingly reduced by a factor of one half.
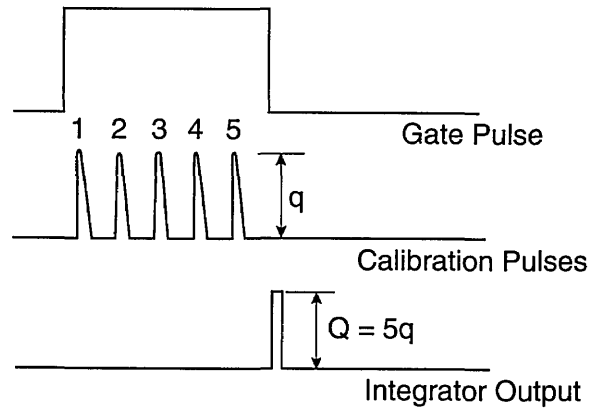
Fig. 25. Pulse timing diagram that applies to a calibration of the gated integrator. The output of the integrator should ideally be a pulse with an amplitude directly proportional to the sum of the amplitudes of the calibration pulses that occur during the gate pulse.

To ensure proper operation of the integrator, the dc bias level at the output of A2 should be adjusted to zero. After this adjustment is made, the offset voltage of the integrator (amplifier A1 in Fig. 18) should be set at a value that forces the integrator output pulse amplitude to be zero when no pulses are applied to the input, i.e, when $N_1 = 0$. This latter adjustment is required because the 0.01 μF integrating capacitor in Fig. 18 can acquire an initial small charge attributable to the transient voltage associated with the opening of the FET's T1 and T2. Failure to make these adjustments will allow systematic errors to occur in the measured integrated charge due to an offset, i.e., a nonzero intercept of the calibration curve.

Errors introduced by the presence of a finite offset are illustrated by the examples of calibration data shown in Figs. 26 and 27. Plotted in Fig. 26a is the amplitude (or equivalently charge) per calibration pulse, $q_c = Q^{\pm}/N_1$, versus the recorded MCA channel number per pulse, $N(k)$, for $N_1 = 1$ to 5. Figure 26 shows the corresponding calibration plot of $Q^{\pm}$ versus $N(k)$, again for $N_1 = 1$ to 5. The data in Fig. 26a tend to fall on a straight line given by

$$Q^{\pm}/N_1 = \eta_0 + \eta_1 N(k)/N_1, \qquad (32)$$

where η_1 is the slope and η_0 is the intercept corresponding to a constant offset voltage. The

corresponding integrator calibration curves are given by

$$Q^{\pm} = N_{\mathrm{I}}\eta_0 + \eta_1 N(k) . \tag{33}$$
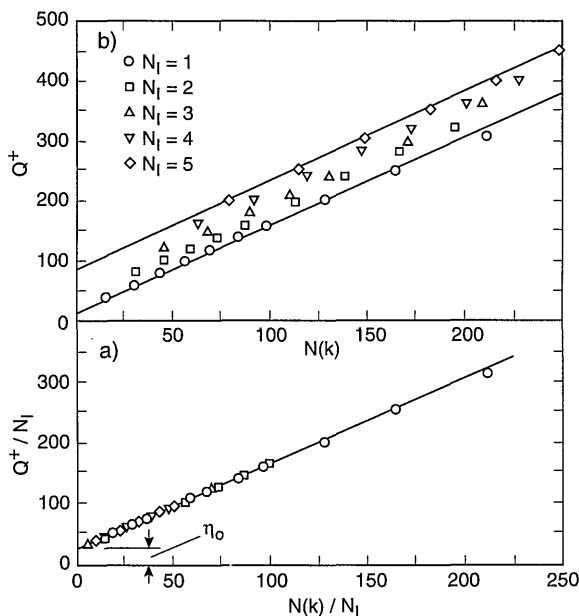
Fig. 26. Example of an integrator calibration performed under conditions where there is a finite offset corresponding to a non-zero intercept η_0 as shown in a). The calibration data in b) indicate the resulting uncertainty due to this offset (range of Q^+ defined by the solid lines).

Consistent with the data shown in Fig. 26b, the intercepts for the $Q^{\pm}$ versus $N(k)$ curves increase with increasing N_{I}. Under these operating conditions, there is an uncertainty of $\eta_0 \Delta N_{\mathrm{I}}$ in the amplitude sum (integrated charge) due to the offset, where ΔN_{I} is given by

$$\Delta N_{\mathrm{I}} = N_{\mathrm{I}}(\max) - N_{\mathrm{I}}(\min) . \tag{34}$$

Here, $N_{\mathrm{I}}(\max)$ and $N_{\mathrm{I}}(\min)$ are respectively the maximum and minimum number of events that are likely to be recorded within the integrator gate interval (Δt_{I} in Fig. 19). The solid lines in Fig. 26a represent the error limits for the case considered when $N_{\mathrm{I}}(\max) = 5$ and $N_{\mathrm{I}}(\min) = 1$. Figure 27 shows how this systematic error can be reduced if care is taken to minimize the offset so that $\eta_0 \approx 0.0$. In general, all stages of amplification should be adjusted individually to eliminate offsets. Further reduction in the error can be achieved by giving the greatest weight to calibrations made using values for N_{I} that equal the mean number of experimentally observed events within the integrating interval.
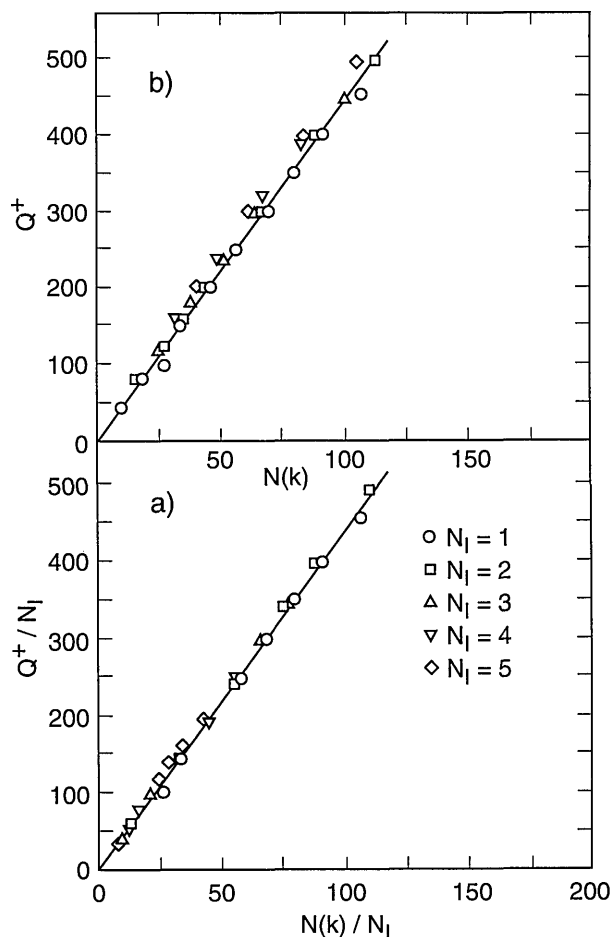
Fig. 27. Example of an integrator calibration performed under conditions of zero offset (zero intercept, η_0) as shown in a); and corresponding error reduction as seen in b).

6.3 Time-Interval and Phase-of-Occurrence Distributions

Systematic errors that can occur in the measurement of pulse time-separation distributions were analyzed in our earlier work [24]. It was noted that the measured time-separation distributions can become distorted if: a) a significant fraction of the time separations are less than the time-to-amplitude converter reset time, Δt_r, and b) there are correlations among successive time separations. The reason why distortions are introduced under these conditions can be understood from a consideration of the example illustrated in Fig. 28. It is assumed that the phenomenon of interest appears in the form of pulse bursts where there is an ordering of pulse time separations within a burst such that the first separation is on the average smaller than the second and so on. This type of behavior occurs, for example, in the case of burst-type positive-corona

pulses generated in sulfur hexafluoride using point-plane electrode gaps [27].
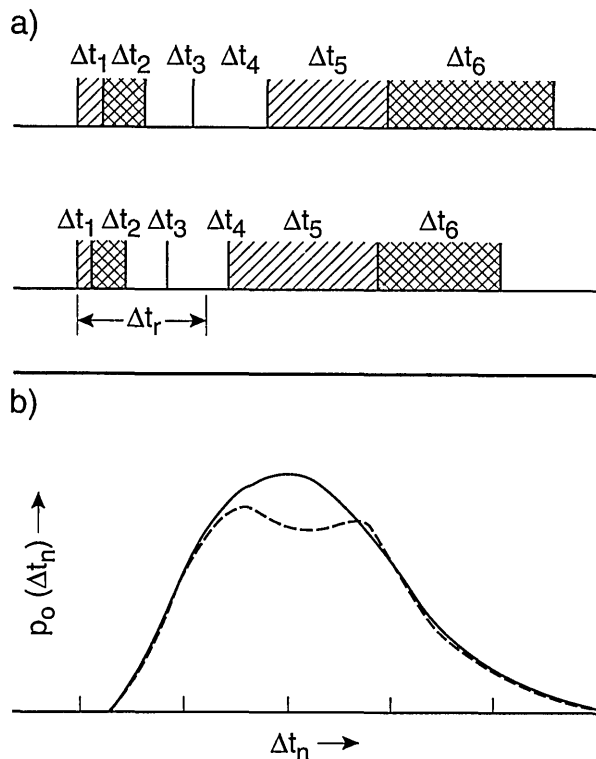
Fig. 28. Possible distortion of a measured time-separation distribution, $p_0(\Delta t_n)$, for pulse bursts due to the finite TAC reset time Δt_r.

Figure 28a shows pulse diagrams for two different bursts of 7 pulses each with the indicated successive time separations Δt_1, Δt_2,... and the TAC reset time Δt_r. It is assumed that two TACs are used for the measurement as shown in Fig. 3. The shaded time separations are those actually recorded by the system, i.e., Δt_1, and Δt_5 are measured by TAC1 and Δt_2 and Δt_6 are measured by TAC2. The time separations Δt_3 and Δt_4 are not recorded because they occur before the TAC has had time to reset. The failure to record these separations causes the measured distribution to deviate from the true distribution as shown in Fig. 28b. This limitation can be overcome to some extent by using multiple TACs as discussed in the next section.

In the case of conditional time-interval or phase-of-occurrence distributions, distortions can also occur if the range of values for the "fixed" variable are not sufficiently well restricted. As noted above

[see Eq. (9)], the necessity of using a finite window size for the fixed variable introduces a broadening of the distribution. The problem has already been noted for the measurement of conditional pulse-amplitude distributions [24]. Unlike the broadening due to noise, the broadening introduced by a finite window can be asymmetrical with a resultant apparent shift in the associated mean value. Examples of asymmetric broadening due to an increase in window for the variable Q^+ are shown in Fig. 29 for measured conditional distributions $p_1(\phi_{\bar{1}} | Q^+)$ corresponding to the phase of the first negative PD pulse generated in a point-dielectric discharge gap. In general, it is desirable to keep the window size to the minimum required to obtain acceptable statistics within a reasonable time. Excessive distortions due to finite window size will invalidate consistency analysis using the various integral relationships among measured conditional and unconditional distributions, e.g., using Eqs. (7), (8), (13), and (14).

7. Limitations, Extensions, and Alternatives

7.1 Limitations

It was noted at the outset that the system described in this work is optimally designed to investigate the stochastic properties of ac or dc generated PD pulses with repetition rates between 50 and 5×10^4/s. The lower limit on pulse rate is determined by the acceptable times within which observations can be made that will yield statistically significant results. If the phenomenon of interest is stationary over the time of observation, then there is, in principle, no lower limit on the pulse rate that could be observed. However, if the time between pulses exceeds the range of a TAC (typically 1 s), then time intervals must be measured by another method, e.g., using a digital clock with a gated pulse counter. For extremely low pulse rates (less than 1 per min) it may be more efficient to simply perform a statistical analysis of recorded data.

The upper limit on the rate of observed pulses is imposed by time restrictions inherent to the electronics. Specifically, there are limits due to: 1) the finite reset time of the TAC, 2) the dead-time of the MCA, 3) built-in delays in the SCA and Δt control logic circuits, and 4) the inherent impulse response of the pulse detection and amplifier network. It may be possible by using a broad-band detector and faster electronics to increase the range of applicability by an order-of-magnitude, i.e., to 5×10^5/s. However, this may introduce
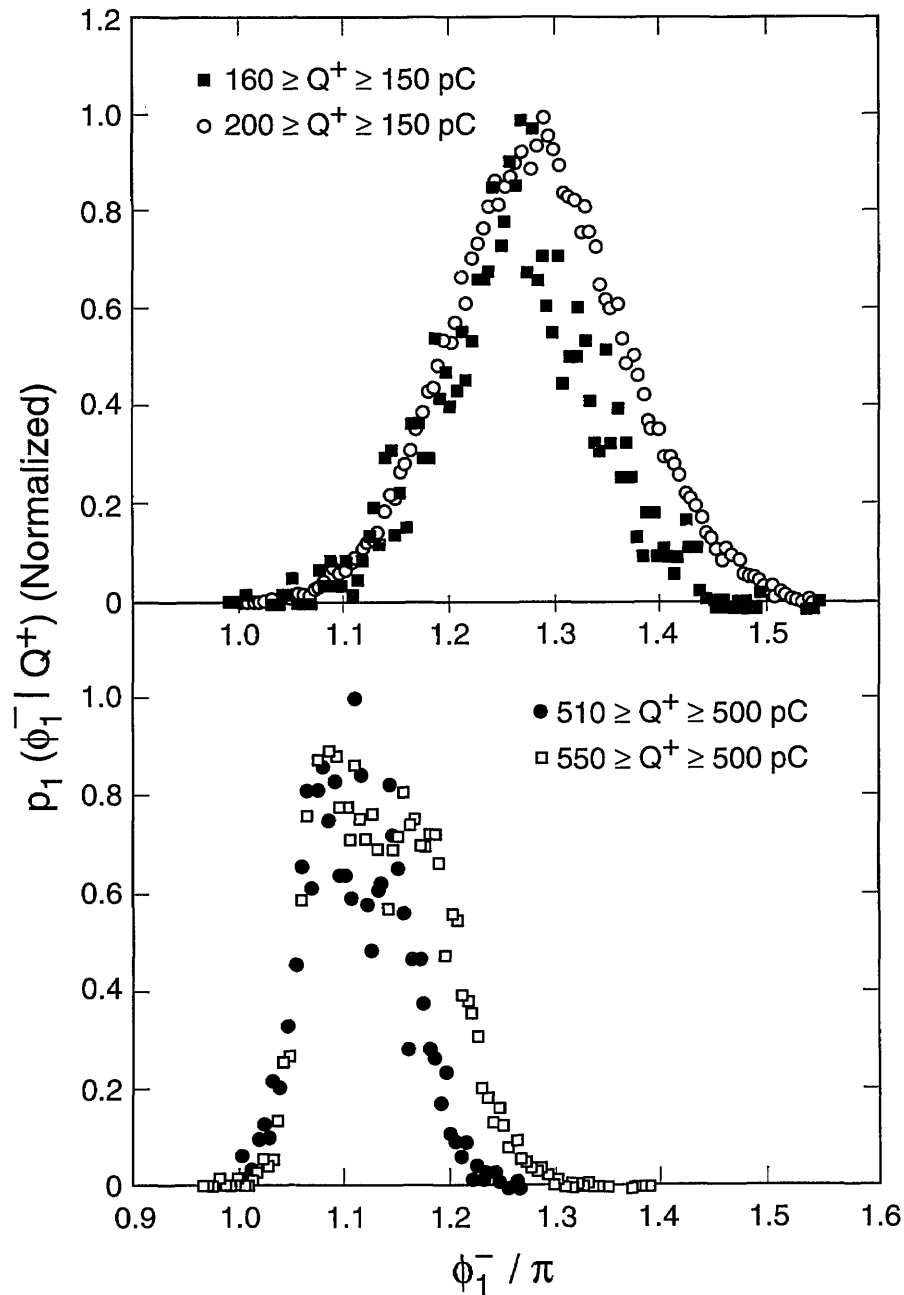
Fig. 29. Examples of data for measured conditional phase-of-occurrence distributions $p_1(\phi_1^-|Q^+)$ that show asymmetric broadening due to a finite window for the "fixed" variable Q^+.

added complexity and cost that would make alternative methods appear more attractive such as the "software" approach considered in Sec. 7.3.

Although it was assumed here that pulse amplitude (or the sum of successive pulse amplitudes) is the appropriate "mark" for characterizing the intensity of the phenomenon, there may exist cases where other marks such as pulse area or pulse-shape parameters are more appropriate indicators of "intensity." The system documented here may still be applicable to these cases provided the mark can be converted to a pulse with an amplitude that is directly proportional to the "size" of the mark.

In principle, there is no upper limit to the size of a mark that can be measured. In some cases it may be necessary to restrict the amplitude of an event pulse by a linear attenuation network so that it does not exceed the voltage range acceptable to the MCA (0 to 8 V in the present system). If the dynamic range of pulse amplitudes is very large (two or more orders-of-magnitude), then it may be necessary or desirable to replace the linear input pulse amplifier with a logarithmic amplifier.

The lower limit on acceptable pulse amplitude is simply governed by signal-to-noise ratio. As the broadening due to noise (see Sec. 6.1.3) becomes comparable to the width of the observed distribution, it becomes increasingly difficult to extract meaningful information about memory effects from the data.

It was noted previously that when broadening due to noise or restricted variable window size is significant, it may no longer be possible to perform a consistency analysis among various measured distributions using the integral relationships that connect these distributions, e.g., Eq. (7). It may still be possible, nevertheless, to use the data on conditional distributions to establish the *existence* of memory propagation. The existence of memory propagation can be unequivocally established if it can be shown, for example, that the conditional distributions $p_1(q_j | \Delta t_{j-1} \in (\Delta t_a, \Delta t_b))$ and $p_1(q_j | \Delta t_{j-1} \in (\Delta t_{a'}, \Delta t_{b'}))$ do not coincide under at least one condition where the corresponding ranges of the time intervals $(\Delta t_a, \Delta t_b)$ and $(\Delta t_{a'}, \Delta t_{b'})$ are different. In order to determine this lack of coincidence, it is necessary: 1) to acquire enough data to demonstrate a statistically significant difference between the two distributions, and 2) to acquire the data under conditions where the phenomenon is stationary. The effects of nonstationary behavior can be minimized if the data for the two conditional distributions can be accumulated simultaneously. Unfortunately, in the present system, which has only one Δt control logic circuit and one MCA, it is not possible to make simultaneous measurements of two distributions of the same type. The system can be operated, however, to alternately accumulate data in two different 256-channel segments of the 1024-channel MCA for two different ranges of the fixed variable. By periodic switching back and forth between the two segments, it may be possible to "average out" effects of nonstationary behavior. The existence of nonstationary behavior can often be detected from periodic monitoring of unconditional distributions such as $p_0(q_j)$ or $p_0(Q^{\pm})$ for

which statistically significant data can be accumulated in much shorter times than for conditional distributions for which pulse count rates are lower. It has been shown [1, 4] that the profiles of unconditional distributions tend to be more sensitive to nonstationary behavior than the profiles of conditional distributions.

It should be realized that, in general, the time required to obtain statistically significant data for a distribution can increase rapidly as the number of restrictions imposed by the fixed variables is increased and as their ranges are reduced. This is perhaps the most stringent limitation inherent not only to this measurement system but also to stochastic analysis in general. For the types of pulsating PD phenomena investigated with this system, it has usually not been possible to obtain enough data with adequate statistics for conditional distributions higher than second order.

7.2 Extensions

Some of the limitations mentioned in the previous and earlier sections can be overcome (or at least reduced) by introducing various extensions or expansions to the existing measurement system. One obvious extension would be to introduce additional MCAs with associated circuitry to allow simultaneous measurement of two or more distributions. This would not only reduce the total data acquisition time, but would also allow better monitoring of effects due to nonstationary behavior. Since nonstationary behavior in PD phenomena is often a consequence of discharge-induced modifications of the discharge gap, e.g., changes in rates of electron emission from surfaces, multiple MCA measurement capability might make the system more useful as a diagnostic of insulation aging.

The previously noted limitations on the measurement of time or phase separation distributions imposed by the finite TAC reset time can be overcome by incorporating more TACs in series with an associated pulse sorting circuit so that each TAC measures a different successive time interval. If instead of using only two TACs one uses $2n$ TACs, where $n > 2$, then the minimum time separation that can be measured without introducing errors (see Sec. 6.3) is reduced from $\Delta t_r / 2$ to $\Delta t_r / 2n$.

Of course, the introduction of added instrumentation such as MCAs and TACs significantly increases the cost of the system. In some cases this added cost may be more than compensated for by the reduction in time required to acquire and

analyze the data. Additional time savings may be achieved by automating the system to allow not only the simultaneous measurement of more than one distribution but also real-time calibration, data analysis, and optimization of time spent where needed to obtain the best statistics.

Finally, it should be noted that although the system described here has only been applied to the measurement of pulse sequences in real time, it is also possible to use it for stochastic analysis of pre-recorded pulses. This merely requires that the source of the input pulses be derived from an electronic recording device operated in the "play-back" mode. As will be argued in the next section, it should be possible to use prerecorded data derived from computer simulations to test the overall system performance. It is, of course, desirable that the simulation produce pulses with known stochastic properties, i.e., conditional distributions that mimic those of the phenomena under investigation, and that simulated pulses have an amplitude and shape similar to experimentally observed pulses. The use of the system described here to perform analysis on prerecorded data allows an obvious extension to pulses with repetition rates that are higher or lower than the ranges which are normally acceptable. However, one should consider whether or not it may be more efficient to analyze prerecorded data directly using computer software such as considered in the next section.

7.3 Alternatives

One of the primary advantages of the system described in this work is the ability to measure the stochastic properties of a pulsating phenomenon in real time. It allows one to view on a computer output device (video monitor) the development of conditional or unconditional distributions as the data are acquired. With this capability, it is possible for the operator to determine quickly the existence of memory effects and to make decisions on the conditions that should be selected to yield the most interesting data.

The system, in its present form, is designed to be a *research tool* for use in investigating memory propagation in pulsating phenomena. It is assumed that it is operated by those who have a thorough understanding of the phenomenon under investigation. Because this is a highly "interactive" system, the quality of the information acquired from the measurements will be determined to a large extent from the judgments of the operator. It may be possible to construct an "automated" real-time

stochastic analyzer based on the measurement concepts introduced here. Some aspects of the present system could, for example, be incorporated into advanced partial-discharge measurement systems that would allow the possibility for meaningful pattern recognition needed to identify types of discharge sites.

Another advantage of a real-time measurement system is that it overcomes problems of storing large data files. For example, the measurement of some of the second-order distributions shown in Figs. 22 and 23 required ten or more minutes of data acquisition time. This means that only a very small fraction of the total number of discharge events that occurred during the measurement time were actually recorded. A record of all discharge events that occurred in a typical 10 min segment would generally contain data for more than 10^9 pairs of numbers. Within the times required to obtain reasonably good statistics on higher-order conditional distributions, it is possible to generate data files containing all events that exceed mini-computer storage capacity. Analysis could then only be performed using either "main-frame" type computers or appropriately segmented data files in smaller computers.

The obvious disadvantage of the present measurement system is that it does not make efficient use of the available data. In the measurement of conditional distributions, most of the information about the impulse events is discarded. Once the data are discarded, they can no longer be retrieved for subsequent analysis. The expense of introducing additional MCAs in parallel to enhance the information retrieval efficiency can make the cost of the system prohibitive.

In cases where either the amount of data is severely limited or the phenomenon is highly non-stationary, it may be essential to consider all of the available data. There may also be other cases where it is necessary to work with prerecorded data due to externally imposed geometrical or time constraints.

The most efficient use of available data in such cases can, at least in principle, be achieved using an alternate approach that places more reliance on computer software. An example is given below of an algorithm that was developed to acquire data on conditional and unconditional distributions from a Monte Carlo simulation of ac-generated partial discharges. Details of the theoretical model upon which the simulation is based are given elsewhere [33] and will not be covered here. It need only be said that the simulation produces a sequence of

phase-correlated pulses with stochastic properties similar to those observed for PD generated by applying an alternating voltage to a point-dielectric electrode configuration [3].

A partial listing of a FORTRAN-77 routine used to sort data in real-time for determination of the distributions that apply to simulated PD is given in Table 6. The specific distributions considered in this table are the unconditional and conditional phase-of-occurrence distributions for the i th negative PD pulse, i.e., $p_0(\phi\bar{\imath})$ and $p_1(\phi\bar{\imath}|Q^+)$.

Table 6. Partial listing of a FORTRAN 77 routine for determining the distributions $p_0(\phi\bar{\imath})$ and $p_1(\phi\bar{\imath}|Q^+)$ from numerical data on $\phi\bar{\imath}$ and two windows for Q^+, i.e., $Q^+ \in (Q_1\mathrm{u}, Q_1\mathrm{L})$ and $Q^+ \in (Q_2\mathrm{u}, Q_2\mathrm{L})$.

```
C   POPI = ARRAY FOR UNCONDITIONAL PHASE DIST.
C   P1PI1, P1PI2 = ARRAYS FOR CONDITIONAL PHASE DIST.
C   QPOS = INTEGRATED POSITIVE CHARGE (AMPLITUDE SUM).
C   QPU1, QPL1 = LIMITS ON WINDOW-1 FOR QPOS.
C   QPU2, QPL2 = LIMITS ON WINDOW-2 FOR QPOS.
C   IN = NEGATIVE PULSE INDEX NUMBER.
C   CHANNEL = INTEGER BETWEEN 0 AND 200.
C   PHASE = PHASE OF NEGATIVE PULSE.

    CHANNEL = NINT(200*PHASE)
    POPI(CHANNEL,IN,0) = POPI(CHANNEL,IN,0) + 1
    IF(QPOS.LT.QPU1) THEN
     IF(QPOS.GT.QPL1) THEN
      P1PI1(CHANNEL,IN,,0) = P1PI1(CHANNEL,IN,0) + 1
     END IF
    END IF
    IF(QPOS.LT.QPU2) THEN
     IF(QPOS.GT.QPL2) THEN
      P1PI2(CHANNEL,IN,0) = P1PI2(CHANNEL,IN,0) + 1
     END IF
    END IF
```

The first statement in this routine converts the value of the normalized phase $(\phi\bar{\imath}/2\pi)$ to the nearest integer value between 0 and 200. It thus performs essentially the same discretization of the data as in a 200-channel MCA. The assigned integer value is then used to identify elements of three-dimensional integer arrays corresponding to particular distributions. In the case of the unconditional phase distributions, the array element is increased by 1, i.e., by one pulse count. In the case of the conditional distributions, the array elements associated with $p_1(\phi\bar{\imath}|Q\mathrm{u})$ and $p_1(\phi\bar{\imath}|Q\mathrm{L})$ are incremented by 1 only if the values of $Q\mathrm{u}$ and $Q\mathrm{L}$ lie within specified ranges. An example of the results from this routine are shown in Fig. 30 together with the corresponding data for $p_0(Q^+)$ that indicate the ranges selected for $Q\mathrm{u}$ and $Q\mathrm{L}$. It is seen that the conditional distributions from this simulation show the same stochastic trends seen for the experimental data in Fig. 22, i.e., $(Q^+ \uparrow \Rightarrow \phi\bar{\imath} \downarrow)$ for all values of i.

The routine shown in Table 6 is used to analyze simulated PD pulses in real time. The value for Q^+ is stored from the previous half-cycle. Each time a negative pulse is generated, its number, phase, and amplitude are tested and selected for inclusion in various bins associated with distributions such as considered in Table 6. Data for many different distributions can be simultaneously recorded in this way. Thus it is possible using software to make efficient use of available data without generating large intermediate data files.

In order to implement this approach in a measurement system, it is necessary that the data be converted to digitized pairs of numbers corresponding to pulse amplitude and time (or phase) that can be accessed sequentially by a computer. Such a system could, of course, also be used to analyze prerecorded data. Although this approach appears feasible using existing analog-to-digital conversion methods and computer technology, no attempts have been made to develop the required hardware.

It should finally be noted that Monte Carlo simulations such as the one that yielded the results shown in Fig. 30 could be used to test the performance of stochastic analyzers. This can be accomplished by using a digital-to-analog converter to produce a sequence of pulses from the output of the computer simulation. The conditional and unconditional distributions measured for the simulated pulses can be compared with the known distributions determined from an analysis made using computer routines such as given in Table 6. The results from the simulation can also be used to provide an indication of the quantities of data needed to obtain statistically meaningful results. The results shown in Fig. 30 correspond to 10^6 cycles of the excitation voltage. It is clear that the quantity of data for $p_1(\phi\bar{8}|Q^+)$ is close to the minimum needed for determination of a statistically significant memory effect.

The possibilities thus appear to exist for constructing efficient computer-based stochastic analyzers that can essentially duplicate and extend the capabilities of the system described here. There are no reasons why such a system could not be designed to accept either analog or digital data directly from measuring devices or indirectly from prerecorded files. The correct performance of the system can be verified using reference data with known stochastic behavior such as generated with a Monte Carlo simulation.
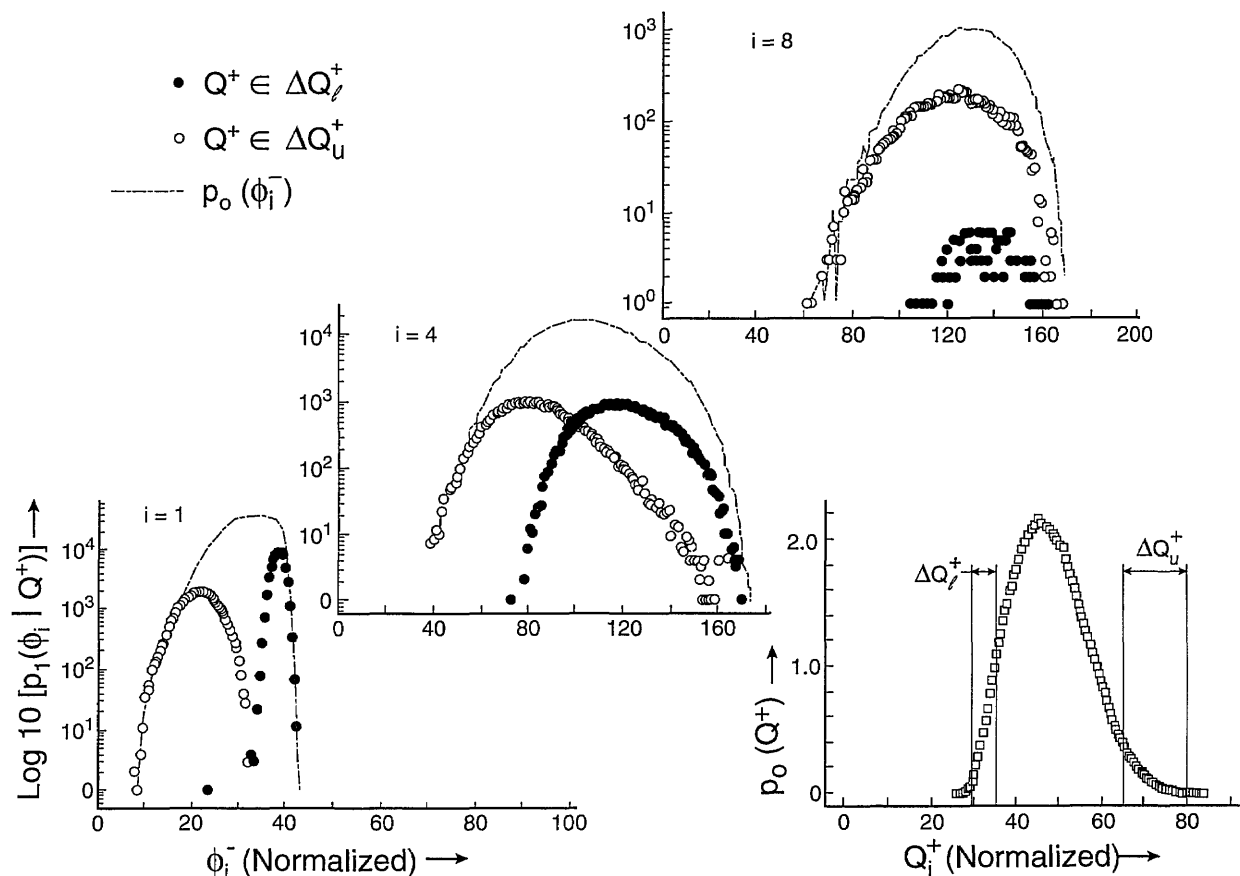
Fig. 30. Examples of results from a computer analysis of PD pulses generated using a Monte Carlo simulation. Shown are the conditional and unconditional distributions determined from a data sorting routine similar to that listed in Table 6.

Acknowledgment

8. References

[1] R. J. Van Brunt and S. V. Kulkarni, Stochastic Properties of Trichel-Pulse Corona: A Non-Markovian Random Point Process, Phys. Rev. A 42, 4908–4932 (1990).

[2] R. J. Van Brunt, M. Misakian, S. V. Kulkarni, and V. K. Lakdawala, Influence of a Dielectric Barrier on the Stochastic Behavior of Trichel-Pulse Corona, IEEE Trans. Elec. Insul. 26, 405–415 (1991).

[3] R. J. Van Brunt and E. W. Cernyar, Influence of Memory Propagation on Phase-Resolved Stochastic Behavior of AC-Generated Partial Discharges, Appl. Phys. Lett. 58, 2628–2630 (1991).

[4] R. J. Van Brunt, Stochastic Properties of Partial-Discharge Phenomena, IEEE Trans. Elec. Insul. 26, 902–948 (1991).

[5] R. Bartnikas, A Commentary on Partial Discharge Measurement and Detection, IEEE Trans. Elec. Insul. 22, 629–653 (1987).

[6] G. Mole and F. C. Robinson, A Versatile Corona Detector, 1962 Annual Report—Conference on Electrical Insulation, Nat. Aca. Sci., Publ. 1080, 54–56 (1962).

[7] Report of CIGRE Working Group 21.03, Recognition of Discharges, Electra 11, 61–98 (1969).

[8] T. Okamoto and T. Tanaka, Prediction of Treeing Breakdown from Pulse Height of Partial Discharge on Voltage-Phase Angle, Jap. J. Appl. Phys. 24, 156–160 (1985).

[9] H. Huzumi, T. Okamoto, and H. Fukagawa, Simultaneous Measurement of Microscopic Image and Discharge Pulses at the Moment of Electrical Tree Initiation, Jap. J. Appl. Phys. 27, 572–576 (1988).

[10] T. Tanaka, Internal Partial Discharge and Material Degradation, IEEE Trans. Elec. Insul. 21, 899–905 (1986).

[11] M. Gomez-Garcia, R. Bartnikas, and M. R. Wertheimer, Modification of XLPE Exposed to Partial Discharges at Elevated Temperature, IEEE Trans. Elec. Insul. 25, 688–692 (1990).

[12] E. Gulski and F. H. Kreuger, Computer-aided Analysis of Discharge Patterns, J. Phys. D: Appl. Phys. 23, 1569–1575 (1990); Computer-aided Recognition of Discharge Sources, IEEE Trans. Elec. Insul. 27, 82–92 (1992).

[13] E. Gulski, P. H. F. Morshuis, and F. H. Kreuger, Atomized Recognition of Partial Discharges in Cavities, Jap. J. Appl. Phys. 29, 1329–1335 (1990).

[14] H. Hikita, Y. Yamada, A. Nakamura, T. Mizutani, A. Oohasi, and M. Ieda, Measurement of Partial Discharge by Computer and Analysis of Partial Discharge by the Monte Carlo Method, IEEE Trans. Elec. Insul. 25, 453–468 (1990).

[15] J. M. Braun, S. Rizzetto, N. Fujimoto, and G. L. Ford, Modulation of Partial Discharge Activity in GIS Insulators by X-ray Irradiation, IEEE Trans. Elec. Insul. 26, 460–468 (1991).

[16] B. Fruth and L. Niemeyer, The Importance of Statistical Characteristics of Partial Discharge Data, IEEE Trans. Elec. Insul. 27, 60–69 (1992).

[17] J. Austin and R. E. James, On-line Digital Computer System for Measurement of Partial Discharges in Insulation Structures, IEEE Trans. Elec. Insul. 11, 129–139 (1976).

[18] H. Borsi and M. Hartje, A New System for Computer Aided Automation of Different Commercially Available Partial Discharge (PD) Detectors, Proc. 6th Int. Symp. on High Voltage Engineering, New Orleans, paper 22.18 (1989).

[19] H. N. Geetha, M. B. Srinivas, and T. S. Ramu, Pulse-Count Distribution—a Possible Diagnostic Tool for Assessing the Level of Degradation of Rotating Machine Insulation, IEEE Trans. Elec. Insul. 25, 747–756 (1990).

[20] T. Okamoto and T. Tanaka, Novel Partial Discharge Measurement Computer-aided Measurement Systems, IEEE Trans. Elec. Insul. 21, 1015–1016 (1986).

[21] U. Bammert and M. Beyer, Partial Discharges Measured with an Automated System in Epoxy Resin and Polyethylene, IEEE Trans. Elec. Insul. 23, 215–225 (1988).

[22] R. Schifani, A Novel Histogram for Partial Discharge Signals in HV Insulating Systems, IEEE Trans. Elec. Insul. 21, 89–99 (1986).

[23] J. P. Steiner, Digital Measurement of Partial Discharge, Ph. D. Thesis, Purdue University, May 1988.

[24] R. J. Van Brunt and S. V. Kulkarni, Method for Measuring the Stochastic Properties of Corona and Partial Discharge Pulses, Rev. Sci. Instrum. 60, 3012–3023 (1989).

[25] R. J. Van Brunt, K. L. Stricklett, J. P. Steiner, and S. V. Kulkarni, Recent Advances in Partial Discharge Measurement Capabilities at the NIST, IEEE Trans. Elec. Insul. 27, 114–129 (1992).

[26] D. L. Snyder, Random Point Processes, Wiley, New York, New York (1975), pp. 434–455.

[27] R. J. Van Brunt and D. Leep, Characterization of Point-Plane Corona Pulses in SF_6, J. Appl. Phys. 52, 6588–6600 (1981).

[28] J. L. Mesa and A. P. Sage, An Introduction to Probability and Stochastic Processes, Prentice-Hall, Englewood Cliffs, New Jersey (1973) p. 60.

[29] R. J. Van Brunt and M. Misakian, Mechanisms for Inception of dc and 60-Hz ac Corona in SF_6, IEEE Trans. Elec. Insul. EI-17, 106–120 (1982).

[30] W. E. Anderson and R. S. Davis, Measurements on Insulating Materials at Cryogenic Temperatures, National Bureau of Standards Interagency Report, NBSIR 79-1950 (1980).

[31] P. Horowitz and W. Hill, The Art of Electronics, Cambridge University Press, London (1980) pp. 134–135.

[32] R. J. Van Brunt, E. W. Cernyar, P. von Glahn, and T. Las, Variations in the Stochastic Behavior of Partial-Discharge Pulses with Point-to-Dielectric Gap Spacing, Conf. Rec. 1992 IEEE Int. Symp. on Elec. Insul., Baltimore, 349–353 (1992).

[33] R. J. Van Brunt and E. W. Cernyar, Stochastic Analysis of AC-Generated Partial Discharge Pulses from a Monte-Carlo Simulation, 1992 Annual Report—Conference on Electrical Insulation and Dielectric Phenomena, IEEE, NY, 427–434 (1992).

[34] H. T. Harnen, The Characteristic Decay with Time of Surface Charges in Dielectrics, J. Electrostatics 1, 173–185 (1975).

[35] E. A. Baum, T. J. Lewis, and R. Toomer, The Lateral Spreading of Charge on Thin Films of Polyethylene Terephtalate, J. Phys. D: Appl. Phys. 11, 963–977 (1978).

[36] I. Somerville and P. Vidand, Surface Spreading of Charge Due to Ohmic Conduction, Proc. Roy. Soc. London, Sec. A 399, 277–293 (1985).

[37] D. K. Das-Gupta, Decay of Electrical Charges on Organic Synthetic Polymer Surfaces, IEEE Trans. Elec. Insul. 25, 503–508 (1990).

[38] W. L. Lama and C. F. Gallo, Systematic Study of the Electrical Characteristics of the "Trichel" Current Pulses from Negative Needle-to-Plane Coronas, J. Appl. Phys. 45, 103–113 (1974).

[39] D. A. Bosan and T. V. Jovanovic, Memory Curves used in Establishing the Time Variation of Metastable Concentrations in the Afterglow Period in Nitrogen and Neon, J. Phys. D: Appl. Phys. 25, 436–441 (1992).

[40] A. K. Jonscher and E. F. Owede, Time and Frequency-resolved Surface Currents on Insulators, IEEE Trans. Elec. Insul. 25, 1077–1084 (1990).

[41] T. V. Blalock, A. L. Wintenberg, and M. O. Pace, Low-Noise, Wide-Band Amplification System for Acquiring Prebreakdown Current Pulses in Liquid Dielectrics, IEEE Trans. Elec. Insul. 24, 641–647 (1989).

[42] L. R. Rabiner, J. H. McClellan, and T. W. Parks, FIR Digital Filter Design Techniques Using Weighted Chebyshev Approximations, Proc. IEEE 63, 595–610 (1975).

[43] V. Köpf and K. Feser, Possibilities to Improve the Sensitivity of PD-Measurements by Using Digital Filters, Proc. Int. Symp. on Digital Techniques in High-Voltage Measurements, Toronto, Canada, 2-27-2-31 (1991).

About the authors: R. J. Van Brunt is a physicist in the Electricity Division of NIST and E. W. Cernyar is a co-op student at NIST from the Georgia Institute of Technology. The National Institute of Standards and Technology is an agency of the Technology Administration, U.S. Department of Commerce.

High Power CW Wattmeter Calibration at NIST

Gregorio Rebuldela and
Jeffrey A. Jargon

National Institute of Standards
and Technology,
Boulder, CO 80303

The National Institute of Standards and Technology has established a measurement capability to support high power systems and devices. The automated wattmeter calibration system operates at power levels of 1 to 1000 W for frequencies from 1 to 30 MHz and 1 to 500 W from 30 to 400 MHz. A cascaded coupler technique is used to extend power measurements to high levels which are traceable to a 10 mW standard thermistor mount. This technique uses an arrangement of nominal 10, 20, 30, 40, and 50 dB couplers with sidearm power meters. The initial step transfers the calibration of the 10 mW standard to the 10 dB coupler/power meter. The standard is then replaced with a wattmeter to be calibrated. RF power is increased 10 dB and the calibration is transferred to the adjacent 20 dB coupler/power meter. This sequence is repeated with the remaining coupler/power meters until the wattmeter is calibrated at the desired power levels and frequencies. Power ratios calculated from simultaneous power measurements made at each transfer are used to calculate the incident power at the wattmeter. Due to nonideal components, corrections are made for nonlinearities, mismatch, and other errors. Two types of wattmeters have been evaluated at selected frequencies and power levels. Total uncertainties are based on the random and systematic components.

Key words: automated; calibration; cascaded; continuous wave; coupler; high power; measurement; transfer; uncertainty; wattmeter.

Accepted: August 25, 1992

1. Introduction

There has been a recent interest in and demand for improved high power calibrations to support new and more accurate high power systems and devices being developed by industry. NIST has established a measurement capability to provide a traceability for continuous wave (cw) high power measurements. This paper describes the system, measurement scheme, calibration results and uncertainty analysis of the calibrations performed on different types of high power wattmeters.

2. System Description

A diagram of the system is shown in Fig. 1. The rf source provides a stable rf signal at power levels of 1 to 1000 W for frequencies from 10 to 30 MHz, and 1 to 500 W from 30 to 400 MHz [1]. The frequency and output power are controlled by software. A closed-loop feedback arrangement maintains the output power within ±0.005 dB. The rf power path is switched to one of three test output ports depending on the frequency.

Since the source delivers a minimum of 1 W and the initial two calibration stages are made at 10 and 100 mW, an in-line attenuator is inserted between the source and the 10 dB coupler to reduce the power to the required levels. This latching attenuator has a range of 1 to 31 dB in 1 db steps and is controlled manually.
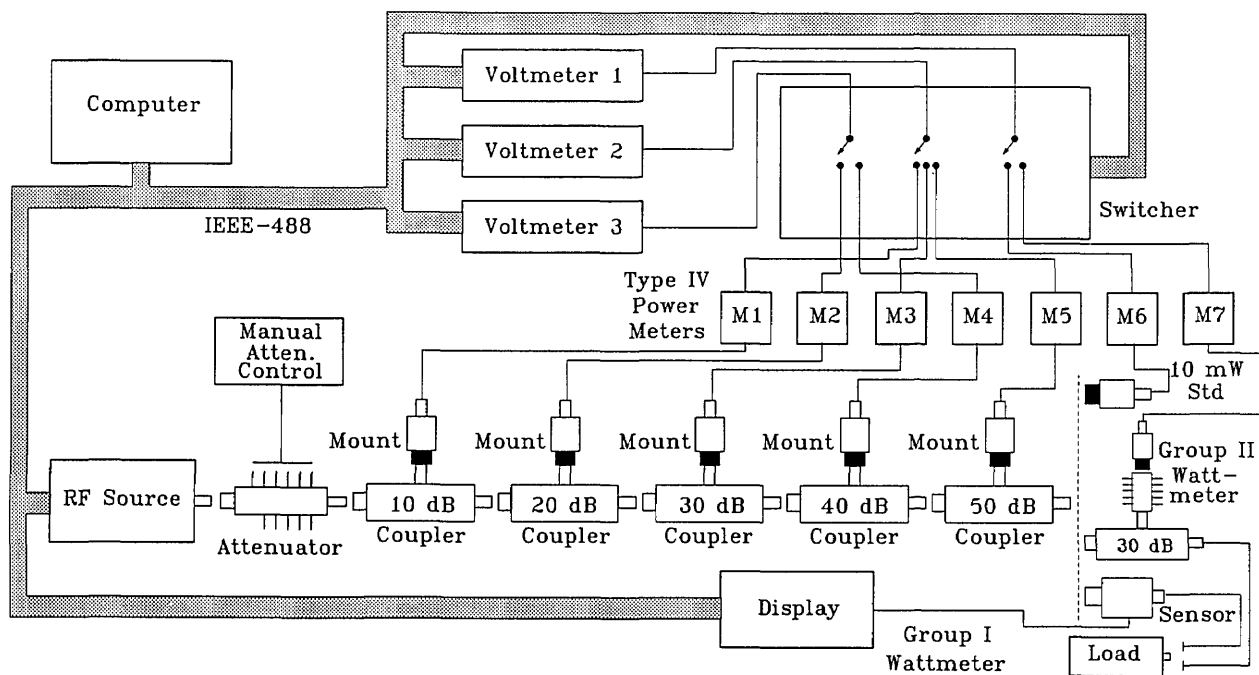
Fig. 1. Block diagram of NIST high power cw wattmeter calibration system.

The cascaded coupler arrangement is composed of nominal 10, 20, 30, 40, and 50 dB directional couplers with sidearm power meters connected to digital voltmeters. Five coupler/power meters are required to transfer powers from 10 mW to 1000 W in 10 dB steps. Each sidearm power meter, composed of a thermistor mount in conjuction with a NIST Type IV bridge, is connected to a digital voltmeter to measure rf powers within the bandwidth of the thermistor mount. The switcher connects each voltmeter to one of seven power meters depending on the stage of the calibration. A calibrated thermistor mount serves as the 10 mW reference for extending measurements to higher levels.

Measurements are performed on two types of wattmeters. Group I includes three similar commercial units that measure rf power directly using diode power sensors. These sensors, used in conjunction with a power meter as a display, are microprocessor-based, each carrying its own wideband calibration constants in a self-contained nonvolatile memory. Since the calibration data are stored in the sensor, any sensor may be used with any power meter. Group II consists of two 30 dB couplers each with a manually switched, 0–31 dB step attenuator and thermistor mount on the sidearm. The attenuation is determined by the rf power incident on the coupler.

The computer controls the rf source, the digital voltmeters, and the switcher, and handles the data acquisition and processing through an IEEE-488 bus.

3. Measurement Methods

3.1 Cascaded Coupler Technique

At NIST, the measurement of rf power below 1 GHz has been limited to 10 mW with thermistor mounts at uncertainties of $\pm 0.5\%$ or better. A cascaded coupler technique, developed by K. E. Bramall [2], extends measurements to higher levels which are traceable to a 10 mW standard. Each stage is summarized below.

Stage 1 The 10 mW standard is connected to the cascaded coupler arrangement as shown in Fig. 2(a). Since the source delivers a minimum of 1 W, an in-line attenuator is inserted between the source and the input of the 10 dB coupler/thermistor mount combination to prevent any damage to the reference standard. With the attenuator set to 20 dB, approximately 10 mW are applied to the reference standard. Simultaneous readings are taken on M_1 and M_S. The power on M_1 is nominally 1 mW and due to the insertion loss of the coupler chain, M_S will indicate slightly less than 10 mW.
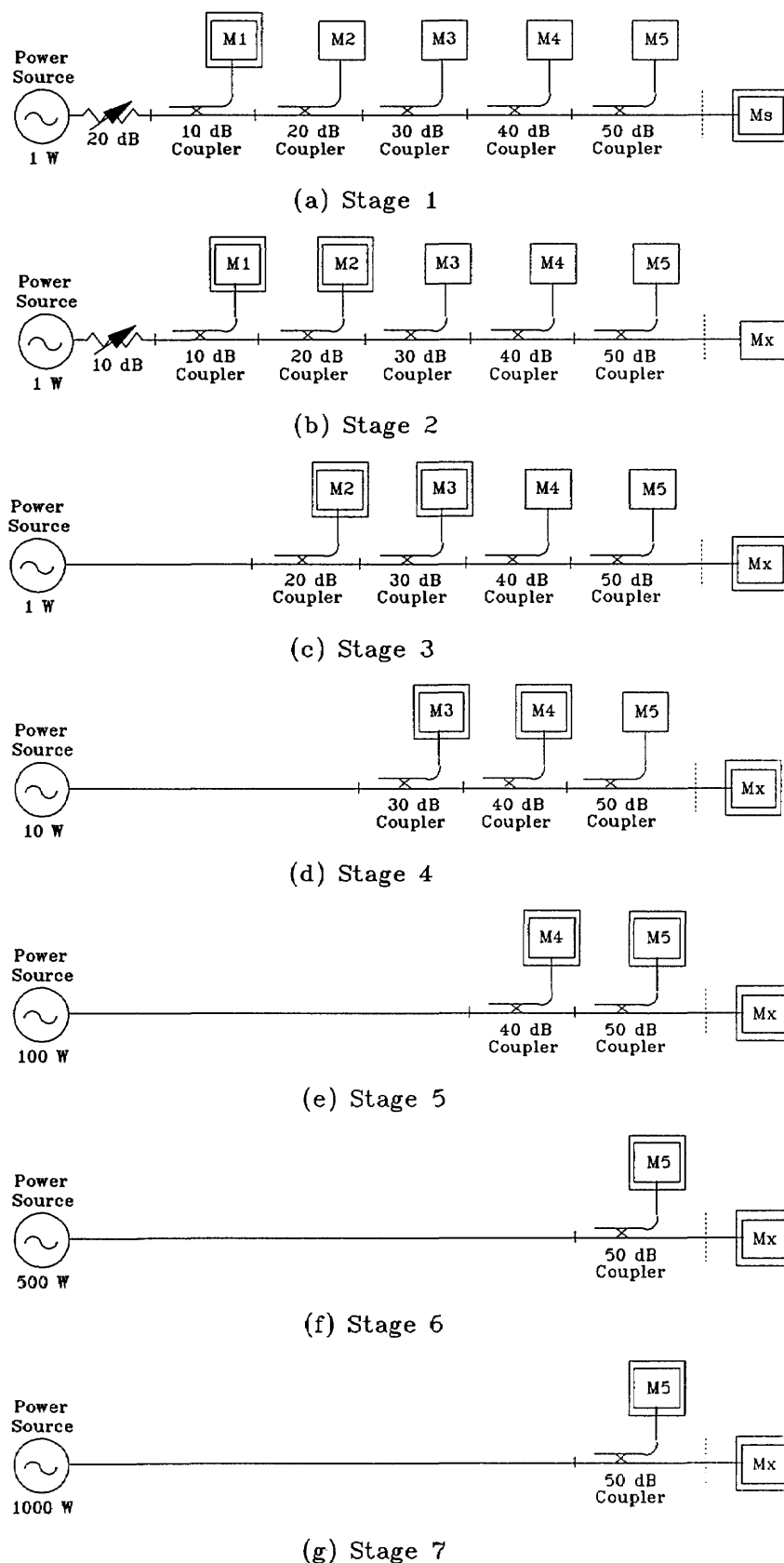
Fig. 2. Cascaded coupler arrangements for power transfer from 10 mW to 1000 W.

Stage 2 The 10 mW standard is replaced with the wattmeter, M_X, to be calibrated as shown in Fig. 2(b). If the wattmeter is from Group II, its attenuator is set to 0 dB, and the rf power is increased 10 dB to 100 mW, by setting the in-line attenuator to 10 dB. Simultaneous readings result in a nominal 10 mW on M_1 and 1 mW on M_2. The main-arm output power, P_L, incident on the wattmeter is approximately 100 mW and is given by

$$P_L = \frac{P_1'}{P_1} \frac{P_S}{K_B},$$ (1)

where P_1 is the reading of the sidearm power meter of the 10 dB coupler/thermistor mount, M_1, when the calibration was transferred from the 10 mW standard, P_1' is the reading of M_1 when it was used to transfer the calibration to M_2, and P_S is the reading of M_S from the first stage. The calibration factor, K_B, of the 10 mW standard is defined as the ratio of the substituted dc power in the thermistor mount to the cw rf power incident upon it.

Equation (1) is true only if the impedances of the power standard and the wattmeter are equal. Since they are not, the expression is modified to include the effects of mismatch [3].

$$P_L = \frac{P_1'}{P_1} \frac{P_S}{K_B} \frac{|1 - \Gamma_{GE}\Gamma_S|^2}{|1 - \Gamma_{GE}\Gamma_X|^2},$$ (2)

where Γ_S and Γ_X are the reflection coefficients of the standard and wattmeter, respectively. The factor, Γ_{GE}, is defined by Engen [4] as the equivalent generator reflection coefficient, and is given in terms of the coupler chain's scattering parameters,

$$\Gamma_{GE} = S_{22} - \frac{S_{21}S_{32}}{S_{31}},$$ (3)

where the input of the 10 dB coupler is port 1, the output of the 50 dB coupler is port 2, and the sidearm of the 10 dB coupler is port 3.

Stage 3 The in-line attenuator and the 10 dB coupler/thermistor is removed, as shown in Fig. 2(c). The calibration of the 20 dB coupler/thermistor is not affected since a directional coupler has the property that the power split between the main and sidearm is independent of the source characteristics [5].

The source is set to 1 W, a 10 dB increase from the previous stage, and simultaneous readings are taken on M_2, M_3, and M_X. The reading on M_2, referred to as P_2', is about 10 mW, while P_3, the reading on M_3, is approximately 1 mW. The main-arm output power, P_L, is about 1 W and is given by

$$P_L = \frac{P_1'}{P_1} \frac{P_2'}{P_2} \frac{P_S}{K_B} MM,$$ (4)

where

$$MM = \frac{|1 - \Gamma_{GE}\Gamma_S|^2}{|1 - \Gamma_{GE}\Gamma_X|^2}.$$ (5)

At this level, the calibration factor, K_{f1}, of the Group I wattmeter is defined as

$$K_{f1} = \frac{P_X}{P_L},$$ (6)

where P_X is the reading on the wattmeter's display. The calibration factor, K_{f2}, of the Group II wattmeter is defined as

$$K_{f2} = \frac{P_L}{P_X},$$ (7)

where P_X is the substituted dc power of the wattmeter's thermistor mount. In both cases, P_L is the rf power incident on the wattmeters and is calculated at each rf power level.

Stage 4 The 20 dB coupler/thermistor is removed as shown in Fig. 2(d), and the source power is increased 10 dB, to about 10 W. Simultaneous readings are taken on M_3, M_4, and M_X. The reading on M_3, called P_3', is about 10 mW and P_4, the reading on M_4, is about 1 mW. The wattmeter is calibrated at this level using either Eq. (6) or (7), depending on the wattmeter. The main-arm output power, P_L, is nominally 10 W and is given by

$$P_L = \frac{P_1'}{P_1} \frac{P_2'}{P_2} \frac{P_3'}{P_3} \frac{P_S}{K_B} MM.$$ (8)

Stage 5 The 30 dB coupler/thermistor is removed as shown in Fig. 2(e). If the wattmeter is from Group II, its attenuator is set to 10 dB to prevent damage to its thermistor mount from subsequent increases of power. The source power is increased 10 dB, to about 100 W and simultaneous readings are taken on M_4, M_5, and M_X. The reading on M_4, called P_4', is about 10 mW, and P_5 is about 1 mW. The main-arm output power, P_L, is nominally 100 W and is given by

$$P_L = \frac{P_1'}{P_1} \frac{P_2'}{P_2} \frac{P_3'}{P_3} \frac{P_4'}{P_4} \frac{P_S}{K_B} MM.$$ (9)

Stage 6 The 40 dB coupler/thermistor is removed as shown in Fig. 2(f). If it is desired to calibrate the wattmeter between 100 and 1000 W, such as 500 W, the rf power is increased by 7 dB. If the wattmeter is from Group II, its attenuator is set to

17 dB before applying rf power. Simultaneous readings are taken on M_5, called P_5', and M_X. The main-arm output power is given by

$$P_L = \frac{P_1'}{P_1} \frac{P_2'}{P_2} \frac{P_3'}{P_3} \frac{P_4'}{P_4} \frac{P_5'}{P_5} \frac{P_S}{K_B} MM. \qquad (10)$$

Stage 7 The source power is increased by 3 dB, to 1000 W, using the same configuration as the previous stage. See Fig. 2(g). If the wattmeter is from Group II, its attenuator is set to 20 dB, and simultaneous readings are taken on M_5, called P_5'', and M_X. The main-arm output power is given by

$$P_L = \frac{P_1'}{P_1} \frac{P_2'}{P_2} \frac{P_3'}{P_3} \frac{P_4'}{P_4} \frac{P_5''}{P_5} \frac{P_S}{K_B} MM. \qquad (11)$$

The wattmeter is now calibrated at 1, 10, 100, 500, and 1000 W at the desired frequency.

3.2 Modifications to the Cascaded Coupler Technique

Since the high power source is limited to 500 W at 30–400 MHz, wattmeters from Group I were calibrated at 1, 10, 100, 300 and 500 W in this frequency band. This still requires seven stages in the calibration although stages 6 and 7 are modified for lower powers. Wattmeters from Group II are rated at 200 W, so they were calibrated at 1, 10, 100 and 200 W which required six stages. When the measurements were taken, a 10 dB coupler was not available, so a 14 dB coupler was used instead. The only modification necessary was to set the in-line attenuator to 6 dB rather than 10 dB at the second stage, so enough power would be applied to the thermistors.

3.3 Power Measurements

The NIST Type IV power meter does not directly read dc power in watts and must be connected to an external dc voltmeter.The substituted dc power, P_{dc}, is calculated from measured voltages and is given by

$$P_{dc} = \frac{V_{off}^2 - V_{on}^2}{R_0}, \qquad (12)$$

where V_{off} is the output voltage with no rf power applied, V_{on} is the output voltage with rf power applied, and R_0 is the operating resistance of the thermistor mount. Figure 3 shows the measurement sequence for a power calculation [6]. An initial V_{off} is taken; rf power is then applied and V_{on} is measured; rf power is removed and a final V_{off} is taken.

The initial and final dc measurements are used with the V_{on} measurement to calculate the power and correct for any mount drift, which is assumed to be linear. The calculated value of V_{off} in Eq. (12) is given by

$$V_{off} = V_{off,i} + \frac{t_2 - t_1}{t_3 - t_1} (V_{off,f} - V_{off,i}), \qquad (13)$$

where $V_{off,i}$ is the voltage reading taken before rf is applied at time t_1, $V_{off,f}$ is the voltage taken after rf is removed at time t_3, and t_2 is the time at which V_{on} is taken.
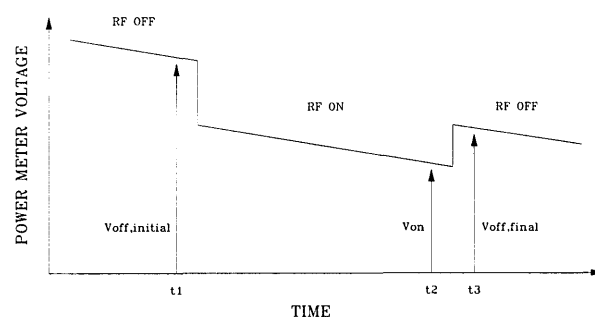
Fig. 3. Sequence for measuring power meter dc voltages.

4. Measurement Results

Measurements were made on both groups of wattmeters at several frequencies and power levels. Group I wattmeters were calibrated at 1, 10, 100, 500 and 1000 W at frequencies from 2 to 30 MHz and at 1, 10, 100, 300 and 500 W at frequencies from 30 to 400 MHz. Group II wattmeters were calibrated at 1, 10, 100 and 200 W at the same frequencies.

The calibration factors for a Group I wattmeter are near unity at all power levels since it measures power directly with a diode detector. A Group I wattmeter has one sensor, denoted Sensor 1, that measures powers at frequencies between 1.8 and 32 MHz and another, Sensor 2, that measures power at frequencies between 25 and 1000 MHz. Sensor 1 was used at frequencies between 2 and 30 MHz, and Sensor 2 was used at frequencies between 35 and 400 MHz. Table 1 lists calibration factors at selected frequencies for three wattmeters from Group I. The calibration factors differ among wattmeters, and the calibration factor at each frequency increases with power, partly due to nonlinearity in the diode detector.

The calibration factors for a Group II wattmeter range from 1,000 to 20,000 due to the 30 dB directional coupler and the attenuator's setting which is dependent on the power level; 0 dB at 1 and 10 W, 10 dB at 100 W, and 13 dB at 200 W. One wattmeter has a frequency range from 2 to 100 MHz and the other has a range from 100 to 400 MHz. Tables 2 and 3 list the measured calibration factors of the two wattmeters.

Table 1. Calibration factors of Group I wattmeters

Freq. (MHz)	Power level (W)	Wattmeter A cal. factor	Wattmeter B cal. factor	Wattmeter C cal. factor
2	1	0.9989	0.9929	0.9927
	10	1.0067	1.0062	1.0022
	100	1.0195	1.0196	1.0134
	500	1.0268	1.0285	1.0218
	1000	1.0297	1.0321	1.0244
15	1	1.0014	0.9895	0.9972
	10	1.0087	1.0026	1.0061
	100	1.0198	1.0133	1.0153
	500	1.0240	1.0190	1.0207
	1000	1.0248	1.0202	1.0216
30	1	1.0041	0.9989	0.9950
	10	1.0108	1.0121	1.0022
	100	1.0207	1.0194	1.0118
	500	1.0252	1.0277	1.0167
	1000	1.0269	1.0293	1.0181
40	1	0.9961	0.9955	0.9903
	10	1.0052	1.0047	0.9972
	100	1.0110	1.0142	1.0097
	300	1.0116	1.0161	1.0116
	500	1.0178	1.0220	1.0177
70	1	1.0002	1.0005	0.9857
	10	1.0082	1.0083	0.9965
	100	1.0129	1.0192	1.0094
	300	1.0149	1.0256	1.0153
	500	1.0209	1.0283	1.0185
100	1	1.0059	1.0061	0.9943
	10	1.0126	1.0153	1.0055
	100	1.0180	1.0253	1.0176
	300	1.0235	1.0313	1.0214
	500	1.0271	1.0339	1.0253
125	1	0.9988	0.9960	0.9782
	10	1.0050	1.0068	0.9915
	100	1.0180	1.0238	1.0068
	300	1.0200	1.0300	1.0127
	500	1.0236	1.0318	1.0158
250	1	1.0036	0.9984	0.9758
	10	1.0102	1.0099	0.9905
	100	1.0219	1.0258	1.0045
	300	1.0241	1.0325	1.0112
	500	1.0292	1.0351	1.0125
400	1	0.9939	0.9939	0.9694
	10	1.0025	1.0014	0.9826
	100	1.0135	1.0173	0.9971
	300	1.0169	1.0247	1.0045
	500	1.0230	1.0276	1.0078

Table 2. Calibration factors of Group II-A wattmeter

Freq. (MHz)	Power level (W)	Wattmeter A cal. factor
2	1	1105.9
	10	1102.9
	100	11004.2
	200	21747.7
10	1	1139.3
	10	1137.0
	100	11359.1
	200	22506.0
20	1	1167.7
	10	1165.0
	100	11642.0
	200	23119.1
30	1	1189.2
	10	1186.5
	100	11816.8
	200	23586.1
40	1	1224.7
	10	1224.0
	100	12179.5
	200	24047.3
60	1	1272.2
	10	1272.1
	100	12654.4
	200	25036.1
80	1	1320.8
	10	1320.7
	100	13163.1
	200	26174.3
100	1	1378.3
	10	1377.4
	100	13806.0
	200	27561.8

Table 3. Calibration factors of Group II-B wattmeter

Freq. (MHz)	Power level (W)	Wattmeter B cal. factor
125	1	1249.6
	10	1247.3
	100	12659.0
	200	25054.4
200	1	1127.0
	10	1122.9
	100	11694.0
	200	23150.8
300	1	1166.4
	10	1162.4
	100	12606.7
	200	24952.1
400	1	1558.4
	10	1553.9
	100	16629.3
	200	33003.9

5. Uncertainty Analysis

5.1 Systematic Uncertainty

The factors contributing to the total systematic uncertainty are:

a. Uncertainty in the dc voltmeter measurements.
b. Uncertainty in the Type IV power meters.
c. The dual-element substitution errors associated with the coaxial thermistor mounts.
d. Uncertainty in the 10 mW standard mount calibration factor.
e. Mismatch uncertainty due to the reflection coefficient of the 10 mW standard mount, the reflection coefficient of the wattmeter/high power load combination, and the equivalent generator reflection coefficient.
f. Nonlinearities in the cascaded couplers.
g. Uncertainty in the high power source.

5.1.1 Voltmeter Uncertainty

The uncertainty in the individual voltmeter readings can be determined by taking the total differential of the power expression, Eq. (12), which gives

$$dP = \frac{2}{R_0} \left(V_{off} \, dV_{off} - V_{on} \, dV_{on} \right). \tag{14}$$

The total differential of power, Eq. (14), can be determined by taking the differential of V_{off}, Eq. (13), which gives

$$dV_{off} = (1 - T) \, dV_{off, i} + T \, dV_{off, f}, \tag{15}$$

where

$$T = \frac{t_2 - t_1}{t_3 - t_1}. \tag{16}$$

The uncertainties, $dV_{off,i}$, $dV_{off,f}$, and dV_{on}, in the measured values of $V_{off,i}$, $V_{off,f}$ and V_{on}, are based on the voltmeter manufacturer's specifications.

Figure 4 shows the uncertainty in the power measurement as a function of power level, assuming the coupler sidearm powers, P_1 through P_5 and P_1' through P_5', are ratioed as in the Bramall measurements. Figure 5 shows the uncertainty when a power is not ratioed as in the case of P_5.

The power measurements, P_1' through P_5', are approximately 10 mW, which result in uncertainties of 0.01%. The power measurements, P_2 through P_5, are approximately 1 mW, which result in uncertainties of 0.07%. The measurement of P_1 is about 0.4 mW due to the 14 dB coupler and has an uncertainty of 0.17%.

5.1.2 Type IV Power Meter Uncertainty

The four possible sources of uncertainties internal to the Type IV power meter are the reference resistors, the operational amplifier open-loop gain, input offset voltage, and input bias current. Larsen has shown that the uncertainties due to the Type IV power meters are negligible compared to those of the voltmeters [7].

5.1.3 Dual-Element Uncertainty

The thermistors used in the system are dual-element bolometers. They are nonlinear with power due to the rf-dc substitution error that occurs because the two elements are not identical [8]. The NIST calibration of the effective efficiency is done at 10 mW; therefore, this error is of concern when measurements are made below this power. Direct measurements were performed on similar thermistor mounts [6] resulting in a nonlinearity of about 0.04% at the 1 mW level.

5.1.4 Uncertainty in the Standard Mount Calibration Factor

The uncertainty of the NIST thermistor mount calibration factor, K_B, is approximately $\pm 0.5\%$ in the worst case. The 10 mW standard is recalibrated periodically.

5.1.5 Mismatch Uncertainty

Since the impedances of the standard power meter and the high power load are not equal, mismatch is introduced when the power meter is replaced by the load. The mismatch term, discussed earlier, is given by

$$MM = \frac{|1 - \Gamma_{GE}\Gamma_S|^2}{|1 - \Gamma_{GE}\Gamma_X|^2}. \tag{17}$$

The uncertainty of the mismatch term requires the knowledge of the uncertainties in measuring Γ_X, Γ_S, and the couplers' scattering coefficients. These uncertainties are given in Table 4. The uncertainty of Γ_{GE}, which is almost entirely due to the uncertainty of S_2, is ± 0.0034 and is combined with those of the 10 mW standard and wattmeter/load combination to calculate the total mismatch uncertainty. Two different methods were used to analyze the uncertainty.

First, a simulation program was written to calculate the mismatch uncertainty using random values of magnitude and phase, within their respective limits, for the reflection coefficients along with their respective uncertainties. Several hundred trials were performed, resulting in a maximum mismatch uncertainty of $\pm 0.19\%$.

Second, the mismatch uncertainty was calculated by combining the terms in Eq. (17) in the worst phase with the uncertainties included. The result

was a maximum mismatch uncertainty of ±0.2%. The latter method was arbitrarily chosen and its derivation is explained in the Appendix.

5.1.6 Nonlinearity of Couplers The directional couplers were chosen with power ratings greater than the actual requirements to minimize the power sensitivity of the couplers. Each coupler is rated at least one and one-half times its maximum applied power.

Tests for power nonlinearities were performed on selected couplers at higher powers, and an estimate for the entire coupler chain is approximately ±0.30%.

5.1.7 Uncertainty in the High Power Source There are several uncertainties due to the radio frequency source, most of which are negligible.

a. Harmonics are at least 46 dB below the fundamental signal at the output port, thus having negligible effects.
b. Spurious signals are also negligible since they are approximately −60 dBc.
c. The frequency uncertainty is approximately ±0.001% due to the internal free-air crystal oscillator of the rf source.
d. The rf source amplitude stability is specified by the manufacturer to be ±0.12%.
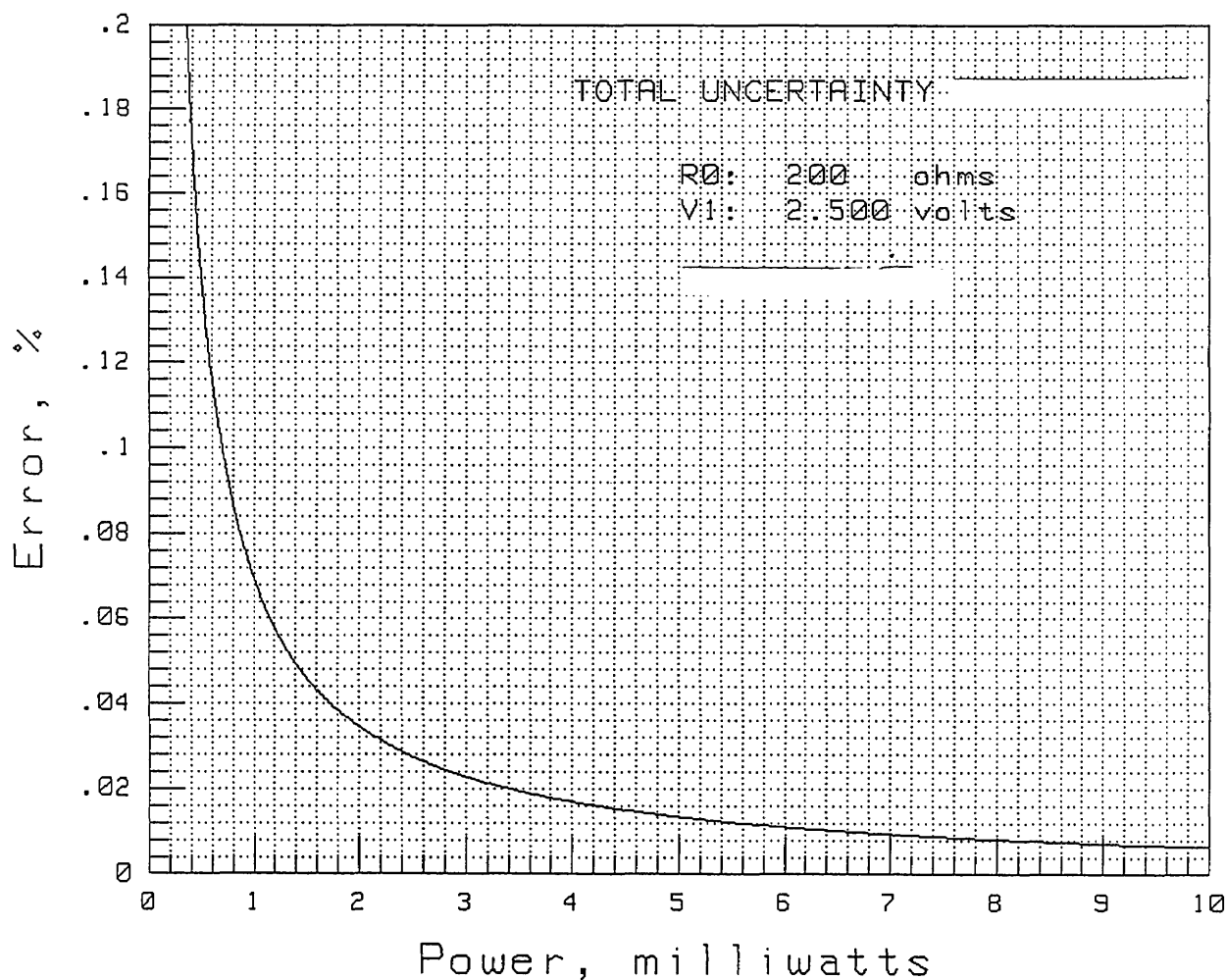
Fig. 4. Power measurement uncertainty due to DVM when ratios are taken.
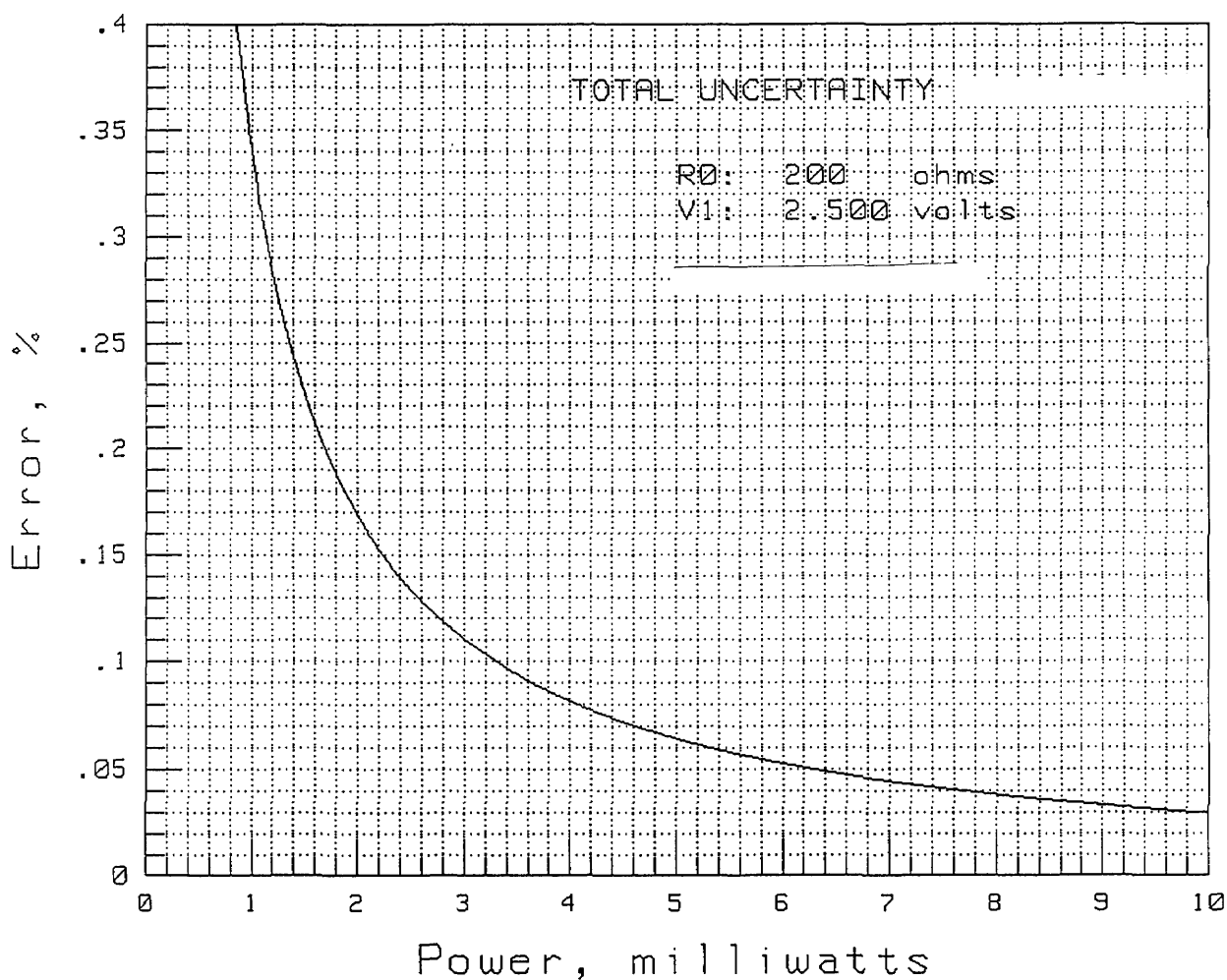
Fig. 5. Power measurement uncertainty due to DVM when ratios are not taken.

Table 4. Reflection coefficients and uncertainties of mismatch components

Source	Max. value ± uncertainty
Reflection coefficient of 10 mW std.	0.02 ± 0.0030
Reflection coefficient of wattmeter/load combination	0.04 ± 0.0034
Reflection coefficient of equivalent generator	0.12 ± 0.0034
S_{22} of coupler chain	0.12 ± 0.0034
S_{21} of coupler chain	1.92 ± 0.0050 dB
S_{32} of coupler chain	60.95 ± 0.20 dB
S_{31} of coupler chain	14.49 ± 0.0095 dB

5.1.8 Overall Systematic Uncertainty A summary of all the systematic uncertainty components and the total as calculated by the root-sum-square method are shown in Table 5. The overall systematic uncertainty is ±0.67%.

Table 5. Systematic uncertainty components

Uncertainty source	Contribution (%)
dc voltage measurements	
Measurement of P_1	±0.17
Measurement of P_2	±0.07
Measurement of P_3	±0.07
Measurement of P_4	±0.07
Measurement of P_5	±0.07
Measurement of P_1'	±0.01
Measurement of P_2'	±0.01
Measurement of P_3'	±0.01
Measurement of P_4'	±0.01
Measurement of P_5'	±0.01
Measurement of P_s	±0.03
Dual element of bolometer mounts	
Measurement of P_1	±0.05
Measurement of P_2	±0.04
Measurement of P_3	±0.04
Measurement of P_4	±0.04
Measurement of P_5	±0.04
Power standard calibration factor	±0.50
Mismatch due to reflection coefficients	±0.20
Nonlinearity of cascaded couplers	±0.30
High power source	±0.12
Total (RSS)	±0.67

5.2 Random Uncertainty

Each of the wattmeters was calibrated five times to determine the repeatability of the measurements. Tests were made at various times of the day over several days to cover as many random factors as possible, including variations of environmental conditions and quality of the connections by the operator. The sample standard deviations were calculated for each meter at all frequencies and power levels. Table 6 lists the standard deviations of the three Group I wattmeters; Table 7 lists the standard deviations of the Group II-A wattmeter (2–30 MHz); and Table 8 lists the standard deviations of the Group II-B wattmeter (30–400 MHz).

Wattmeter C of Group I was calibrated five more times over a 6 month period to determine the long-term stability of the calibration factors. Figures 6, 7, and 8 show the ten measurements at each power level with their averages at 2, 100, and 400 MHz, respectively. Sample standard deviations of the ten trials ranged from 0.07% to 0.66%.

5.3 Total Uncertainty

The total uncertainty, U_T, may be calculated by combining the standard deviation, S, determined from N repeated measurements, with the overall systematic uncertainty, Δ, using the equation

$$U_T = 2\sqrt{\frac{\Delta^2}{3} + \frac{S^2}{N}} .\tag{18}$$

Table 9 lists the systematic uncertainty, ranges of values for the random uncertainties, and total uncertainties for each wattmeter.

6. Conclusion

The calibration of high power cw wattmeters is accomplished using the cascaded coupler technique. Directional couplers are used to extend the range of low power meters up to the kilowatt range. Although this technique is quite cumbersome and lengthy due to multiple power transfers, the standard deviations are less than 0.66% over a 6 month period for Wattmeter C in Group I. Standard deviations for all other wattmeters vary from 0.03% to 0.80% and are caused largely by the instability of the individual wattmeter. The overall uncertainty limits are 0.77% to 1.05% depending on the type of wattmeter, frequency, and power level. Wattmeters may be used to calibrate a high power source for certifying other wattmeters, thus avoiding the cascaded coupler arrangement and reducing measurement time. However, this introduces another level in the calibration structure, resulting in higher uncertainties.

Table 6. Sample standard deviations of Group I wattmeters

Freq. (MHz)	Power level (W)	Wattmeter A std. dev. %	Wattmeter B std. dev. %	Wattmeter C std. dev. %
2	1	0.11	0.13	0.24
	10	0.15	0.12	0.09
	100	0.50	0.72	0.08
	500	0.54	0.75	0.05
	1000	0.59	0.77	0.07
15	1	0.14	0.06	0.18
	10	0.10	0.06	0.10
	100	0.52	0.64	0.09
	500	0.52	0.59	0.07
	1000	0.52	0.63	0.09
30	1	0.08	0.12	0.24
	10	0.12	0.08	0.15
	100	0.51	0.57	0.11
	500	0.52	0.64	0.11
	1000	0.47	0.63	0.08
40	1	0.12	0.19	0.14
	10	0.17	0.57	0.18
	100	0.52	0.77	0.07
	300	0.61	0.70	0.20
	500	0.54	0.75	0.15
70	1	0.16	0.15	0.14
	10	0.20	0.16	0.11
	100	0.54	0.70	0.05
	300	0.51	0.66	0.15
	500	0.56	0.75	0.11
100	1	0.15	0.63	0.18
	10	0.12	0.52	0.15
	100	0.71	0.50	0.08
	300	0.58	0.56	0.07
	500	0.62	0.47	0.18
125	1	0.08	0.11	0.14
	10	0.14	0.08	0.07
	100	0.52	0.29	0.08
	300	0.51	0.32	0.07
	500	0.53	0.35	0.12
250	1	0.06	0.13	0.11
	10	0.12	0.20	0.02
	100	0.42	0.38	0.08
	300	0.46	0.37	0.06
	500	0.45	0.36	0.09
400	1	0.06	0.05	0.07
	10	0.09	0.04	0.19
	100	0.38	0.25	0.12
	300	0.33	0.30	0.17
	500	0.42	0.30	0.28

Table 7. Sample standard deviations of Group II-A wattmeter

Freq. (MHz)	Power level (W)	Wattmeter A std. dev. %
2	1	0.20
	10	0.21
	100	0.09
	200	0.07
10	1	0.15
	10	0.10
	100	0.03
	200	0.11
20	1	0.17
	10	0.11
	100	0.13
	200	0.15
30	1	0.20
	10	0.14
	100	0.59
	200	0.46
40	1	0.52
	10	0.54
	100	0.47
	200	0.37
60	1	0.49
	10	0.51
	100	0.20
	200	0.23
80	1	0.40
	10	0.43
	100	0.40
	200	0.25
100	1	0.34
	10	0.40
	100	0.33
	200	0.34

Table 8. Sample standard deviations of Group II-B wattmeter

Freq. (MHz)	Power level (W)	Wattmeter B std. dev. %
125	1	0.12
	10	0.10
	100	0.14
	200	0.12
200	1	0.23
	10	0.11
	100	0.18
	200	0.26
300	1	0.43
	10	0.52
	100	0.59
	200	0.80
400	1	0.31
	10	0.13
	100	0.18
	200	0.22
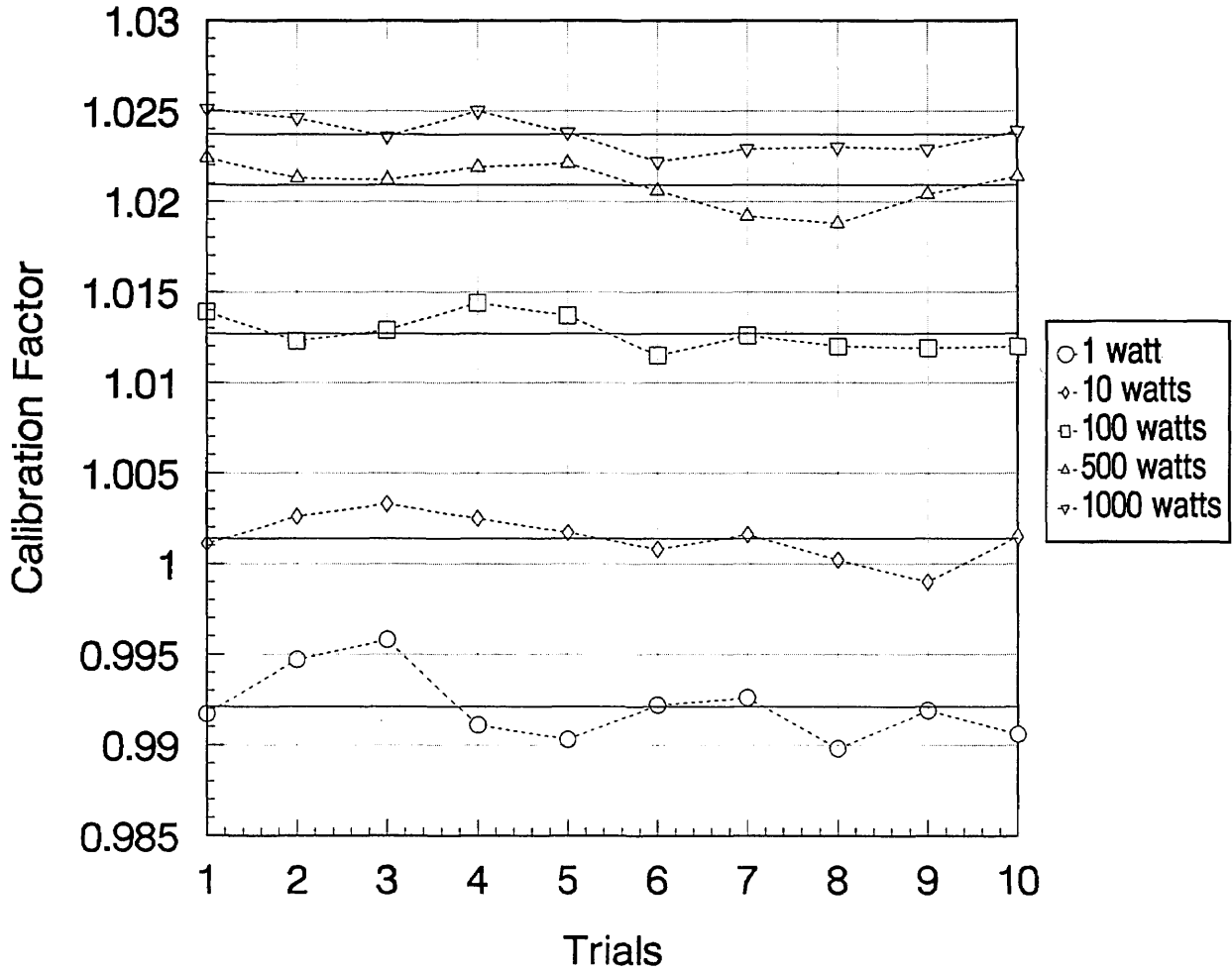
Fig. 6. Calculated values of calibration factors (ten trials) for Group I-C wattmeter at 2 MHz and at various power levels. Averages of ten trials shown as solid lines.
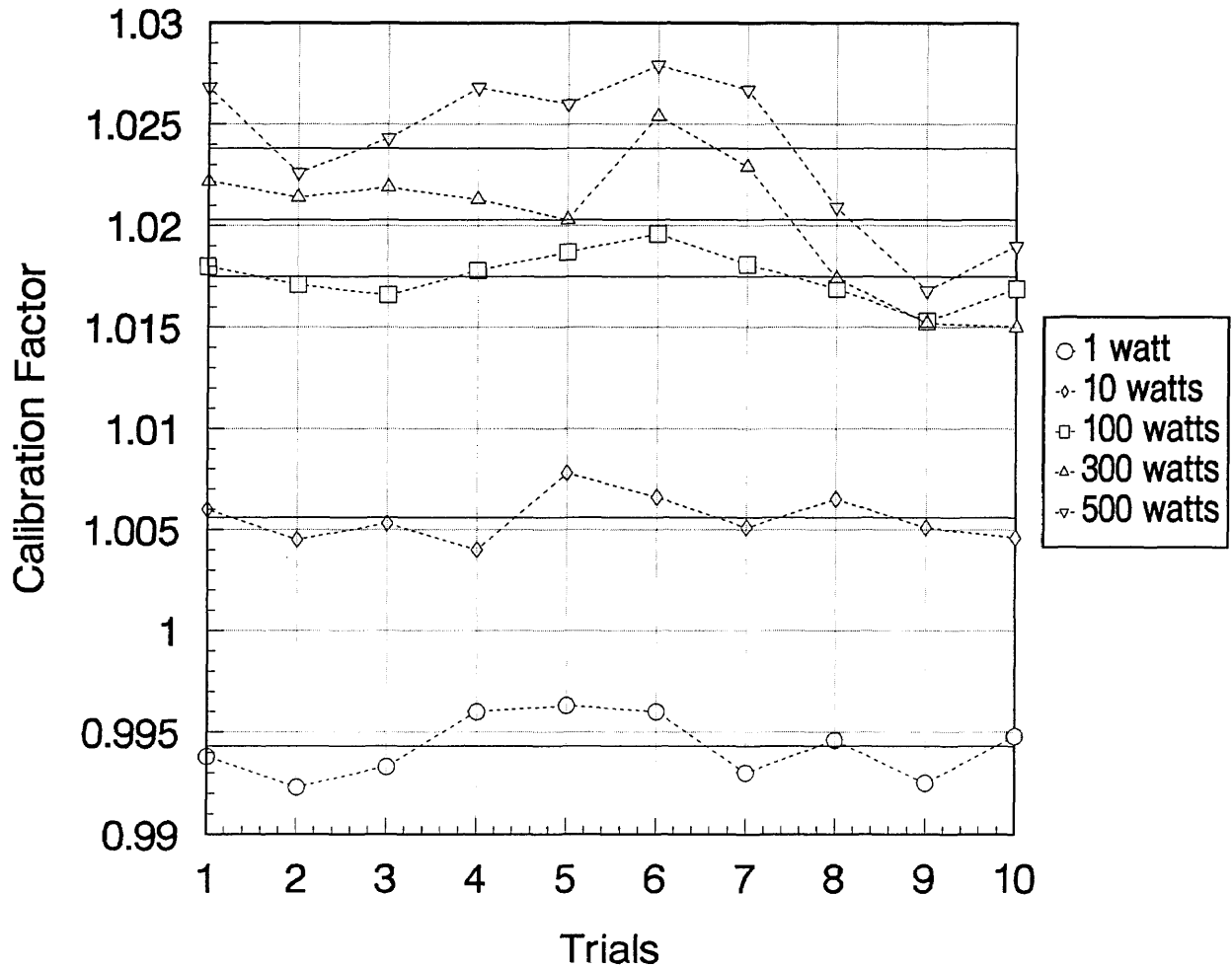
Fig. 7. Calculated values of calibration factors (ten trials) for Group I-C wattmeter at 100 MHz and at various power levels. Averages of ten trials shown as solid lines.
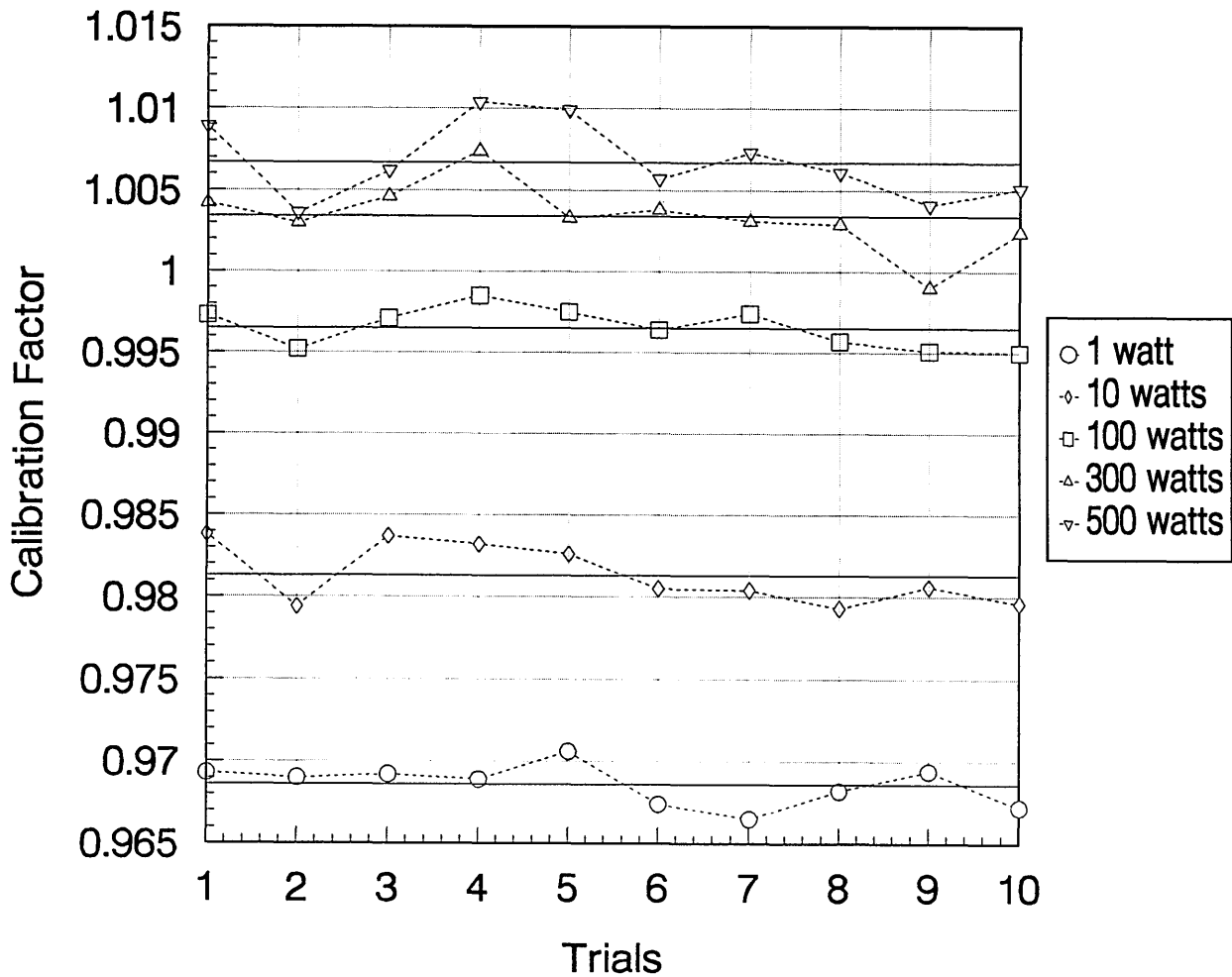
Fig. 8. Calculated values of calibration factors (ten trials) for Group I-C wattmeter at 400 MHz and at various power levels. Averages of ten trials shown as solid lines.

Table 9. Systematic uncertainties and ranges of values for the random and total uncertainties of the wattmeters

	Systematic uncertainty (%)	Random uncertainty (%)	Total uncertainty (%)
Group I			
Wattmeter A	0.67	0.06 – 0.62	0.78 – 0.95
Wattmeter B	0.67	0.04 – 0.77	0.77 – 1.04
Wattmeter C	0.67	0.02 – 0.28	0.77 – 0.81
Group II			
Wattmeter A (2–30 MHz)	0.67	0.03 – 0.59	0.77 – 0.94
Wattmeter B (30–400 MHz)	0.67	0.10 – 0.80	0.78 – 1.05

7. Appendix A

Since the impedances of the 10 mW standard and the wattmeter/load are not equal, a mismatch term, MM, is introduced [3] and is given by

$$MM = \frac{|1 - \Gamma_{GE}\Gamma_S|^2}{|1 - \Gamma_{GE}\Gamma_X|^2}, \tag{19}$$

where Γ_X and Γ_S are the reflection coefficients of the wattmeter/load combination and the power standard, respectively, and Γ_{GE} is the equivalent generator reflection coefficient.

The reflection coefficients are complex numbers and can be written in the form

$$\Gamma_{GE} = |\Gamma_{GE}|(\cos\theta_{GE} + j \sin\theta_{GE}), \tag{20}$$

$$\Gamma_S = |\Gamma_S|(\cos\theta_S + j\sin\theta_s), \tag{21}$$

$$\Gamma_X = |\Gamma_X|(\cos\theta_X + j\sin\theta_x) \tag{22}$$

where θ_{GE}, θ_S, and θ_X are the arguments of the reflection coefficients of the equivalent generator, the power standard, and the wattmeter/load combination.

The mismatch term is simplified and approximated using several steps. First, completing the squares of both the numerator and denominator of Eq. (19) gives

$$MM = \frac{|1 - 2\Gamma_{GE}\Gamma_S + (\Gamma_{GE}\Gamma_S)^2|}{|1 - 2\Gamma_{GE}\Gamma_X + (\Gamma_{GE}\Gamma_X)^2|}. \tag{23}$$

An approximation may be used by deleting the $(\Gamma_{GE}\Gamma_S)^2$ and $(\Gamma_{GE}\Gamma_S)^2$ terms since their contributions are negligible. This gives

$$MM \approx \frac{|1 - 2\Gamma_{GE}\Gamma_S|}{|1 - 2\Gamma_{GE}\Gamma_X|}. \tag{24}$$

Expanding and neglecting the higher order terms, Eq. (24) can be written as

$$MM \approx \frac{1 - 2|\Gamma_{GE}||\Gamma_S|\cos(\theta_{GE} + \theta_S)}{1 - 2|\Gamma_{GE}||\Gamma_X|\cos(\theta_{GE} + \theta_X)}. \tag{25}$$

The cosine terms can range in value from -1 to $+1$. Therefore MM has a range

$$MM \approx \frac{1 \pm 2|\Gamma_{GE}||\Gamma_S|}{1 \pm 2|\Gamma_{GE}||\Gamma_X|}. \tag{26}$$

With the uncertainties included

$$MM \approx \frac{1 \pm 2(|\Gamma_{GE}| \pm \Delta|\Gamma_{GE}|)(|\Gamma_S| \pm \Delta|\Gamma_S|)}{1 \pm 2(|\Gamma_{GE}| \pm \Delta|\Gamma_{GE}|)(|\Gamma_X| \pm \Delta|\Gamma_X|)}. \tag{27}$$

Acknowledgments

8. References

[1] Installation, Operation and Maintenance Instructions With Illustrated Parts List for Automated Wattmeter Calibration System, M/A-COM Microwave Power Devices, Inc., May 1990.

[2] K. E. Bramall, Accurate Microwave High Power Measurements Using a Cascaded Coupler Method, J. Res. Natl. Bur. Stand. (U.S.), 75C (3-4), 185–192 (1971).

[3] G. F. Engen, Recent Developments in the Field of Microwave Power Measurements at the National Bureau of Standards (U.S.), IRE Transactions on Instrumentation, I-7, 304–306 (1958).

[4] G. F. Engen, Amplitude Stabilization of a Microwave Signal Source, IRE Transactions on Microwave Theory and Techniques, MTT-6, 202–206 (1958).

[5] R. W. Beatty and A. C. Macpherson, Mismatch Errors in Microwave Power Measurements, Proc. IRE 41 (9), 1112–1119 (1953).

[6] F. R. Clague, Power Measurement System for 1 mW at 1 GHz, Natl. Inst. Stand. Technol., Technical Note 1345 (1990).

[7] N. T. Larsen, A New Self-Balancing DC-Substitution RF Power Meter, IEEE Trans. Instrum. Meas. IM-25, 343–347 (1976).

[8] G. F. Engen, A DC-RF Substitution Error in Dual-Element Bolometer Mounts, IEEE Trans. Instrum. Meas. IM-13, 58–64 (1964).

About the Authors: Gregorio Rebuldela has worked on the development and evaluation of high frequency, coaxial voltage standards and measurement systems and on the development of the low frequency dual six-port automatic network analyzer which measures the circuit parameters of one and two port devices. His current technical responsibilities as a project leader in the Electromagnetic Fields Divison at NIST include developing and evaluating cw, coaxial high power measurement systems and transfer standards, and improving and maintaining the high frequency rf voltage and low power calibration services. Jeffrey A. Jargon is a member of the Microwave Metrology Group in the NIST Electromagnetic Fields Division, where his main responsibilities are in cw, coaxial high power and high frequency voltage metrology. The National Institute of Standards and Technology is an agency of the Technology Administration, U.S. Department of Commerce.

Compact Fitting Formulas for Electron-Impact Cross Sections

Yong-Ki Kim

National Institute of Standards and Technology, Gaithersburg, MD 20899

Compact fitting formulas, which contain four fitting constants, are presented for electron-impact excitation and ionization cross sections of atoms and ions. These formulas can fit experimental and theoretical cross sections remarkably well, when resonant structures are smoothed out, from threshold to high incident electron energies (<10 keV), beyond which relativistic formulas are more appropriate. Examples of fitted cross sections for some atoms and ions are presented. The basic form of the formula is valid for both atoms and molecules.

Key words: electron-impact cross sections; excitation; fitting formulas; helium; hydrogen; ionization.

1. Introduction

For applications in plasma modeling and the study of energy deposition in matter by charged particles, various analytic formulas have been used to fit ionization and excitation cross sections, σ, of neutral atoms, ions and molecules by electron impact. The Bethe theory [1,2] provides clear guidelines for choosing such analytic formulas at high incident energies, E, for electric dipole (E1) allowed transitions:

$$\sigma(x) = x^{-1}(a \ln x + b + c/x), \quad \text{with } x = E/I, \quad (1)$$

where I is the ionization potential (or excitation energy for discrete excitations), and a, b and c are constants characteristic of the target but independent of E, or the scaled incident energy x.

The logarithmic term arises from the dipole interaction, and hence an E1-forbidden transition will begin with the b term in Eq. (1). Actually, the expansion in Eq. (1) continues after the c term in negative powers of x. The Bethe formula is based on the first Born approximation. The physical effects not represented by the Born approximation — such as the distortion of the incident wave, polarization of the target charge distribution by the incident particle, and the electron exchange effect between the incident electron and bound electrons in the target — contribute terms between the b and c terms in Eq. (1). Hence, expanding the cross section formula beyond those included in Eq. (1) becomes a futile exercise unless the additional physical effects mentioned above are also included. The fitting formulas discussed in this article are only valid for E1-allowed transitions, since we keep the logarithmic term in our formulas.

According to the Mott scattering formula, which includes the electron exchange between the projectile and target electrons (or an ejected one in our case), the interference between the scattered and ejected electrons generated by electron-impact

ionization leads to a term [2] of the form $x^{-2} \ln x$ in $\sigma(x)$. On the other hand, the distortion of the projectile wave function near the target nucleus introduces a term [3] of the form $x^{-1} \times \sigma$(plane-wave Born). Moreover, cross sections must vanish at the threshold, except for the discrete excitations of ions. The terms associated with $\ln x$ vanish for E1-forbidden transitions. Various fitting formulas [4,5] differ in the choice of functions to represent σ at low x toward the threshold at $x = 1$, and often contain more fitting constants than our formulas.

To accommodate the leading x dependence both of the electron exchange and the projectile-wave distortion mentioned earlier, it is desirable to introduce negative powers of x in the fitting formula. This was achieved by introducing $(x + D)$ in the denominator with a fitting constant D, which provides additional flexibility. We found that the following compact formulas fit known cross sections remarkably well throughout the entire range of $I \leq E \leq 10$ keV. For a cross section that vanishes at the threshold $(x = 1)$, e.g., for the ionization of atoms, ions and molecules and for the excitations of neutral atoms and molecules, we use

$$\sigma(x)x \equiv S(x) = A \ln x + [B \ln x + C(x - 1)]/(x + D),$$
$$(2)$$

where $S(x)$ is a scaled collision strength and A, B, C, and D are fitting constants. Cross sections for the E1-allowed excitations of ions do not vanish at thresholds, i.e., $\sigma(x = 1) > 0$. In this case, we use

$$\sigma(x)x \equiv S(x) = A \ln x + (B \ln x + Cx)/(x + D).$$
$$(3)$$

The scaled collision strength, $S(x)$, monotonically increases with x in most cases, and the fitting constants are better determined using S rather than σ itself, particularly when the asymptotic behavior of the cross section at high x is known either through actual measurements or theories such as the Born approximation.

Often, electron-impact cross sections close to thresholds are crowded with resonances, mostly through the formation of transient multiply-excited states or negative ion states. Fitting formulas presented in this report are too simple to reproduce such resonances.

In Table 1, we list fitting constants [see Eq. (2)] that reproduce electron-impact ionization cross sections for some first-row atoms and ions. For the hydrogen atom, we fitted to the experimental ionization cross section measured by Shah, Elliott, and

Gilbody [6]. For the helium atom, we used the experimental ionization cross section by Shah et al. [7] and the asymptotic Bethe cross sections by Kim and Inokuti [2]. For the ionization of He^+ and Li^+, the cross sections measured by Dolder and coworkers [8,9] and the asymptotic cross sections from Ref. [2] were used. Our fitting reproduces the original data within a few percent, except for minor local departures mostly near ionization thresholds.

Table 1. The constants I, A, B, C, and D [see Eq. (2)] for electron-impact ionization of atoms and ions. The ionization potential I is given in eV, and the fitting constants A, B, C, and D are in 10^{-16} cm^2

Atom	I(eV)	A	B	$-C$	D
H	13.61	0.7576	−5.521	5.867	2.948
He	24.58	0.7326	−5.117	3.295	2.468
He$^+$	54.42	0.06233	−0.2982	0.2835	0.327
Li$^+$	75.60	0.08329	−0.4476	0.3225	4.252

We note that the ionization cross section of the hydrogen atom recommended in Ref. [5] is about 15% higher than the latest experimental value [6] at the peak cross section. These two cross sections are compared in Fig. 1.
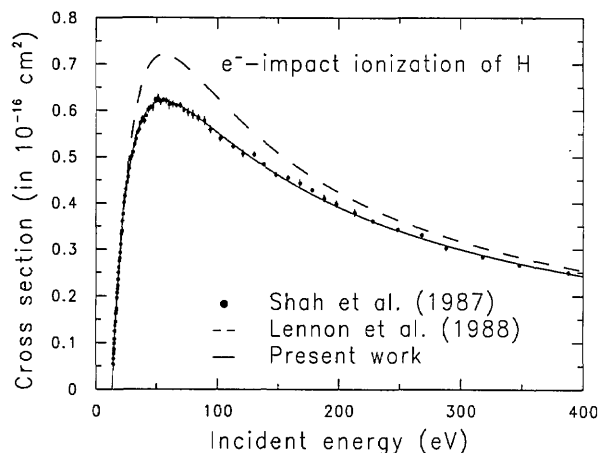
Fig. 1. Cross section for the ionization of the hydrogen atom by electron impact. Solid circles represent the experiment by Shah, Elliott, and Gilbody [6], the dashed curve represents the cross section recommended by the Belfast group [5], and the solid curve is our fitting to the experimental data [6].

As an example of E1-allowed discrete excitations, fitting constants [see Eqs. (2) and (3)] for the $1s^2\,^1S \rightarrow 1snp\,^1P$ $(n = 2-4)$ excitations of He [10,11] and the $2s\,^2S \rightarrow 2p\,^2P$ excitation of C^{3+} by

electron impact [12] are listed in Table 2. The He excitation cross sections were combined with the Bethe cross sections at high incident energies [13]. Also, the experimental data on the excitation of C^{3+} by Taylor et al. [12] were smoothly joined to the plane-wave Born cross section at high incident energies using the shape of the distorted-wave Born cross section. The Born cross sections were evaluated by the present author using Hartree-Fock wave functions for the ground and the $2p$ ^2P states as is shown in Fig. 2. Equation (2) should also be useful in fitting electron-impact cross sections for molecules.

Table 2. The constants I, A, B, C and D [see Eq. (2)] for the $1s^2\,^1S \rightarrow 1snp$ ^1P ($n = 1-4$) transition of He and the $2s$ $^2S \rightarrow 2p$ ^2P excitation of C^{3+} by electron impact. The excitation energy I is given in eV, and the fitting constants A, B, C, and D are in Å^2

Atom	Excited state	I(eV)	A	B	C	D
He	$1s\,2p\,^1P$	21.22	0.3991	-0.3314	-0.00325	-0.012
He	$1s\,3p\,^1P$	23.09	0.08978	-0.0499	0.01003	-0.789
He	$1s\,4p\,^1P$	23.75	0.03488	-0.0286	0.00571	-0.343
C^{3+}	$2p\,^2P$	8.004	3.938	6.373	0.0061	-0.999
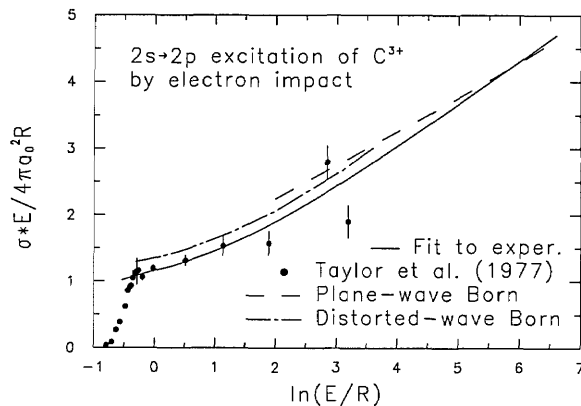
Fig. 2. Collision strength for the $2s$ $^2S \rightarrow 2p$ ^2P excitation of C^{3+} by electron impact. The plane-wave and distorted-wave Born cross sections were calculated by the present author using Hartree-Fock wave functions. In the figure, σ is the cross section, E is the incident electron energy, a_0 is the Bohr radius (5.29 nm), and R is the rydberg energy (13.6 eV).

To calculate the rate coefficients $\langle \sigma v \rangle$ averaged over a Maxwellian distribution, we recommend that eight-point Laguerre quadrature be used, as suggested in Ref. [5]:

$$\langle \sigma v \rangle = 6.692 \times 10^7 \, (kT)^{1/2} \, \Sigma_i \, \omega_i \, S \, (1 + kT x_i/I), \quad (4)$$

where kT is the (plasma) electron temperature in eV, and ω_i and x_i are the Laguerre quadrature weights and abscissas, respectively.

Note that the integration formula (8) in Ref. [5] has a misprint: x_i there should be replaced by $(x_i + I/kT)$. Nevertheless, the rates reported in Ref. [5] are correct. The fitting constants in Tables 1 and 2 will lead to cross sections in $10^{-16}\,\text{cm}^2$ and collision rates in cm^3/s.

For E1-forbidden transitions, the logarithmic terms in the fitting formulas vanish. The remaining two terms with C and D coefficients alone do not provide enough flexibility to fit E1-forbidden cross sections except in unusually simple cases. Instead, a power series in $(x - 1)$,

$$\sigma x = \Sigma_i A_i (x - 1)^i, \quad (5)$$

where th A_i are fitted coefficients $(i \leq 5)$, should be adequate to reproduce most E1-forbidden cross sections.

Also, the formulas presented here are not suitable for fitting proton-impact ionization cross sections at low incident energies, say $E \sim 300$ keV or lower, because the analytic form used here cannot account for ionization by charge transfer—an electron in the target attaching itself to the incident proton—which begins to dominate the ionization process at $E \sim 300$ keV and below.

Acknowledgments

2. References

[1] H. Bethe, Ann. Physik 5, 325 (1930).

[2] Y.-K. Kim and M. Inokuti, Phys. Rev. A 3, 665 (1971).

[3] Y.-K. Kim and J. P. Desclaux, Phys. Rev. A 38, 1805 (1988).

[4] S. M. Younger, J. Quant. Spectrosc. Radiat. Transfer 26, 329 (1981).

[5] M. A. Lennon, K. L. Bell, H. B. Gilbody, J. G. Hughes, A. E. Kingston, M. J. Murray, and F. J. Smith, J. Phys. Chem. Ref. Data 17, 1285 (1988).

[6] M. B. Shah, D. S. Elliott, and H. B. Gilbody, J. Phys. B 20, 3501 (1987).

[7] M. B. Shah, D. S. Elliott, P. McCallion, and H. B. Gilbody, J. Phys. B 21, 2751 (1988).

[8] B. Peart, D. S. Walton, and K. T. Dolder, J. Phys. B 2, 1347 (1969).

[9] J. B. Wareing and K. T. Dolder, Proc. Phys. Soc. (London) 91, 887 (1967).

[10] D. E. Shemansky, J. M. Ajello, D. T. Hall, and B. Franklin, Astrophys. J. **296**, 771 (1980).
[11] D. C. Cartwright, G. Csanak, S. Trajmar, and D. F. Register, Phys. Rev. A **45**, 1602 (1992); Erratum, *ibid*. A **46**, 696 (1992).
[12] P. O. Taylor, D. Gregory, G. H. Dunn, R. A. Phaneuf, and D. H. Crandall, Phys. Rev. Lett. **39**, 1256 (1977).
[13] Y.-K. Kim and M. Inokuti, Phys. Rev. **175**, 176 (1968); *ibid*. **184**, 38 (1969).

About the author: *Yong-Ki Kim is a supervisory phycisist in the Atomic Physics Division at NIST. The National Institute of Standards and Technology is an agency of the Technology Administration, U.S. Department of Commerce.*

Accuracy of the Double Variation Technique of Refractive Index Measurement

Jennifer R. Verkouteren,
Eric B. Steel, Eric S. Windsor,
and John M. Phelps

National Institute of Standards
and Technology,
Gaithersburg, MD 20899

Errors in the double variation technique of refractive index measurement are analyzed using a new approach. The ability to measure matching wavelength is characterized, along with the effect on the calculated refractive index. Refractive index accuracy and precision are very dependent on the specifics of each calibration set, particularly the difference in dispersion between the liquid and solid. Our best precision (± 1 or 2×10^{-4}) is attained only when the difference in dispersion between liquid and solid is small, and is dependent on an individual operator's ability to perceive changes in relief. This precision is impossible to achieve for the other glass/liquid combinations, where we are limited by a precision of approximately 1 nm in the selection of matching wavelength. A bias in the measurement of matching wavelength exists that affects the accuracy of the calculated refractive indices. The magnitude of the bias appears to be controlled by the bandpass of the graded interference filter. The errors in refractive index using a graded interference filter with a bandpass of 30 nm FWHM (full width at half maximum intensity) are an order of magnitude larger than the errors using a filter with a bandpass of 15 nm FWHM.

Key words: dispersion; double variation; immersion method; optical properties; polarized light microscopy; refractive index.

1. Introduction

One of the tasks in our laboratory was to characterize the optical properties of asbestos minerals to serve as NIST Standard Reference Materials (SRMs). Mine-grade chrysotile, amosite, and crocidolite were to be made available as SRM 1866 [1] with certified values for all optical properties, and in particular, refractive index. The SRM is intended to serve as a calibration standard for laboratories that analyze bulk materials for asbestos using polarized light microscopy. Refractive index is a primary optical property used to characterize transparent minerals, including asbestos, during microscopic analysis. Immersion techniques for microscopic measurement of refractive index such as Becke line, oblique illumination, and focal masking

are used routinely for refractive index measurement to the third place [2]. To characterize reference materials for use with these techniques, we need to use a method with higher accuracy and precision.

There are several microscopic techniques to measure refractive index accurately to the fourth place, including interferometry [3], the variation of temperature at constant wavelength (single variation) [4], and the double variation technique [5-8]. We decided to use the double variation technique for our measurements because we expected it to be an improvement on the single variation technique. The double variation technique requires the control of temperature and wavelength to match the

refractive index of the liquid to that of the unknown solid. The solid is immersed in a liquid of known refractive index and dispersion, the temperature is held constant at some value between 20 and 35 °C, and the wavelength of the illuminating light is varied until the refractive index of the solid and liquid are observed to match, as indicated by a minimum of contrast. The temperature is then set to a new value and the process of determining the wavelength at which solid and liquid match in refractive index is repeated. The refractive index of the solid is calculated for each set of temperature/matching wavelength measurements using the dispersion equation and temperature coefficient of the liquid. The refractive indices thus determined are fit to standard dispersion equations, such as the Cauchy or Sellmeier equation [9] to describe the dispersion of the solid throughout the measured range of wavelengths.

References [6,7] describe a bias in refractive index measurements with respect to wavelength using the double variation technique which the authors attribute to the color sensitivity of the human eye. The measured values are biased high at wavelengths <555 nm and are biased low at wavelengths >555 nm. The systematic errors reported are on the order of $\pm 2 \times 10^{-4}$. Reference [8] describes an approach to correcting the bias by measuring a glass calibration standard closely matched in refractive index to the unknown. A refractive index correction value for each wavelength (Δn_λ) is calculated as $n_{meas} - n_{true}$ for the glass in question and is then applied to the measurements of the unknown, resulting in an accuracy and precision of approximately $\pm 1 \times 10^{-4}$.

We obtained calibration glasses with refractive indices closely matched to the asbestos minerals and placed the appropriate glass in the heating stage alongside the asbestos mineral as an internal standard. We observed a bias with respect to wavelength of the same general nature reported earlier, however, the magnitude of the bias was at least a factor of ten larger. The errors were too large to correct for in the manner described in Ref. [8]. We began a systematic study of the variables involved in the measurement process and developed a different approach to assessing the errors in refractive index. This approach, in which we characterize the errors in the determination of the wavelength at which solid and liquid match in refractive index at each temperature, as opposed to characterizing the errors in refractive index with wavelength, provides a better understanding of the variables which control the accuracy and precision of the technique.

This error analysis also allowed us to determine information concerning the measurement bias and the variables that control it.

2. Calibration

The calibration procedures for the equipment used in the measurement process and the results of the calibrations are given below. For a more detailed description of the types of equipment used in the double variation technique, including heating stages, illumination sources, immersion liquids, and refractometers, see Ref. [6].

2.1 Filter Calibration

We used three different filters in conjunction with the quartz halogen light source on our microscope: 1) a narrow-bandpass graded interference filter (GIF), 2) a broad-bandpass GIF, and 3) a set of seven fixed-wavelength interference filters. The narrow-bandpass GIF has a minimum bandpass of 15 nm full width at half the maximum intensity (FWHM), the broad-bandpass GIF has a minimum bandpass of 30 nm FWHM, and the fixed-wavelength filters each have a bandpass of 10 nm FWHM. A GIF is a 20 cm long rectangular interference filter that grades in thickness from one end to the other, allowing the selection of peak wavelengths from approximately 350 to 750 nm. The filter is marked from 1 to 200 in millimeter increments, and is calibrated at 16 positions by the manufacturer to determine the correspondence between filter position and peak wavelength. The filter holder has an exit slit which can be opened to a maximum width of 20 mm. The bandpass of the transmission peak is increased by opening the exit slit. The set of seven fixed-wavelength filters is designed to isolate the common spectral lines in the visible spectrum with transmittance peaks at 405, 436, 486, 546, 577, 589, and 656 nm.

The filters were each calibrated for wavelength and bandpass using a spectrophotometer. The spectrophotometer was first calibrated for wavelength at 589.3 (the mean of the doublet at 589.6 and 589.0 nm) using a sodium arc lamp, and at 546.1 and 435.8 nm using a mercury arc lamp. The filters were then calibrated using a tungsten light source to transmit white light through the filter, collecting the transmitted light with the spectrophotometer. The data were corrected for both the source characteristics and the relative sensitivity of the detector using a blank spectrum collected under the same conditions. The peak wavelength of

the transmission curve is determined as the centroid of the peak, and the bandpass is measured graphically. The GIFs were calibrated at eight positions of the filter, corresponding to a range in wavelength of 440–630 nm, with the exit slit fixed at 2 mm. The narrow-bandpass GIF was also measured at one position (wavelength) but with a variation in slit width of 2–20 mm.

Our wavelength measurements for one of the GIFs disagreed with the manufacturer's calibration measurements by 8 nm, with the same 8 nm discrepancy at each measured position. The measurements of the other GIF and the fixed-wavelength filters agreed with the manufacturers' values. The bandpasses at FWHM for the two GIFs determined with the exit slit at 2 mm agree with the manufacturer's values. (The manufacturers do not specify a slit size for their bandpass measurements.) If the exit slit is much narrower than 2 mm, the amount of light transmitted is insufficient to illuminate the microscope field. The transmission of a filter that is graded in thickness is complex, and the changes due to changing the size of the exit slit are difficult to predict. We measured the transmission of the narrow-bandpass GIF as a function of slit size, opening the slit symmetrically about the center position. The FWHM of the transmission peak increased from 15 nm for a 2 mm slit, to 32 nm at the fully open position (20 mm). The shape of the transmission curve also changed with slit size, with the FWHM increasing at a greater rate than the width at 1% of the peak height. Therefore, although the FWHM of the two GIFs are both approximately equivalent when the exit slit of the narrow-bandpass GIF is fully opened and the exit slit of the broad-bandpass GIF is at the minimum operating width, the transmission peaks are not equivalent.

The two GIFs differ in bandpass (15 or 30 nm FWHM) and also in transmission efficiency. The manufacturer states a transmission efficiency of 60% for the narrow-bandpass GIF and 30% for the broad-bandpass GIF. We did not measure the transmission efficiency of the filters; however, the change in brightness of the field of view supports the relative difference in efficiency given for the two GIFs. We could also see a difference in field illumination using the two GIFs that may reflect the difference in bandpass. Using the broad-bandpass GIF, we could see faint Becke lines with different colors than the field, such as red and blue Becke lines on a green field, whereas with the narrow-bandpass GIF and the fixed-wavelength filters, the Becke lines are simply intensity variations of the field color. The transmission efficiency of each

fixed-wavelength filter is listed as approximately 60%, which again is in relative agreement with our observations of brightness in the field of view.

2.2 Immersion Liquids

The immersion liquids used in this study were obtained from Cargille.[1] The refractive index at 589.3 nm was measured on a Zeiss Abbe-type refractometer (with an Amici prism) and a Bellingham and Stanley precision refractometer (without an Amici prism). The temperature was measured on the Zeiss refractometer with the instrument's fixed thermometer, and the temperature on the Bellingham and Stanley refractometer was measured with an E-type thermocouple placed on the measuring prism. The refractive index measurements of the liquids are within $\pm 2 \times 10^{-4}$ of the value given by Cargille. In addition, the value $n_F - n_C$, which is a measure of the dispersion between 486.1 nm (F) and 656.3 nm (C), was determined for each liquid on the Zeiss refractometer using the Amici prism, and was again found to be within $\pm 2 \times 10^{-4}$ of the value given by Cargille. Therefore, the dispersion equations of the liquids (Cauchy equations) provided by Cargille were used in this study.

We found that the errors in measurements at wavelengths other than 589.3 using the Bellingham and Stanley refractometer precluded the use of the data to determine the dispersion of the liquids independently. The errors were determined by measuring three SRMs designed for testing refractometers; SRM 1822 [10] and SRM 1823 [11]. The question of uncertainty in the liquid dispersions is addressed later in this paper.

2.3 Calibration Glasses

The glasses used in this study were obtained from D. Blackburn and D. Kauffman of the Mechanical Properties Group at NIST. The glasses were made at NIST approximately 30 years ago, and the refractive indices were characterized at that time using the minimum deviation technique [9] which is a high accuracy technique commonly used for the measurement of glasses. The technique requires

---

[1] Certain commercial equipment, instruments, or materials are identified in this paper to specify adequately the experimental procedure. Such identification does not imply recommendation or endorsement by the National Institute of Standards and Technology, nor does it imply that the materials or equipment identified are necessarily the best available for the purpose.

that the glass be in the form of a prism with polished surfaces. The nomenclature used to identify the glasses when they were prepared was retained in this study. Each of the four glasses is identified by an alphabetic character followed by three or four digits. The refractive indices of some of the glasses were measured prior to this study by M. Dodge at NIST using the minimum deviation technique. The results agree with the earlier measurements and are accurate to $\pm 5 \times 10^{-5}$. The values at four wavelengths distributed across the visible spectrum were fit to a Cauchy equation using a least squares fit. A fit to a linearized Sellmeier equation [7] did not differ from a fit to a Cauchy equation by more than $\pm 5 \times 10^{-6}$, which is within the level of accuracy of the data; thus the mathematically simpler Cauchy equation and fit were used.

2.4 Heating Stage

The performance of the thermocouple in the heating stage during a temperature ramp was determined by placing a reference thermocouple in the immersion cell with its tip in close proximity to the stage thermocouple. We detected a problem in one of our commercial stages using this procedure. We found that the temperature readings were normal at room temperature and became anomalously high with increasing temperature. The thermocouple was not out of calibration, but instead was receiving additional heat from the wire used to heat the metal stage, and therefore was not providing a reliable measurement of the temperature of the immersion liquid. This problem was rectified by changing the placement of the stage thermocouple to remove it from proximity to the heating wire. A new heating stage was constructed in-house with this new design.

The thermocouple in the heating stage is accurate to ± 0.1 °C at all temperatures between room temperature and 35 °C, and there is no temperature gradient in the immersion cell. The compositional stability of the liquids with temperature was tested by cycling the temperature up and down while measuring the refractive index of the calibration glasses. The liquids were found to be stable through at least two repeated ramps.

3. Experimental Design

We tested the measurement accuracy of the double variation technique using glasses with well

characterized refractive indices that cover the range of the asbestos minerals. There are seven sets of glass/liquid calibration data, with a set defined as the measurements of one glass in one liquid. The liquids and calibration glasses are listed in Table 1 along with the wavelength range over which the calibration measurements were performed.

Table 1. Calibration sets

Liquid n_D	Glass	Glass n_D	Glass V[a]	λ_m Range (nm)
1.552	F1152	1.5549	0.017	463–564
1.556	F1152	1.5549	0.017	526–666
1.558	F1152	1.5549	0.017	560–674
1.674	A574	1.6820	0.018	497–540
1.678	E1889	1.6783	0.033	518–619
1.682	A574	1.6820	0.018	545–609
1.694	E1442	1.7110	0.020	460–491

[a] Dispersive power $V = n_F - n_C/n_D - 1$ (Jenkins and White, 1976).

Refractive index is measured by placing grains of the appropriate glass in the calibrated liquid to select the wavelength at which solid and liquid match at the given temperature. A match is indicated by a minimum of relief. At matching conditions, the dispersion curve of the glass [Eq. (1)] and the dispersion curve of the liquid [Eq. (2)] intersect. Cauchy equations, as given in Eqs. (1) and (2), are commonly used to describe the dispersion of materials in the visible region of the spectrum [9].

$$n_{gls} = a + \frac{b}{\lambda^2} + \frac{c}{\lambda^4},\qquad(1)$$

$$n_{liq} = d + \frac{e}{\lambda^2} + \frac{f}{\lambda^4} + [(T-25)\cdot dn/dT].\qquad(2)$$

Temperature coefficients (dn/dT) of the liquids are negative, and are on the order of 5×10^{-4}/°C. Temperature coefficients of most glasses are two orders of magnitude lower and are usually neglected for this range of temperature. The effect of glass temperature coefficients is discussed later in the paper.

For any given intersection (m) of the two dispersion curves, refractive index (n), wavelength (λ), and temperature (T) are uniquely defined. To determine the accuracy and precision of our measurements, we need to know the set of $(n, \lambda, T)_m$ for $T = 20$–35 °C, which is our temperature range, for

each calibration set. All possible values of n_m are given by the dispersion equation of the glass. Setting Eqs. (1) and (2) equal to each other and rewriting for T allows T_m to be calculated, as given in Eq. (3):

for $n_{gls} = n_{liq}$:

$$T_m = \frac{a + \frac{b}{\lambda^2} + \frac{c}{\lambda^4} + (25 \cdot \mathrm{d}n/\mathrm{d}T) - (d + \frac{e}{\lambda^2} + \frac{f}{\lambda^4})}{\mathrm{d}n\,\mathrm{d}T} . \quad (3)$$

The resulting $(T,\lambda)_m$ data calculated from Eq. (3) for each calibration set were fit by least squares to a polynomial using DATAPLOT [12] to generate an expression that solves for λ_m at any T_m. For all calibration sets, a quadratic or cubic equation was sufficient to achieve residuals from the fit of λ_m to T_m of ≤ 0.05 nm.

Because of the relationship among the variables n, λ, and T, we can look at our measurement errors in terms of any of the three. We chose to analyze the errors in T and λ, since they are the variables that we measure directly, and apply the results to the calculation of n. Due to the design of the experiment, in which we hold temperature constant during the measurement and vary wavelength to make a match, it is appropriate to view temperature as the independent variable and wavelength as the dependent variable, and determine our errors in measuring λ_m. This assignment of variables fits the assumptions of most statistical approaches in which there is little or no error in the independent variable, and all error in the dependent variable. The same assumption of error does not hold however, if the data are analyzed in the more conventional way as (λ, n) pairs.

Figure 1a illustrates the double variation technique and the relationship of n, λ, and T in the measurement of calibration glass E1442 in liquid 1.694 from 20 to 35 °C. The intersections between the two curves for that range of temperatures are shown by the bold line, which contains all possible $(n, \lambda, T)_m$ for that calibration set. Figure 1b is a representation of $(n, \lambda, T)_m$ in λ, T space. The "true" λ_m at each T is given by the solid line in Fig. 1b, with our measurements of λ_m given by the squares. The λ_m measurement errors $(\Delta \lambda_m)$, calculated as $\lambda_m^{meas} - \lambda_m^{true}$, are shown by the squares in Fig. 1c. A linear fit to the measurement errors is shown by the solid line in Fig. 1c, and will be discussed later in this paper.

The relationship between the error in the measurement of λ_m and errors in the calculated n is
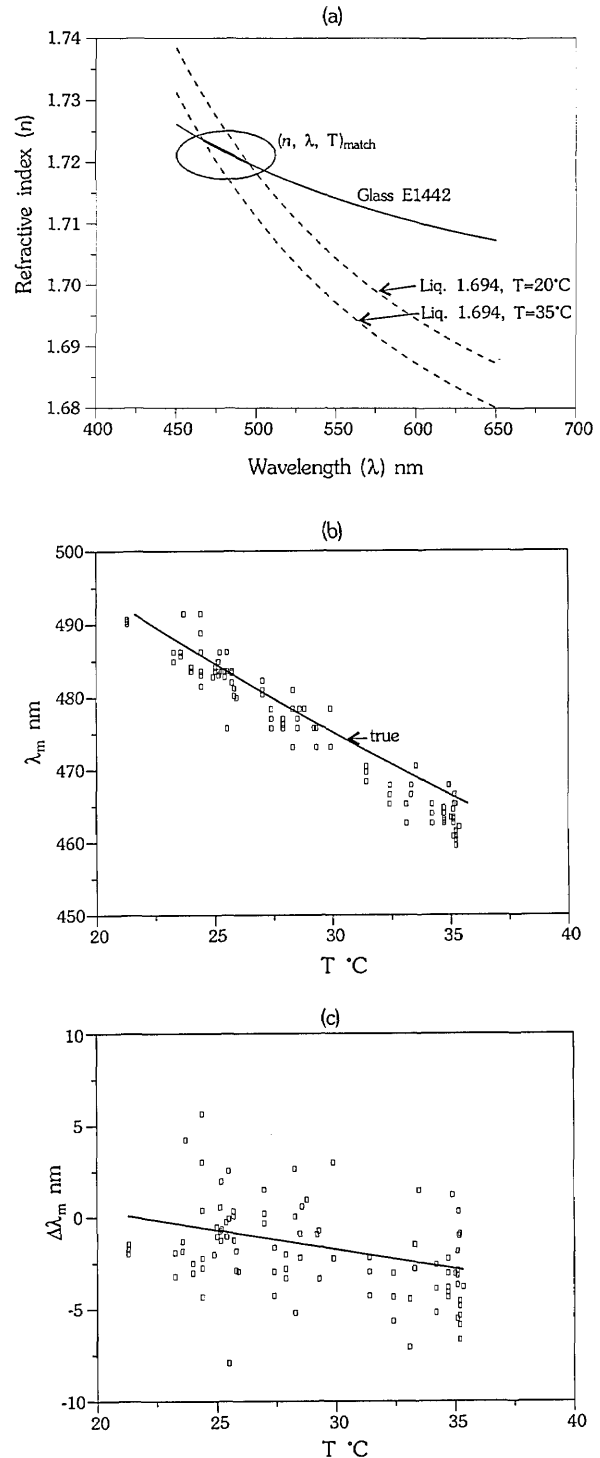
Fig. 1. Generation of $\Delta \lambda_m$: (a) segment of E1442 dispersion curve measured in liquid 1.694 between 20 and 35 °C given by bold line, (b) calibration measurements (squares) vs true (solid line), and (c) errors calculated as $\lambda_{meas} - \lambda_{true}$ (squares) with least squares linear fit (solid line).

dependent on the difference in dispersion between the liquid and the solid. The relationship stems from the fact that the refractive index of the solid is calculated from the dispersion equation of the liquid. Figure 2 illustrates this point for a glass measured in two liquids of different dispersion. For an error of ± 1 nm in the determination of λ_m, the error in the calculated n is larger when the glass is measured in the high dispersion liquid. This relationship between the error in n and the difference in dispersion between the glass and the liquid is important to the discussion of the technique, and will be referred to frequently. We define the difference in dispersion between the glass and liquid as the difference in refractive index between the glass and the liquid at ± 1 nm of λ_m [$(n_{gls} - n_{liq})$ @$\lambda_m \pm 1$ nm]. This value varies slightly with wavelength for each glass/liquid calibration set and is a quantitative description of the relief of the glass grain at ± 1 nm of match conditions.
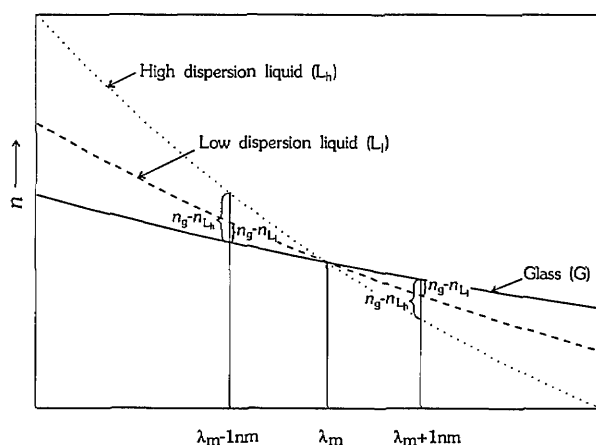
Fig. 2. Effect of liquid dispersion on refractive index errors.

Other variables in the experiment in addition to λ, n, T, and dispersion include the operator and the filter. As mentioned before, the seven calibration sets, comprising seven immersion liquids and four glasses, were chosen for the analysis of the asbestos reference materials, but also allow us to test the effects of differences in dispersion. Three operators performed the measurements, and differences due to operator bias are discussed. The data for the seven calibration sets were collected using the narrow-bandpass GIF with a 2 mm exit slit. Additional measurements were performed using the fixed-wavelength filters, the narrow-bandpass GIF with the slit fully opened, and the broad-bandpass GIF to test the effects of bandpass.

Each operator measured at least two grains of each glass in each liquid from independent preparations. The measurements of λ_m were performed for each glass grain at three temperatures; one at room temperature, a second between room temperature and 35 °C, and a third at approximately 35 °C. The measurements were always made in order of increasing temperature, and three measurements were made at each temperature. The measurements were made when the temperature in the immersion cell had stabilized; the temperature did not vary by more than 0.1 °C for any set of three measurements.

4. Results

The (T, λ_m) data collected for each glass/liquid calibration set listed in Table 1 were converted to $(\Delta\lambda_m, T)$, as shown in Figs. 1b and 1c, to provide common ground on which to compare all calibration sets. Both the precision and the accuracy of the measurements were determined using the data in this form. The accuracy was additionally determined by converting the (T, λ_m) data to (λ, n) to determine errors in the dispersion curves calculated from the measured data.

4.1 Precision

The precision of the λ_m measurement, as indicated by the variation of the measurements at each T in Figs. 1b and 1c, was calculated as one standard deviation (1σ) of the mean of the residuals from a linear fit to $(\Delta\lambda_m, T)$ for each calibration set. The precision was calculated separately for each operator's data, and also for the combined set of data. The precision of each operator, and of the combined dataset (all), is given in Table 2, where the glass/liquid calibration sets are identified by n_D of the liquid used. The difference in dispersion between liquid and glass is given by $(n_{gls} - n_{liq})$ @$\lambda_m \pm 1$ nm, which describes quantitatively the relief of the glass in the liquid. The slopes of the two curves change with wavelength, and therefore $(n_{gls} - n_{liq})$ @$\lambda_m \pm 1$ nm varies with wavelength. The range given for $(n_{gls} - n_{liq})$ @$\lambda_m \pm 1$ nm for each calibration set represents a dependence on wavelength, and decreases with increasing wavelength. The range in λ_m for each calibration set is given in Table 1.

The precision can be interpreted with respect to Fig. 2, in which the solid is measured in either a high dispersion liquid $(V \geq 0.050)$ or a low dispersion liquid $(V = 0.031)$. (The dispersion of the glass remains relatively constant $(V = 0.017 - 0.020)$, except for calibration set 1.678 which has a higher

Table 2. λ_m precision

Set	Op1	Op2	Op3	All[a]	Liq V[b]	$(n_{gls} - n_{liq})$
		$1\sigma\lambda_m$ (nm)				$@\lambda_m \pm 1$ nm $\times 10^{-4}$
1.552	±2.8	±3.7	±2.2	±3.3	0.031	0.9–0.8
1.556	±2.8	±3.5	±3.1	±4.6	0.031	0.6–0.3
1.558	±3.1	±3.5	±3.2	±3.5	0.031	0.5–0.3
1.674	±1.7	±2.0	±1.3	±2.0	0.050	1.9–1.7
1.678	±1.5	±2.9	±1.1	±2.0	0.050	0.9–0.6
1.682	±1.6	±2.7	±1.7	±2.3	0.053	1.4–1.0
1.694	±1.6	±2.9	±1.3	±2.4	0.053	3.1–2.3

[a] Determined from combined dataset.
[b] Dispersive power $V = n_F - n_C/n_D - 1$.

dispersion glass ($V = 0.033$).) The λ_m measurements are more precise in the high dispersion liquids than in the low dispersion liquids. The precision is operator dependent, but this basic categorization holds for all three. Operators 1 and 3 have an average 1σ of approximately 1.5 nm for the high dispersion liquids and an average 1σ of approximately 3 nm for the low dispersion liquids. Operator 2 is less precise but follows the same trends. The improvement in precision with increasing liquid dispersion and therefore increasing $(n_{gls} - n_{liq})$ $@\lambda_m \pm 1$ nm indicates that the amount of relief influences the precision of the measurement, which is a reasonable conclusion. The precision also seems to have a lower boundary at 1σ equal to approximately 1 nm, beyond which the relief can increase without an additional improvement in precision. The precision for set 1.694 is comparable to the other high dispersion liquid sets, even though this set has the highest relief. This probably represents a limitation of the GIF in that it may not be capable of providing peak wavelengths with a separation of better than approximately 1 nm.

The precision in n for the measurements can be calculated by multiplying the λ_m precision by $(n_{gls} - n_{liq})$ $@\lambda_m \pm 1$ nm, which defines the error in n for each 1 nm error in λ_m. The precision in n, calculated using the mean value of $(n_{gls} - n_{liq})$ $@\lambda_m \pm 1$ nm for each calibration set, is given in Table 3. The precision in n for the low dispersion liquids, where relief is the controlling factor, is between $\pm 1 \times 10^{-4}$ and $\pm 2.4 \times 10^{-4}$ for operators 1 and 3. The precision degrades for the high dispersion liquids with the exception of set 1.678, which has a high glass dispersion and thus a lower relief. The precision in λ_m, and thus n, for the high relief calibration sets is ultimately controlled by the ~ 1 nm limitation in λ_m. Therefore, for calibration set 1.694, the precision in n is poor even though the precision in λ_m is comparable to other sets, due

solely to the high relief. Put in another way, to achieve a precision in n of approximately $\pm 1 \times 10^{-4}$ for calibration set 1.694 requires a precision in the measurement of λ_m of approximately ± 0.4 nm or better, which appears to be beyond our measurement capabilities.

The precision of the measurements can be summarized as follows: at best we can discriminate changes in relief of approximately 1×10^{-4} and our best precision in the measurement of λ_m is ~ 1 nm. Because we cannot measure λ_m with a precision better than ~ 1 nm, a difference in dispersion between the liquid and solid which results in $(n_{gls} - n_{liq})$ $@\lambda_m \pm 1$ nm of greater than $\pm 1 \times 10^{-4}$, will result in an imprecision in n that is larger than $\pm 1 \times 10^{-4}$.

The precision of the λ_m measurements, as given in Table 2, is described in terms of individual operators, and also in terms of the combined data set. For each calibration set, 1σ for the combined dataset is larger than the average of the three operators, indicating a bias among operators. Analysis of the average value of λ_m at a given temperature for each operator indicates that operator 1 has a consistent negative bias on the order of approximately 1 nm with respect to the other two operators. It is possible to correct this type of problem through retraining of the operator or by the determination of calibration curves for each operator.

Table 3. n measurement precision

Set	Op 1	Op 2	Op 3	All
		$1\sigma n$ $(\times 10^{-4})$		
1.552	±2.4	±3.1	±1.9	±2.8
1.556	±1.3	±1.6	±1.4	±2.1
1.558	±1.2	±1.4	±1.3	±1.4
1.674	±3.1	±3.6	±2.3	±3.6
1.678	±1.1	±2.2	±0.8	±1.2
1.682	±1.9	±3.2	±2.0	±2.8
1.694	±4.3	±7.8	±3.5	±6.5

4.2 Accuracy

The accuracy of the technique was analyzed by determining the errors in the measurement of λ_m with respect to T for each glass/liquid calibration set. Systematic errors in the measurements of λ_m were observed for each calibration set. The linear fits of $\Delta\lambda_m$ to T for each set have negative slopes, and the values of $\Delta\lambda_m$ predicted by the fits are positive or close to zero at the low temperature end of each set, and negative at the high temperature end of each set, as shown in Fig. 3a. Because of the

nature of the experiment, an increase in temperature always corresponds to a decrease in λ_m, and therefore a bias associated with temperature cannot be separated from a bias associated with wavelength. Linear fits to the errors in λ_m with respect to wavelength for each set are given in Fig. 3b, with temperature listed at each end point. The linear fits all have positive slopes, and the predicted $\Delta\lambda_m$'s are negative at the short wavelength end of each set, and positive at the long wavelength end of each set. It is important to note that the calibration sets cover different ranges of wavelength, and that the errors are not associated with wavelength in an absolute sense. These data indicate that the systematic errors are not due to color sensitivity of the detector (human), as we will discuss later in the paper. The linear fits to $\Delta\lambda_m$ with respect to temperature and wavelength shown in Fig. 3 are noisy, as can be seen in Fig. 1c, and the absolute values of the slope and intercept for each set are not the same. However, the repetition of the trends in the errors for all sets is significant, and indicates that there is a bias in our measurements which correlates with temperature and wavelength.

Some possible sources of error that could produce the observed bias include those related to the heating stage (thermocouple calibration, temperature instability, temperature gradients), systematic errors in the calibration of the GIF, systematic errors in the dispersion of the liquids and/or glasses, and uncertainties in temperature coefficients. The calibrations of the heating stage, GIF, and glasses are described in the calibration section and we can eliminate these factors as possible significant contributors to the observed bias. We were concerned about possible systematic errors in the calibration of the liquids, since we were not able to measure the dispersion independently (other than the measurement of F−C). The dispersions of the liquids also change with temperature such that dn/dT is not the same at all wavelengths, although by a small amount (10^{-5}). In addition, the temperature coefficients of the glasses are not known, although they are also small (10^{-6}).

The possibility that systematic errors in the dispersions of the liquids and uncertainties in temperature coefficients were responsible for the bias observed in λ_m was tested by using a liquid and glass for which those quantities are well characterized. We measured SRM 1822, an optical glass refractive index standard, in SRM 1823I, one of the refractive index liquid standards. The dispersions of both liquid and glass are well characterized, as are the temperature coefficients of the liquid with
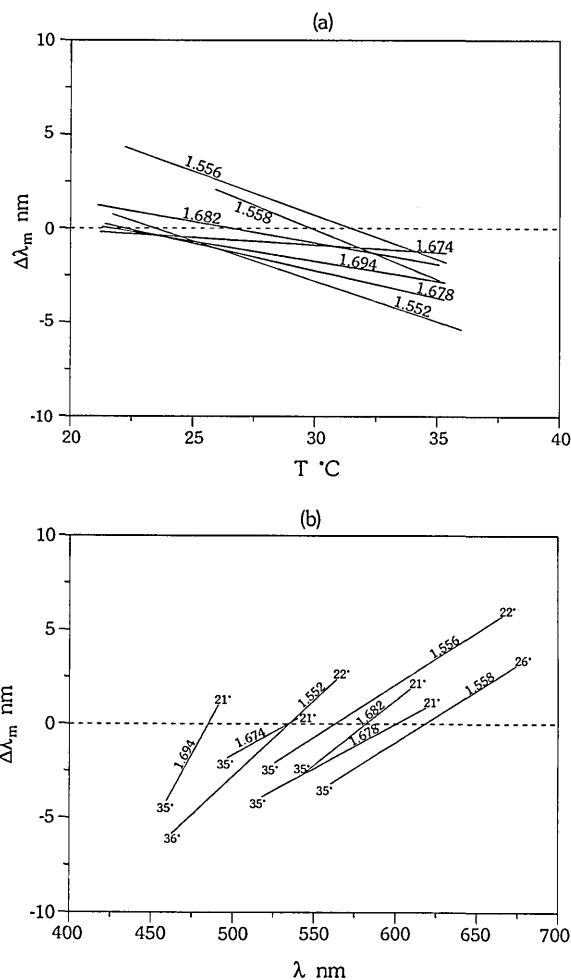
Fig. 3. Bias in λ_m: (a) with temperature and (b) with wavelength. Calibration sets identified by n_D of liquid. Lines represent least squares linear fits to $\Delta\lambda_m$ for each calibration set.

respect to wavelength. SRM 1823I is a silicone oil that is chemically and thermally stable. The refractive index of the liquid was measured using the minimum deviation technique and is certified at 10 wavelengths in the visible with an accuracy of $\pm 4 \times 10^{-5}$ at four temperatures from 20 to 80 °C. SRM 1822 is a commercial soda-lime glass that is certified for refractive index at 13 wavelengths in the visible with an accuracy of $\pm 9 \times 10^{-6}$. The temperature coefficient for SRM 1822 is not given on the certificate, however, the temperature coefficients for common optical glasses are available from the Schott catalog [13] and range from -3×10^{-6} to -5×10^{-6}, increasing with increasing refractive index. A barium crown glass (BK7) made by Schott Glass is similar in refractive index to SRM 1822, and has a temperature coefficient of -3×10^{-6}. This value was taken as the temperature coefficient for SRM 1822, although the

selection of other temperature coefficients within the range listed produced no significant difference in results.

The errors in the measurements of SRM 1822 in SRM 1823I using the narrow bandpass GIF are shown in Fig. 4, and the linear fit to the errors follows the same trend as the fits to the errors for all other calibration sets. The conclusion from these measurements is that the bias in the measurements of our seven calibration sets, as displayed in Fig. 3, is not due to uncertainties in dispersion, temperature coefficients, or liquid instability at high temperatures.

We were able to change the magnitude of the bias observed in λ_m by changing the bandpass of the GIF. We performed measurements of SRM 1822 using the narrow bandpass GIF with the slit fully open (FWHM ~30 nm), and the broad bandpass GIF, and the errors are illustrated in Fig. 4. The linear fits to the data from the GIFs have negative slopes, and the magnitude of the slope increases with increasing bandpass. The slopes of the three linear fits are significantly different from each other such that at 30 °C the 95% confidence limits for each fit comprise separate populations.
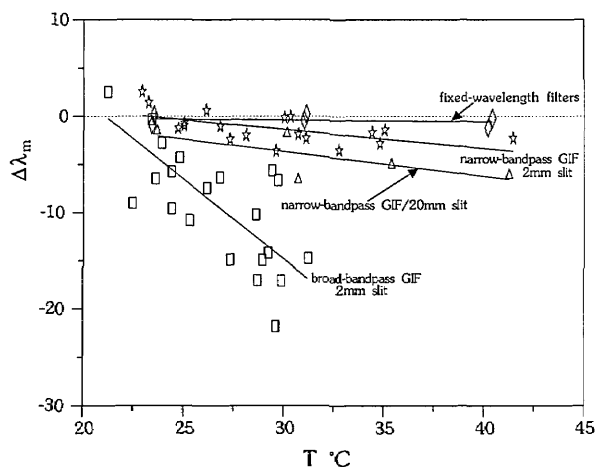
Fig. 4. Effects of bandpass on measurement bias for measurements of SRM 1822 in SRM 1823I. The broad-bandpass GIF (squares) has a 30 nm FWHM, the narrow-bandpass GIF has a 15 nm FWHM (stars) which increases to 30 nm with the slit fully open (triangles). The fixed-wavelength filters each have a 10 nm FWHM (diamonds).

We do not see a bias with temperature or wavelength when we use the fixed wavelength filters (10 nm FWHM) and vary the temperature to measure T_m (single variation technique). Measurements of SRM 1822 using the 546.1, 486.1, and 435.8 nm filters are shown in Fig. 4 [after conversion to (T, $\Delta\lambda_m$)] along with a least squares linear fit. A 95%

confidence interval of the slope of the fit includes zero, indicating that there is no significant bias for this data.

Measurements of the other calibration sets using the fixed-wavelength filters also do not exhibit any systematic errors. Due to the spacing of the transmittance peaks of the filters, we are usually limited to one or two temperature measurements for each calibration set, and therefore, we have smaller data sets than for the GIFs. However, the measurements from the fixed-wavelength filters span the full temperature and wavelength range, and we do not observe a bias with respect to temperature or wavelength. This result conflicts with that of Ref. [7] which reports the same refractive index bias for both fixed-wavelength filters and a GIF. The authors do not state the bandpass of their filters, and it is possible that the different results are due to this factor. We did not test any fixed-wavelength filters with a broader bandpass. We did test the possibility that the variation of wavelength was responsible for the bias by fixing the position of the GIF and performing a single variation measurement, as with the fixed-wavelength filters. The data collected with the GIF in a fixed position were biased in the same fashion as the data collected by varying the wavelength.

4.3 Dispersion Calculations

Given the fact that there is a bias in the measurement of λ_m, we need to determine the effect of this bias on the calculated refractive indices and fitted dispersion curves. Qualitatively, the errors in n always have the opposite sign of $\Delta\lambda_m$, therefore Δn is positive for the short wavelength—high temperature end of each calibration set, and negative for the long wavelength—low temperature end of each calibration set. We can get a general idea of the magnitude of Δn using the same procedure we used for determining the precision, namely by multiplying the error in λ_m by $(n_{gls} - n_{liq})@\lambda_m \pm 1$ nm for that calibration set. For example, from Fig. 3b we can see that at the short wavelength end of each calibration set, the predicted errors in λ_m from the linear fits range from approximately -2 nm to -6 nm, and we will assume an average error of -4 nm for discussion purposes only. If we multiply -4 nm by the largest value of $(n_{gls} - n_{liq})@\lambda_m \pm 1$ nm for each set from Table 2 (which corresponds to the short wavelength end) we see that the errors in n will range from $+2 \times 10^{-4}$ to $+1.2 \times 10^{-3}$. As discussed with reference to precision, the errors in the calculated n increase as the difference in dispersion between the glass and the liquid increase, even

for the same error in λ_m. This fundamental association stems from the assumption of the technique that the measured value lies on the liquid dispersion curve.

The ultimate goal of the measurement technique is to calculate dispersion constants for the unknown to predict the refractive index throughout the measurement range. We must, therefore, determine the errors involved in the calculation of the dispersion of the calibration glasses. The dispersion of each glass listed in Table 1 was calculated by converting the measurements from each liquid to (λ, n), combining the data from each liquid, and fitting the combined set to a Cauchy equation. In the case of glass F1152 there are three sets of data which are combined for the fit, for glass A574 there are two sets of data, and for glasses E1889 and E1442 there is only one set of data each. The (λ, n) fits to the data for each glass are shown in Fig. 5, along with the "true" (λ, n) shown by the bold line. The error in n at each λ is determined by subtracting the "true" n at each wavelength from the n predicted by the fit to the data. The Δn's thus calculated for the glasses are shown in Fig. 6. This is the same approach recommended by Su et al. (1987), who use three liquids to measure each calibration glass.

The errors in refractive index calculated using this approach now exhibit the systematic bias discussed by Refs. [6–8], particularly for glasses F1152 and A574, which are biased high for short wavelengths and biased low for long wavelengths, approaching zero error at approximately 550 nm. As discussed earlier, however, the bias does not correlate with absolute wavelength, but with the minimum and maximum wavelength of each glass/liquid calibration set. The apparent correlation of the bias with absolute wavelength for glasses F1152 and A574 results from the combination of the data from multiple liquids, and the overlap of the sets. If the data from each calibration set for glass F1152 are treated separately, we obtain the Δn_λ curves shown by the thin lines in Fig. 7, whereas if we combine the sets we obtain the Δn_λ curve shown by the bold line in Fig. 7. The error in refractive index at a particular wavelength is dependent upon the number of liquids used to measure the glass; the bias in each set of data from a given liquid will be compensated over the wavelength range where there is overlap with data from another liquid.

The dependence of Δn_λ on the number of liquids used in the calibration measurements and on the difference in dispersion between the liquid and the solid indicates that the use of such values to correct measurements of unknowns is only appropriate

when the unknown has the same dispersion as the calibration material (or the difference in dispersion between liquid and solid is the same for both) and when the same number of liquids covering the same general range of wavelengths are used. For example, if only one liquid were used to determine Δn_{560} for glass F1152, the result would be either -1×10^{-4}, 0, or $+1.5 \times 10^{-4}$, depending on the liquid used for calibration. In addition, glass E1889 would be an inappropriate calibration material to use to correct the measurements of glass A574 even though they are similar in refractive index, due to the large difference in dispersion.

The refractive index errors are also highly dependent on the filter used because of the bias associated with bandpass. Figure 8 shows the calculated errors in n for glass SRM 1822, using the data from Fig. 4. The error in refractive index for the fixed wavelength filters and the narrow bandpass GIF with the 2 mm slit is within $\pm 2 \times 10^{-4}$, but increases to approximately $+1 \times 10^{-3}$ for the broad bandpass GIF.

5. Discussion

We believe that the bias we observe in λ_m may explain the bias observed in refractive index in the previous studies [6–8]. This bias correlates with temperature and wavelength, but cannot be traced to calibration or measurement errors associated with either variable. The magnitude of the bias appears to be directly influenced by the bandpass of the interference filter. We do not observe a bias with the 10 nm FWHM fixed wavelength filters, but we observe a bias with the variable wavelength GIFs that increases with increasing bandpass. We did not test fixed wavelength filters with wider bandpasses and the question remains as to whether the GIFs themselves are a source of the bias, with the bandpass of the GIFs as an additional factor, or whether it is bandpass alone (or another variable associated with the transmission of the filter) which is the critical factor. The GIFs and the fixed wavelength filters are similar in that both are interference filters, but are dissimilar in transmission characteristics, due to the gradation in thickness of the GIF. Louisnathan et al. (1978) report a bias using fixed wavelength filters of unspecified bandpass, and it is therefore probable that the bias is not restricted to the use of GIFs. We are perplexed by the apparent association between bandpass and the observed bias, and can only suggest that the relief of the glass grains must be affected by the bandpass in some manner that biases our selection of λ_m.
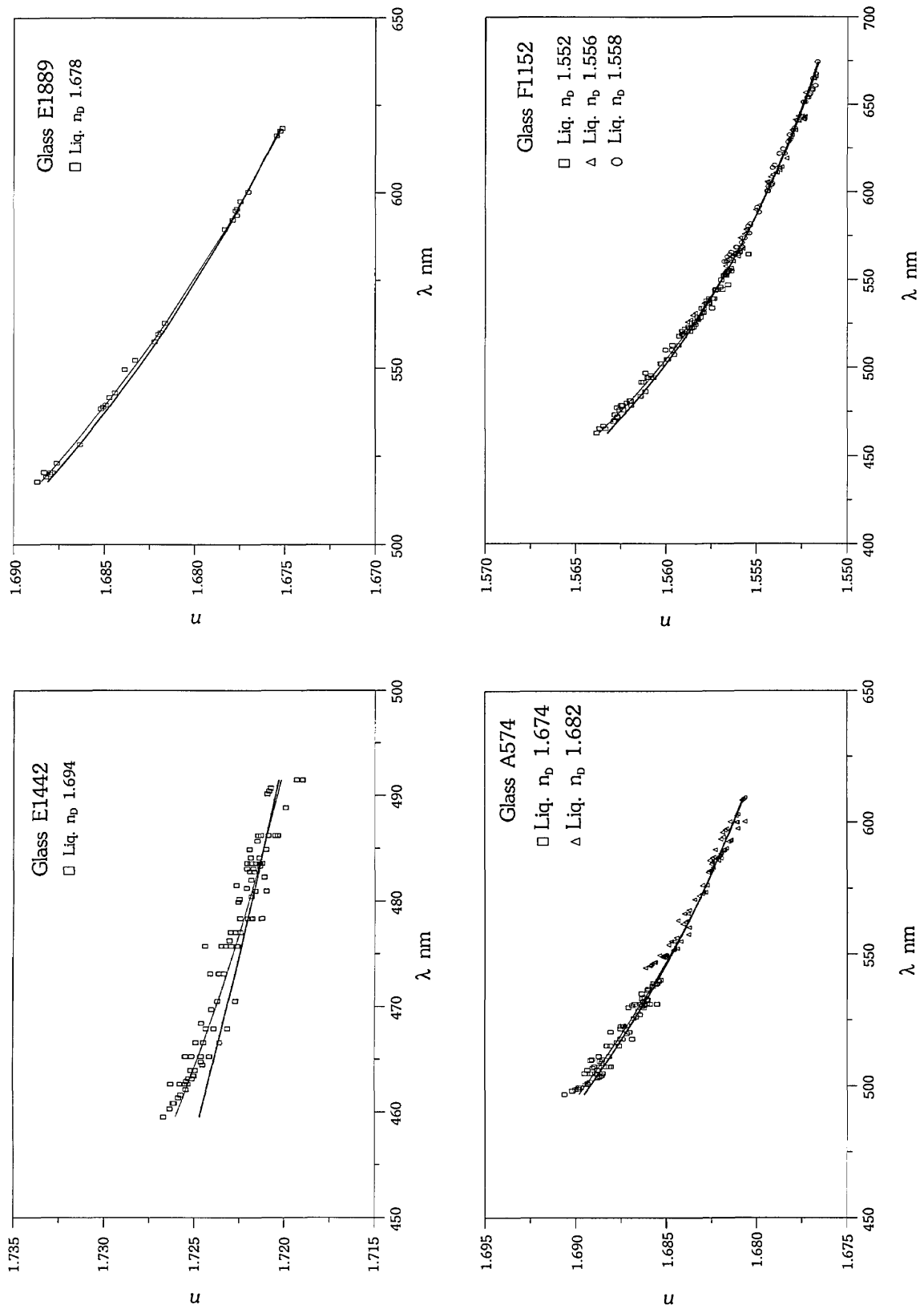
Fig. 5. Measurements of calibration glasses with fitted Cauchy (thin line) vs true (bold line).
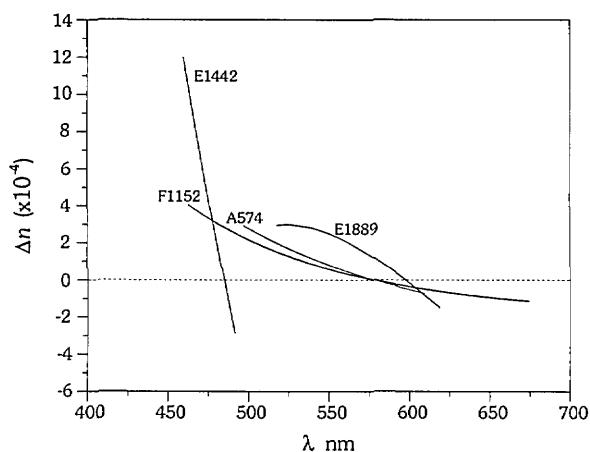
Fig. 6. Dispersion curve measurement errors for calibration glasses.
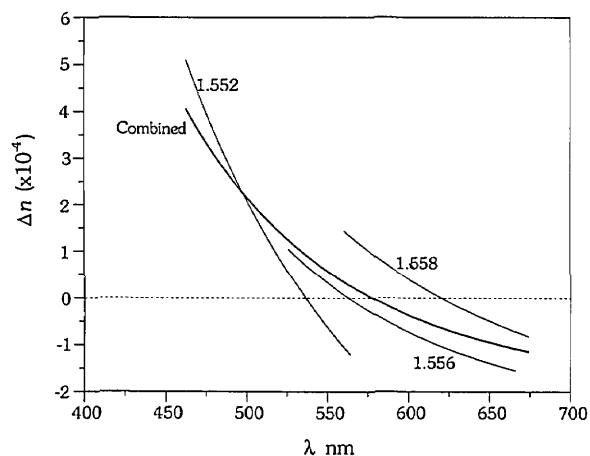
Fig. 7. Dispersion curve errors from multiple vs single liquids. Dispersion curve measurement errors for glass F1152 determined for each liquid (thin lines) and for combined dataset (bold line).
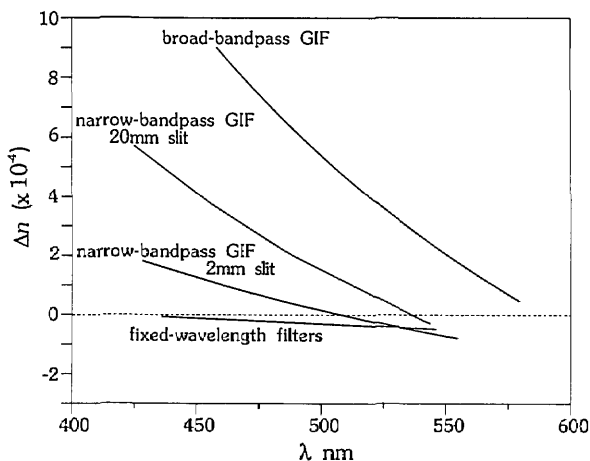
Fig. 8. Effect of bandpass on refractive index errors using data displayed in Fig. 4.

We found that even with the bias in the technique, the measurements of the glasses were acceptable (within $\pm 5 \times 10^{-4}$) with the exception of glass E1442, for which we have a maximum error of $+1.2 \times 10^{-3}$ and a precision of $\pm 6 \times 10^{-4}$. The large error in refractive index is due to the large difference in dispersion between the glass and the liquid, and not to any degradation in the actual measurements. This calibration set emphasizes the need to select liquids with the lowest dispersion possible although the choices are usually quite limited. In the initial stages of this project, when we were determining accuracy and precision in the conventional manner by analyzing the errors in refractive index with wavelength, we mistakenly thought that the precision and accuracy of the technique were dependent on the absolute refractive index of the glass as our errors increased with increasing refractive index. Only after we adopted the approach of assessing the errors in λ_m did we realize that the correlation was with the difference in dispersion between the liquid and the glass, which generally increases with increasing refractive index.

Because of the general acceptability of the double variation measurements, we felt it was appropriate to use the technique for the measurement of the asbestos reference materials. We could have used the fixed-wavelength filters and the single variation technique, for which we did not detect a bias, but our heating stage is not designed for rapid oscillation and equilibration of temperature which is necessary for efficient single variation measurements. We do not correct the measurements of our unknowns using the calibration measurements because of the strong dependence of Δn_λ on the specifics of each calibration set. We do use the calibration measurements to provide estimates of the errors in our measurements and to determine whether our variables are under control during measurement of the unknowns.

6. Conclusions

The errors in refractive index measurement using the double variation technique were determined by characterizing the accuracy and precision of measuring the matching wavelength (λ_m). The precision and accuracy of the technique in terms of the measurement of refractive index are ultimately dependent on the difference in dispersion between the solid and the liquid. The best precision possible, which in our case is 1 or 2×10^{-4}, is dependent on the operator's ability to perceive changes in

relief, and is only possible for those liquid/solid combinations where $(n_{gls}-n_{liq})@\lambda_m+1$ nm $<$ 1×10^{-4}. This limitation is based on our inability to measure λ_m with a precision better than approximately ±1 nm, which may represent a limitation of the filter.

There is a bias in our measurements of λ_m using a GIF which correlates with temperature and wavelength. The bias results in positive refractive index errors at the short wavelength — high temperature end of each dataset, and negative refractive index errors at the long wavelength — low temperature end of each dataset. (A dataset is defined as the measurements of 1 glass in 1 liquid). The bias does not correlate with absolute wavelength, and therefore does not appear to result from a relative sensitivity of the human eye. The magnitude of the bias increases with increasing bandpass, as determined by opening the exit slit of the narrow-bandpass GIF, and by using a GIF with a broader bandpass. The bias, in association with a glass and liquid with a large difference in dispersion, can result in errors in refractive index that exceed $\pm5\times10^{-4}$.

In general, our errors in refractive index using the narrow-bandpass GIF (15 nm FWHM) are within $\pm5\times10^{-4}$ throughout the visible spectrum, and within $\pm1\times10^{-4}$ at 589.3 nm, as calculated from fits to the combined data from multiple liquids. Correction factors calculated from the measurements of calibration glasses are dependent on the number of liquids used and the dispersion of both liquid and solid, and should ideally be used only when these characteristics are matched in the measurement of the unknown.

Acknowledgments

7. References

[1] NIST Certificate of Analysis SRM 1866 (1988), Bulk asbestos—common, Office of Standard Reference Materials, NIST, Gaithersburg, MD 20899.

[2] M. Fleischer, R. E. Wilcox, and J. J. Matzko, Microscopic determination of the nonopaque minerals, U.S. Geological Survey Bulletin 1627 (1984).

[3] E. C. T. Chao, The application of quantitative interference microscopy to mineralogic and petrologic investigations, Am. Mineralogist 61, 212–228 (1976).

[4] C. P. Saylor, Accuracy of microscopical methods for determining refractive index by immersion, J. Res. Natl. Bur. Stand. (U.S.) 15, 277–294 (1935).

[5] R. C. Emmons, The double variation method of refractive index determination, Am. Mineralogist 14, 414–426 (1929).

[6] F. D. Bloss, The spindle stage: Principles and practice, Cambridge University Press, Cambridge, England (1981), 340 pp.

[7] S. J. Louisnathan, F. D. Bloss, and E. J. Korda, Measurement of refractive indices and their dispersion, Am. Mineralogist 63, 394–400 (1978).

[8] S. Su, F. D Bloss, and M. Gunter, Procedures and computer programs to refine the double variation method, Am. Mineralogist 72, 1011–1013 (1987).

[9] F. A. Jenkins and H. E. White, Fundamentals of optics, McGraw-Hill, Inc., New York (1976) 746 pp.

[10] NBS Certificate of Analysis SRM 1822 (1984), Refractive index glass, Office of Standard Reference Materials, NIST, Gaithersburg, MD 20899.

[11] NBS Certificate of Analysis SRM 1823 (1976), Refractive index silicone liquids, Office of Standard Reference Materials, NIST, Gaithersburg, MD 20899.

[12] J. J. Filliben, DATAPLOT—An interactive high-level language for graphics, non-linear fitting, data analysis, and mathematics, Computer Graphics 15, (3), 119–213 (1981).

[13] Optical glass catalog No. 3111/E, 1982, Schott Glass Technologies, Inc., York Avenue, Duryea, PA 18642.

About the authors: Jennifer R. Verkouteren, Eric B. Steel, Eric S. Windsor, and John M. Phelps are all physical scientists in the Microanalysis Research Group of the Surface and Microanalysis Science Division of NIST. The National Institute of Standards and Technology is an agency of the Technology Administration, U.S. Department of Commerce.

News Briefs

General Developments

Inquiries about News Briefs, where no contact person is identified, should be referred to the Managing Editor, Journal of Research, National Institute of Standards and Technology, Administration Building, A635, Gaithersburg, MD 20899; telephone: 301/975-3572.

GAS EXPANSION PROCESS PROBES "THE GLUE OF LIFE"

A new method for measuring one of the fundamental forces of life—the weak hydrogen bonds that hold molecules together—may soon help scientists design drugs, model the chemistry of the Earth's ozone layer, and better understand the functions of the body's proteins. The process, a slit-jet supersonic expansion, expands gaseous mixtures of molecules in an area of high pressure through a narrow slit into a vacuum. This cools the gases to near absolute zero and allows the formation of weak hydrogen bonds. Infrared laser light is then used to warm and vibrate the molecules, breaking the bonds. Spectroscopic analysis of the breaking bonds provides a precise measurement of the force they possessed. Such measurements are particularly important to biochemists because hydrogen bonds hold together the two strands of the DNA molecule, the genetic material that regulates protein formation and determines an organism's characteristics.

FIRST LICENSE GRANTED FOR REMINERALIZING PROCESS

A simplified method for rapidly putting minerals into teeth moved closer to the marketplace as the result of the first patent license granted to a U.S. dental materials manufacturer to produce and market dentifrice products and chewing gum for remineralizing teeth. This means that for the first time, a toothpaste, gel, powder or chewing gum soon may be available to help prevent and repair beginning cavities, restore decalcified areas and make teeth less sensitive to hot and cold temperatures. An exclusive license with the patented remineralization process has been granted to a private company by the American Dental Association Health Foundation (ADAHF). The new products will be based on a method developed by a scientist at the ADAHF Paffenbarger Research Center at NIST. The method involves the use of amorphous calcium compounds or a carbonate solution that crystallize to form hydroxyapatite, the primary mineral in teeth and bone. A dentist at the private company, and the chief executive officer of the company, say, "This is the first major scientific and technological breakthrough in the toothpaste industry since the introduction of fluoride in the 1960s."

REPORT DESCRIBES CIRCUIT EVALUATION TECHNIQUE

NIST has created a computer procedure that ties together three software programs, creating a powerful tool for predicting the behavior of integrated circuits. The NIST method, called KEYS (for linKing softwarE to analYze waferS), links the programs SUXES (Stanford University eXtractor of modEl parameterS), SPICE (Simulation Program with Integrated Circuit Emphasis) and STAT2. SPICE predicts currents and voltages at chosen circuit nodes but requires accurate models files and input parameters. SUXES obtains model parameters and adapts to any model. And STAT2 determines correlation coefficients and generates wafer maps of selected parameters. KEYS combines the strengths of all three, allowing users to characterize individual chips, wafers or lots. KEYS is described in NIST Special Publication 400-90, available for $26 (print) or $12.50 (microfiche) prepaid from the National Technical Information Service, Springfield, VA 22161, (800) 553-6847. Order by PB 92-191220.

LOW LEAD LEVELS ASSESSED IN STUDY OF CONSUMER PAINTS

In tests of 31 different consumer paints, researchers at NIST found lead concentrations to be well below the required level (600 parts per million) as mandated by the Consumer Product Safety Commission in 1978. NIST found that in all cases, lead concentrations were less than 100 ppm. In fact, many samples had levels so low they could not be detected. This study was conducted for the U.S. Department of Housing and Urban Development as part of HUD's lead-paint abatement program. The NIST researchers tested nine oil-based paints—five exterior and four interior—and 22 water-based paints—11 exterior and 11 interior. The paints selected were a variety of quality grades and colors, and were purchased from local retail stores. Lead Concentration in Consumer Paints: A Pilot Study (NISTIR 4851) is available from the National Technical Information Service, Springfield, VA 22161, (800) 553-6847, for $17 (print) and $9 (microfiche) prepaid. Order by PB 92-213370.

CONSORTIUM PROPOSED TO IMPROVE POLYMER PROCESSING

Chemical and mechanical engineers from companies that produce engineering resins are invited to join a cooperative research and development program to improve the processing of polymer blends and alloys. The goal of the proposed research program is to use NIST measurement tools to develop the data and processing models industry needs to produce new and more economical resins. New information will enable producers to make critical in-process measurements that are not possible now. The initial project will be an in-depth study on a non-proprietary blend system. Generic technology on interfacial structure formation and characterization can be developed and applied to company-specific blends and alloy development. The NIST research tools include the small-angle neutron-scattering shear mixing apparatus at the NIST research reactor, the small-angle x-ray scattering facility, the light-scattering shear mixing apparatus, and the temperature-jump light scattering instrument for time resolved and kinetic studies. For information on the proposed 3-year program, contact Charles C. Han, B210 Polymer Building, NIST, Gaithersburg, MD 20899, (301) 975-6771.

SMALL BUSINESSES CAN HELP DEVELOP LAB AUTOMATION

NIST's Consortium on Automated Analytical Laboratory Systems, known as CAALS, recently created a new program tailored for small businesses. The consortium, a partnership of private-sector firms and government agencies, is working to advance automation in analytical chemistry by defining specifications and establishing standards that enable laboratory instruments to communicate and work together. "We wanted to get small businesses involved because of their highly innovative nature and their unique roles in the laboratory automation marketplace," explains NIST chemist and CAALS manager. The new program, known as CAALS Associates, allows small businesses to help devise specifications and standards for laboratory automation. For a $5,000 annual fee, CAALS Associates participate in quarterly workshops and receive relevant reports and newsletters. The program is also open to individuals, not-for-profit organizations, universities and trade associations. For more information, contact CAALS, A343 Chemistry Building, NIST, Gaithersburg, MD 20899, (301) 975-4142.

FEBRUARY MEETING TO FEATURE 1992 BALDRIGE WINNERS

"Quest for Excellence V," Feb. 15–17, 1993, at the Washington Hilton and Towers in Washington, DC, will be the first conference to feature presentations by all of the 1992 winners of the Malcolm Baldrige National Quality Award. Chief executive officers and other team members from the winning companies will describe in detail their quality improvement strategies and results. The conference provides a unique networking opportunity for people from across the country to exchange plans and ideas for quality and productivity improvements. It is being co-sponsored by NIST, the American Society for Quality Control and the Association for Quality and Participation. For more information about "Quest for Excellence V," call (301) 975-2036.

NIST/SBA LINK PROGRAMS FOR SMALL MANUFACTURERS

NIST and the Small Business Administration have announced a joint agreement to link SBA's business management and financial assistance

programs with NIST's national network of Manufacturing Technology Centers (MTCs). The agreement will streamline delivery of SBA-backed financing for replacing old, outdated manufacturing and design processes with new, advanced methods. The NIST MTCs assist small and mid-sized manufacturers in selecting appropriate modern technologies and processes, integrating the new technologies into the manufacturer's operation, and arranging workforce training and similar tasks. The network includes five operational centers headquartered in Cleveland, OH; Albany, NY; Columbia, SC; Ann Arbor, MI; and Overland Park, KS. Two new centers recently were announced for Los Angeles, CA, and Minneapolis, MN.

INDUSTRY, NIST TO TEST FURNITURE FIRE BLOCKERS

NIST and a private company have signed a cooperative research and development agreement to test the effectiveness of a fire-blocking barrier on the flammability of upholstered furniture. The idea is to keep a fire small by placing a fire-resistant layer between the furniture's outside fabric covering and its foam cushion. While the outside fabric may burn or char, the barrier would help prevent the sofa or chair from becoming engulfed in flames and spreading the fire. A similar technique has been used effectively in airplane seats. Researchers from the private company and NIST will run over 100 tests of samples using an industry-developed barrier, a polyurethane foam material and 15 different types of fabric. Based on the results of these tests, NIST will conduct full-scale tests on 10 items of upholstered furniture made with the barrier material. The private company will provide the materials and furniture for the tests. The project is expected to take 6 months.

UNITED STATES, CANADA AGREE ON "EQUAL TIME"

By mutual agreement, the United States and Canada have recognized each other's time scales as being equivalent at a level of 10 μs. This means that North American users of precise time information may get their time "hacks" from shortwave radio stations at either NIST or the National Research Council of Canada with equal certainty. Depending on the level of accuracy desired, users still will have to compensate for propagation delays in broadcast time signals. For very low accuracy requirements — one-tenth of a second to one second — there is little

or no need for propagation correction. NIST broadcasts time information from shortwave radio station WWV in Fort Collins, CO, and the NRC broadcasts from station CHU in Ottawa. Listeners in the eastern part of the United States may find reception of CHU's signals stronger and propagation delays shorter; likewise, time users in western Canada may find WWV to be better for their purposes. In either case, all legal requirements will be met by obtaining time information from either country.

UNITED STATES AND RUSSIA DESIGNATE STANDARDS FOCAL POINTS

The NIST National Center for Standards Code and Information (the inquiry point for the United States under the GATT Standards Code) and the Scientific Research Institute for Technical Information, Classification and Coding at GOSSTANDART, Moscow, have been designated focal points for the exchange of standards-related information between the two countries. The contact points were established by the U.S. Department of Commerce and the Russian Ministry of Foreign Economic Relations. The agreement was reached Sept. 9, 1992, at the first meeting in St. Petersburg, Russia, of the Standards Working Group of the Intergovernmental U.S./Russia Business Development Committee. At the meeting, the group recognized that harmonized standards and conformity assessment procedures, as well as technical regulations, are important for the development of commercial, economic, scientific and technical cooperation between the United States and Russia.

NEW REPORT DETAILS FEDERAL AGENCIES' ROLE IN AMPP

Announced in January 1992, the federal Advanced Materials and Processing Program represents the efforts of 10 federal agencies, the Office of Management and Budget, and the Office of Science and Technology Policy to extend U.S. leadership in materials science and engineering. The AMPP proposes a 10 percent increase for materials research and development in fiscal year 1993. A comprehensive report, Advanced Materials and Processing: The Fiscal Year 1993 Program, describes activities that will strengthen the federal materials R&D development effort and foster increased cooperation between government, industry and academia. The new report will help industry and academic

researchers locate government resources in specific areas of interest. Also listed are national user facilities operated by NIST, the Department of Energy and the National Science Foundation that are available to researchers requiring photon, neutron and magnetic sources. Copies of the report are available from Samuel J. Schneider, B309 Materials Building, NIST, Gaithersburg, MD 20899, (301) 975-5655.

1992 BALDRIGE AWARD WINNERS SET NUMEROUS FIRSTS

For the first time in its history, the Malcolm Baldrige National Quality Award has been presented to five companies in a single year. The 1992 award recipients, announced by President Bush on Oct. 14, 1992, are AT&T Network Systems Group/ Transmission Systems Business Unit (Morristown, NJ) and Texas Instruments Inc. Defense Systems & Electronics Group (Dallas, TX) in the manufacturing category; AT&T Universal Card Services (Jacksonville, FL) and The Ritz-Carlton Hotel Co. (Atlanta, GA) in the service category; and Granite Rock Co. (Watsonville, CA) in the small business category. Other 1992 milestones include the first time two divisions of the same corporation (AT&T) have won; the first time for two winners in the service category; and the first winners from the hospitality (Ritz-Carlton), construction (Granite Rock) and financial (AT&T Universal Card Services) industries. The award, managed by NIST with the active involvement of the private sector, was established by legislation in August 1987 to raise awareness about quality management and to recognize U.S. companies that have a world-class system of management, employee involvement and customer satisfaction. The five winners will be honored at a ceremony in Washington, DC, later this year.

FUTURE THERAPIES MAY "BUILD" ON ENZYME STRUCTURE

The determination of a new high-resolution structure for a liver detoxification enzyme will help scientists understand how the liver filters cancer-causing substances from the body, and may eventually lead to new cancer therapies. Scientists at the Center for Advanced Research in Biotechnology and the University of Maryland College Park describe the three-dimensional structure of glutathione S-transferase, or GST, in the Oct. 27, 1992, issue of Biochemistry. GST is a liver enzyme that protects people and animals from carcinogens encountered in the environment. Knowing the

structure of this complex molecule could enable pharmaceutical companies to design more effective chemotherapy drugs, as well as enzyme-inhibitors that would make cancer cells more susceptible to chemotherapy. Researchers cloned (produced multiple identical copies) GST from genetically engineered E. coli bacteria in order to map more than 4000 atoms and 434 amino acids that make up the protein's structure. CARB was established by NIST and the University of Maryland in 1984. Both institutes supply staff and funding to CARB's Rockville, MD laboratories.

REPORT SHOWS FEDERAL AGENCIES COMMITTED TO METRIC

The federal government's metric transition program is proceeding in a practical, orderly and evolutionary way toward the use of metric units in its business-related activities, states a summary report on the metric transition plans of 34 federal agencies. The metric system long has been the international standard of measurement. In 1988, the Congress recognized the importance of metric specifications for products in global markets by including "metric usage" provisions in the Omnibus Trade and Competitiveness Act. The amendments strengthened the Metric Conversion Act of 1975 and made each federal agency responsible for implementing metric usage in grants, contracts and other business-related activities, to the extent economically feasible, by the end of fiscal year 1992 (which ended Sept. 30, 1992). Copies of the report, Metric Transition Plans and Activities of Federal Government Agencies (NISTIR 4911), are available for $27 prepaid from the National Technical Information Service, Springfield, VA 22161, (703) 487-4650. Order by number PB 92-222249.

WORKING WITH INDUSTRY TO MEASURE PERFORMANCE

NIST has signed a cooperative research and development agreement with private industry to assess the performance of commercial automatic network analyzers used to calibrate microwave system components. ANAs have replaced many manual systems for microwave calibrations throughout government and industry. NIST pioneered the development of six-port ANAs, which enhanced ANA technology. While the six-port device is still available for NIST calibrations, it is costly for the user. NIST wants to determine whether it can achieve calibration integrity by using commercial instruments at a lower cost to customers. During the

3-year agreement, NIST will explore the feasibility of using commercial ANAs for NIST calibration services and develop procedures for validating their use in routine calibrations. For more information, contact Bob Judish, Div. 813.01, NIST, Boulder, CO 80303, (303) 497-3380.

FOURTEEN INVENTIONS NOW AVAILABLE FOR LICENSING

NIST recently announced that the following 14 government-owned inventions are now available for licensing:

- A Diffraction Device Which Detects the Bragg Condition (Docket No. 87-025);

- Apparatus for Identifying and Comparing Lattice Structures and Determining Lattice Structure Symmetries (Docket No. 88-023);

- Coprecipitation Synthesis of Precursors to Bismuth-Containing Superconductors (Docket No. 88-043);

- Microtip-Controlled Nanostructure Fabrication (Docket No. 92-024) and Multitipped Field-Emission Tool for Parallel-Process Nanostructure Fabrication (Docket No. 89-001);

- Optical Sensor for the Measurement of Molecular Orientation and Viscosity of Polymeric Materials Based on Fluorescence Radiation (Docket No. 89-015);

- Colloidal Processing Method for Coating Ceramic Reinforcing Agents (Docket No. 89-016);

- Process for Separating Azeotropic or Close-Boiling Mixtures by Use of a Composite Membrane, the Membrane and Its Process of Manufacture (Docket No. 89-028);

- Bi-Flow Expansion Device (Docket No. 89-033);

- Synthetic Dental Compositions and Bonding Methods (Docket No. 89-039);

- Aqueous Two-Phase Protein Extraction (Docket No. 90-006);

- Line-Width Micro-Bridge Test Structure (Docket No. 91-015);

- MMIC Package and Interconnect Test Fixture (Docket No. 91-016);

- Sensors for Sampling the Sizes, Geometrical Distribution and Small Particles Accumulating on a Solid Surface (Docket No. 91-017); and

- Method and Structure for Eliminating the Effects Caused by Imperfections in Electrical

Test Structures Utilized in Submicrometer Feature Metrology (Docket No. 91-020).

For technical and licensing information on these inventions, contact Bruce E. Mattson, B256 Physics Building, NIST, Gaithersburg, MD 20899, (301) 975-3084.

CRADA KICKS OFF HIGH-NITROGEN STEELS PROGRAM

A private company and NIST have established a cooperative research and development program to develop a new approach to producing stainless steels with high-nitrogen content. The NIST-patented process produces metal powders with ultrahigh nitrogen content using a gas atomization technique. This approach offers a better way of incorporating a controllable, uniform concentration of nitrogen in materials. Nitrogenated stainless steels are known to have superior strength, toughness and resistance to oxidation and corrosion. Under the program, researchers from the company will work with NIST metallurgists at the institute's powder processing laboratory. They will use the NIST metal atomizer to produce rapidly solidified stainless steel powders. The use of nitrogen gas in the process imparts the high nitrogen content in the material. The powders will be fabricated into usable parts to near-net shape by various consolidation methods. For information on the 3-year CRADA program, contact Frank Biancaniello, Metallurgy Division, B156 Industrial Building, NIST, Gaithersburg, MD 20899, (301) 975-6177.

BULLETIN SURVEYS PAPERS IN ELECTRONICS METROLOGY

Measurement programs in semiconductor microelectronics, signals and systems, electrical systems and electromagnetic interference are among those described in the Technical Progress Bulletin, now available from NIST. The quarterly bulletin covers programs that provide national reference standards, measurement methods, supporting theory and data, and traceability to national standards. It features abstracts of papers and other published works arranged by topic (with phone numbers of contacts listed). Semiconductor topics covered include silicon materials, integrated circuit test structures, photodetectors and radiation effects. Also presented are sections on waveform, cryoelectronic, antenna, noise, laser and optical fiber metrology. To receive the most recent issue or to be placed on the mailing list, write (stating profes-

sional affiliation or technical interest) to Technical Progress Bulletin, EEEL, B358 Metrology Building, NIST, Gaithersburg, MD 20899, or call (301) 975-2220.

LICENSING EXPANDED FOR SIMPLIFIED BONDING SYSTEM

Two U.S. dental materials manufacturers have been added to the list of firms authorized to use the American Dental Association Health Foundation patented bonding system for restoring teeth. The two companies now are among a group of five U.S. firms licensed to produce and market a simplified, two-step system for bonding dental resins to hard tooth tissues, both dentin and enamel. The "ultrasimplified" bonding system was developed in the ADAHF Paffenbarger Research Center at NIST. "The bonding system permits dentists to do a better job in conserving tooth structures, rebuilding badly damaged teeth, and making cosmetic improvements to front teeth," says Rafael L. Bowen, PRC director. He points out that in addition to conserving tooth structures, adhesive bonding methods increase patient comfort during and after dental procedures.

NEW EXPORT OFFICE OPENS AT NIST GAITHERSBURG

Under a unique agreement, the Commerce Department's main export promotion agency, the International Trade Administration, has established a branch office of its United States and Foreign Commercial Service at NIST's Gaithersburg, MD site. The new office provides area companies with resources on overseas marketing and facilitates collaborations with Commerce Department officers at U.S. embassies worldwide. For more information, write Stephen Hall at Room A102, Building 411, NIST, Gaithersburg, MD 20899, or call (301) 975-3904. Firms not in the Washington, DC, area can call (800) 872-8723 for the location of the nearest ITA district office.

NIST/INDUSTRY SET STANDARDS IN TELECOMMUNICATIONS

NIST has been working with the telecommunications industry to develop phase noise and synchronization standards for new optical fiber communication systems. The industry turned to NIST because of its experience in characterizing these specifications for clocks and oscillators. Since 1991,

the institute has participated in industry-wide meetings to develop standards for the proposed optical fiber network. The most recent of these, an August workshop at NIST's Boulder Laboratory, familiarized 43 industry representatives with new, NIST-developed measures for system performance that have been adopted by the U.S. and international telecommunications communities. NIST will continue to work with the industry on synchronizing and timing questions, which promise to get more severe as communication data rates increase. For details, contact Marc A. Weiss, Div. 847, NIST, Boulder, CO 80303, (303) 497-3261.

UNITED STATES LEADS WORLD IN PDE STANDARD DEVELOPMENT

A recent report by the National Initiative for Product Data Exchange states that the United States is setting the pace in an international drive to create a key information and manufacturing technology standard. The product data exchange standard will enable manufacturers to describe and exchange all useful information about a given product in computerized format. To produce a "snapshot" of the U.S. effort, NIPDE surveyed over 100 U.S. corporations, industrial consortia, standards organizations and government agencies currently participating in more than 300 product data exchange projects and activities. The survey shows that U.S. activities in PDE have an annual expenditure between $30 million and $50 million, involve personnel assignments equivalent to 200 full-time engineers and other technicians, and make up 50 to 75 percent of the worldwide activity in PDE standard development. The NIPDE Product Data Exchange Baseline Activities Report is available by writing NIPDE, B102 Radiation Physics Building, NIST, Gaithersburg, MD 20899.

NIST IGBT MODEL USED BY INDUSTRY SUBJECT OF CRADA

The generic analytical model for insulated-gate bipolar transistors (IGBTs) developed by a NIST scientist has been selected for use by a major U.S. semiconductor manufacturer and supplier of IGBTs. The model also has been adopted by an auto manufacturer in the design of electronic systems for its products. The scientist's model already has been incorporated in several widely used circuit simulation programs, and he has developed an automated parameter extraction sequence to model a variety of commercially available IGBTs. NIST and

a private company have entered into a Cooperative Research and Development Agreement to further develop the model and the automated parameter extraction sequence and to make the results available in a commercial parameter-extraction package for developers of circuit simulators. The cooperative work will facilitate the development of libraries of IGBT component models for circuit simulators.

MAGNETIZATION MEASUREMENTS APPLIED TO SUPERCONDUCTIVITY IN FIRST-TIME MEASUREMENT OF OFFSET SUSCEPTIBILITY

NIST researchers have measured the offset susceptibility of a sintered high-temperature superconductor, $YBa_2Cu_3O_7$. Such a sintered superconductor can be regarded as an assembly of weakly connected superconducting grains. The magnetic response is useful for characterization and provides information on both intrinsic (intragranular) and coupling (intergranular) components. The offset susceptibility is a new aspect of superconductor magnetization which had been predicted from Fourier analysis but never before measured, largely because it is not detectable with usual pick-up coil techniques. The researchers used a cryogenic Hall-probe magnetometer, developed at NIST, to measure magnetization directly rather than by induction. The measurements are useful in gauging the appropriateness of certain critical-state models of magnetization, and the technique can be applied to magnetic materials. Often the ac and dc susceptibilities of superconductors are treated independently, with the dc susceptibility defined as the ratio of the magnetization per unit volume to the external dc magnetic field. The authors extend the definition of the dc susceptibility for excitation fields having both a dc and a time-varying component, which results in the novel offset susceptibility. The work will appear in a forthcoming issue of Physical Review B.

CERTIFICATION PLAN DEVELOPED FOR ANTENNA NEAR-FIELD SCANNING RANGES

NIST scientists have developed and documented a certification plan that when followed provides the information needed to determine if an antenna near-field planar scanning range is qualified for characterizing the performance of phased-array antennas to a given accuracy. The NIST invention and development of near-field scanning methods has led to their widespread use, especially for complex antennas having many elements in an array and to the consequent establishment of a large number of near-field ranges in the United States and abroad. NIST has assisted many U.S. organizations in developing and qualifying their ranges for the measurement of high-performance phased arrays; in addition, NIST provides calibration services for characterizing the probes used in the near-field measurements. Previously there has been no collected guidance for an organization desiring to certify a new range or to re-certify a range after modifications.

NIST scientists now have distilled their expertise in this respect and in the plan discuss important certification aspects specifically as they relate to the characterization of phased arrays and identify the many factors that must be considered and evaluated.

NIST MEASUREMENTS SHOW HIGH T_c SUPERCONDUCTOR MECHANICAL PROPERTIES ENTERING PRACTICAL RANGE FOR MAGNETS

A NIST scientist has found an order-of-magnitude increase in the strain tolerance of certain high-critical-temperature superconductors, with the implication that for the first time the mechanical properties of high T_c superconductors are entering the practical design range for magnet applications. The measurements were made using a NIST-designed apparatus that operates in the hybrid magnet facility of the MIT National Magnet Laboratory at fields up to 25 T. Using new Ag-sheathed Bi-based superconductor samples produced by non-sintering processes (such as melt processing) and supplied by private companies, the scientist found the point of irreversible strain damage in these materials could be extended up to a value of 0.6 percent from the previous value of 0.05 percent found in virtually all earlier bulk-sintered high T_c superconductors. The NIST scientist believes that in the specimens he has measured irreversible strain damage may equate to actual fracture of the superconducting material. Future development of these conductors will center on the use of ductile matrix materials and subdividing the superconductor into small filaments to achieve greater strain tolerance. The results were recently published in Applied Physics Letters.

INDUSTRY WORKSHOP ATTENDEES STRESS NEED FOR NIST CALIBRATIONS FOR NEW TRACEABILITY

A recent workshop was held at NIST on "Metrological Issues in Precision-Tolerance Manufacturing." During the workshop representatives of key U.S. discrete-part manufacturing sectors—including commercial aircraft, heavy-equipment, automobiles, engines, computers, instrumentation and microelectronics—urgently requested that NIST provide a new and higher-accuracy standard for dimensional measurements, including those for coordinate measuring machines, involute gears, small-bore microwave devices, x-ray optical surfaces, and nanometer-scale microelectronics. Among the attendees were representatives of industry, the machine tool and gear manufacturers associations, and an array of instrument and gage manufacturers. The recurring bases of needs as stated by these companies are the "new traceability" required to meet ISO-9000-type quality requirements for products to be sold both in the European Economic Community and Pacific-rim nations, and to provide fixed reference points to support development of innovative products, such as STMs with well-characterized probes and next-generation nanoelectronic fabrication machines, processes, and devices. A summary report of the workshop and NIST follow-up action plan will soon be available.

TWO NEW NIST PRECISION MEASUREMENT GRANTS AWARDED FOR FY 93

Two new $30,000 NIST Precision Measurement Grants have been awarded for fiscal year 1993. The recipients, Alex de Lozanne and Qian Niu of the University of Texas at Austin, and Thad G. Walker of the University of Wisconsin-Madison, were selected from an initial group of 34 candidates. NIST sponsors these grants to promote fundamental research in measurement science in U.S. colleges and universities, and to foster contacts between NIST scientists and researchers in the academic community actively engaged in such work.

The aim of de Lozanne and Niu's project, "Quantum Charge Pump for a Current Standard," is to conduct experimental and theoretical studies on the realization of a quantum charge pump (QCP). Novel lithographic techniques made possible by the scanning tunneling microscope will be used to pattern the two-dimensional electron gas at a GaAs-AlGaAs interface. For a 750 MHz applied bias voltage and at a temperature of 2 K, the 50 nm features of the QCP should result in a dc current of 120 pA having a precision of 1 part in 10^8.

Walker's project, "Beta-Asymmetry Experiments Using Trapped Atoms," involves optically cooling and confining via radiation pressure short-lived radioactive atoms produced by an accelerator and spin polarizing the atoms by optical pumping. This will enable a variety of beta-decay experiments to be carried out with unprecedented precision. Walker's initial experiment will be to determine the beta-asymmetry parameter for the mirror nuclear decay of potassium 37 to argon 37. This measurement will provide a precision test of the so-called standard model of particle physics.

ATOMIC ENERGY SHIFTS IN STRONG LASER FIELDS

When an atom is subject to an intense time-varying electric field (such as the electromagnetic field produced by intense laser radiation), the atomic energy levels are shifted by the external field, an effect called the light shift or ac Stark shift. A thorough understanding of these shifts is necessary to interpret results from experiments that use intense lasers to probe atomic structure or for laser-based ultrasensitive detection of isotopes. For a highly monochromatic laser not tuned to any atomic transition and for a Rydberg level with binding energy much less than the laser photon energy, theory predicts that the energy shift in the level will approach the value given by the so-called ponderomotive potential. In a Rydberg level, a single electron is in a large orbit loosely bound to the nucleus (which is embedded in the core of the remaining electrons), and this electron exhibits near-classical behavior in certain circumstances. The ponderomotive potential is simply the classical average kinetic energy a free electron gains when driven into oscillation by an external electromagnetic field.

Previous measurements of Rydberg level ac Stark shifts disagree with each other and with predictions, with recently reported values less than half the ponderomotive potential. In addition, some measurements of the energy of electrons produced in certain laser ionization experiments, which should also approach ponderomotive values, deviate significantly from the theory. No acceptable theoretical justification has been proposed to explain these apparent discrepancies.

Recently, scientists at NIST conducted experiments to determine whether these serious dis-

crepancies result from incomplete understanding of the physical principles or from experimental difficulties. Careful, systematic measurements of ac Stark shifts in high-lying levels of calcium and xenon were made using laser ionization techniques. The results are in excellent agreement with detailed theories of laser-atom interactions which predict near-ponderomotive energy shifts and suggest possible reasons for the apparently contradictory results reported by other researchers. These experiments should restore confidence in the simple picture of a Rydberg electron behaving essentially as a free electron when subject to an intense electromagnetic field with photon energy much larger than the Rydberg binding energy.

NIST ORGANIZES INTERCOMPARISON OF U.S. AND RUSSIAN ACCELERATORS USING PROTON BEAMS FOR CANCER THERAPY

Cancer therapy studies using high-energy proton beams are under way in several major medical centers in the United States, including the Harvard Cyclotron and a new dedicated medical accelerator at Loma Linda University in California. Russian medical centers, including one at the Institute for Theoretical and Experimental Physics (ITEP) in Moscow, have been investigating proton therapy for two decades. The National Cancer Institute (NCI) is studying how the Russian experience may apply to new clinical trials for the United States. NIST is collaborating with the Radiation Research Program at NCI in developing new dosimetry systems to facilitate intercomparisons between these laboratories. Preliminary work has focused on investigations of alanine-electron spin resonance (ESR) and radiochromic films for use in measuring detailed proton dose and depth-dose curves in high-energy proton beams. The initial irradiations were carried out in Moscow. Dose measurements and depth-dose profiles obtained from alanine samples read at the NIST ESR facility agreed with the ITEP values to within ±5 percent of the ITEP values for samples irradiated to 100 Gy with protons having an energy of 200 MeV. More recently measurements have been made with the Harvard Cyclotron. Accelerators at Loma Linda and in St. Petersburg will be included in the next round of measurements.

LMR SENSITIVITY ENHANCEMENT LEADS TO OBSERVATIONS OF NEW SPECTRA

A NIST scientist and a guest researcher recently have observed a number of "new" spectra of atomic and molecular species using a substantially improved laser magnetic resonance (LMR) spectro-

meter. LMR spectroscopy was invented in the late 1960s at the NIST Boulder laboratories, and there are now a number of LMR spectrometers in operation throughout the world. These systems have produced a steady stream of results, but the NIST enhancements of LMR sensitivity have resulted in a rapid succession of new observations of spectra from S, Si, Fe, Al, ^{17}O in natural abundance, and ^{16}O sub Doppler. Other measurements include the fine structure transitions in N^+ and new ground state and metastable states in OH^+.

The three instrumental improvements providing for these new results were: an increase of the magnetic field modulation frequency from 13 to 40 kHz, an improvement in the laser pump efficiency at short wavelengths, and the addition of a new intra-laser-cavity microwave discharge to the sample region. The higher modulation frequency increases the instrumental sensitivity threefold; higher pump efficiency permits three to four times more laser lines to oscillate in the 40 to 100 μm region, and the new microwave discharge cavity permits the formation of ions within the NIST far infrared LMR spectrometer for the first time.

The results represent a major advance in spectroscopy with potential applications in studies of important species in space and in the upper atmosphere.

FERROELECTRIC OXIDE THIN FILMS FOR PHOTONICS

Photonics, the interaction of light with matter, is the basis for the next generation of devices that use optical signals rather than electrical signals to transfer information. Such devices will be used in future telecommunications, optical computing, and image processing systems. Devices for switching and modulating optical signals require the development of new photonic materials. Work at NIST has focused on ferroelectric oxides, a class of materials which exhibit the strongest electro-optical responses of any material. A metallorganic chemical vapor deposition facility has been constructed for the fabrication of ferroelectric oxide thin films. Studies have focused on establishing the processing conditions for the ferroelectric oxide compound barium titanate ($BaTiO_3$), and polycrystalline thin films of this material have now been produced. Structural, electrical, and electro-optical measurements on these films will establish the effect of defects on the properties that are critical to the performance of $BaTiO_3$ thin films in future photonic devices.

NITROGENATED METAL ALLOYS VIA GAS ATOMIZATION

Researchers at NIST recently have received a patent on use of gas atomization to produce nitrogenated metal alloys with improved properties. Discussions are under way with industry to exploit this result. The enhanced properties that nitrogen can bestow on steel by substituting for carbon have long been known. However, scientists at NIST have found that substantial additional benefits are realized when nitrogenated alloy powders are produced by atomization in nitrogen gas and bulk alloys then are formed by hot isostatic pressing. These benefits include repeatable-predictable nitrogen content, elimination of hollow spheres found in other gas atomized powders, microstructural refinement, and increased homogeneity. Also, the nitrogenated alloys produced at NIST have nearly twice the ultimate strength of comparable conventionally prepared alloys. Investigations performed for process prediction and control show that the nitrogen is absorbed mainly during alloy melting instead of by gas entrapment during atomization.

NIST RESEARCHERS DOCUMENT THERMAL AGING OF FOAM INSULATION

NIST researchers have completed a 1 year study of rigid polyisocyanurate foam thermal insulation, documenting the decrease in insulating capability and change in other important properties due to exposure to elevated temperature and humidity. Foam blown insulation is used extensively throughout the building industry. It is widely acknowledged that the material ages in place and decreases in effectiveness with time. However, the extent of decrease is subject to debate and determining the "long-term thermal conductivity" to use for building design is somewhat arbitrary at present. The researchers exposed samples to five different combinations of elevated temperature and/or humidity and measured changes in thermal conductivity, mass, volume, and density at approximately 50 day intervals over the year. They determined three regimes of aging by correlating the changes in thermal conductivity with changes in density. This technique could be used in an accelerated aging test to characterize a production lot of foam over its lifetime. Additionally, by using Fourier transform infrared spectroscopy and measurements under a scanning electron microscope, they determined the mechanisms of change occurring within the foam.

NIST RECOMMENDS MOISTURE CONTROL MEASURES TO THE HOTEL-MOTEL INDUSTRY

NIST researchers have used their simulation program MOIST to determine moisture control measures for buildings located in hot humid climates. Mold and mildew is a serious problem in buildings located in southern coastal areas. The American Hotel and Motel Association estimates that mold and mildew problems cost their industry $68 million each year. During the summer, outdoor moisture enters the wall construction by diffusion and air infiltration. If the wallpaper offers a high water-vapor resistance, moisture accumulates behind it, resulting in pink and chartreuse splotches with mildew colonies emitting fungal spores which often cause unacceptable indoor air quality. Through yearly simulations in the southern coastal region, NIST found the mold and mildew problems could be avoided by specifying wallpaper with a minimum permeance, installing an exterior vapor barrier, installing an exterior air barrier, and not excessively cooling the interior space.

TEST SPECIFICATIONS FOR COBOL PUBLISHED

NIST Special Publication 500-203, Conformance Test Specifications for COBOL Intrinsic Function Module, contains test specifications for the COBOL Intrinsic Functions Module of Federal Information Processing Standard (FIPS) 21-3, Programming Language COBOL (which adopts ANSI X3.23-1985 and Addendum ANSI X3.23A-1989). The document serves as a reference model and as a user's guide for the COBOL Intrinsic Function Module Tests in the 1985 COBOL Compiler Validation System. NIST tests COBOL implementations for conformance to FIPS 21-3 to provide language processor validations in support of federal procurement requirements. Validation services also are provided for the FIPS for Ada, C, FORTRAN, MUMPS, Pascal, and Structured Query Language.

PARALLEL PROCESSING RESEARCH ADVANCES

NIST researchers used the novel technique of time-perturbation tuning (TPT) to evaluate and improve the performance of programs on multiple-instruction, multiple-data (MIMD) computer systems. TPT combines synthetic delays with statistically designed experiments (DEX) to yield an attractive new technique for MIMD program

improvement. TPT works on programs for both shared and distributed memory, and it scales well with increasing system size. Research results are contained in NISTIR 4859, Time Perturbation Tuning of MIMD Programs. The paper was presented at the Sixth International Conference on Modeling Techniques and Tools for Computer Performance Evaluation in Edinburgh, Scotland.

NIST HOSTS COMPUTER SYSTEM SECURITY AND PRIVACY ADVISORY BOARD

On Sept. 15–17, NIST hosted a 3 day meeting of the Computer System Security and Privacy Advisory Board (CSSPAB) to assist in conducting a National Cryptographic Review. In March 1992, the board recommended to the Secretary of Commerce that a review be held to examine the positive and negative implications of widespread use of public and private key cryptography. Under Secretary for Technology Robert White has asked NIST to conduct the review.

At the meeting, the CSSPAB focused on identifying the topics to be addressed in the review, including the mechanics for conducting the study; identification of potential participants and organizations; methods for NIST to gather economic impact data; issues that the review should seek to resolve; and methods to avoid disclosures harmful to national security interests.

FEDERAL INFORMATION PROCESSING STANDARDS (FIPS) ACTIVITIES

NIST has proposed the reaffirmation of FIPS 46-1, Data Encryption Standard (DES), for use by federal agencies for the next 5 years. Issued in 1977 and reaffirmed in 1983 and 1987, the DES provides an algorithm to be implemented in electronic hardware devices and used for the cryptographic protection of computer data. The purpose of the current review is to assess the continued adequacy of the standard to protect federal information resources.

Also proposed is a revision to FIPS 127-1, Database Language SQL, which would adopt the draft proposed American National Standard: Database Language SQL (dpANS X3.135–199X), expected to be approved as an American National Standard later in 1992. The proposed revision provides a substantial, upward-compatible enhancement of Database Language SQL at three levels of conformance.

Finally, NIST has proposed a new FIPS for Automated Password Generator. The proposed standard specifies an algorithm to automate the generation of passwords for use in systems that require computer-generated pronounceable passwords. This proposed standard is for use in conjunction with FIPS 112, Password Usage Standard, which specifies basic security criteria for the design, implementation, and use of passwords.

NIST ELECTROMIGRATION WORK SAVES INDUSTRY $26.6 MILLION

A consulting economist has completed an impact study of the work on electromigration conducted by NIST scientists. The economist has concluded that the NIST research produced past and future savings to the electronics industry of more than $26.6 million. The cost of the research, spread over an 11 year period, was just over $1.6 million. Electromigration is a significant failure mechanism threatening the implementation of advanced fine-geometry semiconductor integrated-circuit designs. It occurs as a result of high-current densities in the thin-film metallization lines on an integrated-circuit chip. Two major types of failure are possible: breaks in a conducting line that produce an open circuit and short circuits between closely spaced lines.

The impact study surveyed 10 companies, including six of the seven largest U.S. semiconductor manufacturers. Eight of the 10 companies responded to a written questionnaire, and follow-up telephone interviews were conducted with all 10 companies. The identified savings result from an increased confidence in characterizing metallizations, reduction in time necessary to resolve measurement discrepancies between vendors and users, more efficient research and development related to the metallization process, and improved control and yield in the production of integrated circuits.

COMPANY PROMOTES SOFTWARE BASED ON NIST TESTING STRATEGIES APPROACH

A private company is promoting a new software package that incorporates the testing strategies approach developed by NIST scientists for complex, multi-state components such as high-resolution data converters. Three major U.S. semiconductor manufacturers are already working with the private company to demonstrate the benefits of the NIST approach as applied to testing of their products through the use of the software. Complex semiconductor devices require extensive testing to confirm that all functions are working as designed. Modern high-speed automated test equipment is expensive, and a few seconds more test time per part may make it impractical for a manufacturer to market the part.

The use of the NIST approach significantly reduces the number of test points required for testing an individual part beyond the reductions from all-codes testing now achieved in industry. The result is less expensive testing with the same level of reliability. For example, for a 16 bit analog-to-digital converter, heuristic methods now applied by one semiconductor manufacturer reduce the number of codes so that the time required for testing is about 30 s, still too costly given the anticipated selling price of the part. Using the NIST-based software permits testing this part in 2 s, a fully acceptable figure. Depending on the device, the number of test codes required by the NIST approach can be reduced by factors of 64 and more over the reductions achieved by the current state of the art in testing.

KERR-EFFECT DISPLAY SIMULATOR DEVELOPED

NIST scientists have developed a model that can simulate how a video flat-panel display based on an electro-optical Kerr-effect pixel would present an image and implemented the model in a computer program for the Princeton Engine videocomputer. The input of the display simulator is any video image (for example, as obtained from commercial television); the output is image-processed to reflect the performance characteristics of the flat-panel display. Through the use of the Princeton Engine, the effects of a change entered by keyboard to the value of a variable parameter of the model are displayed on a television screen instantaneously, i.e., in real time. These parameters represent critical characteristics such as contrast, brightness, gray scale, and horizontal and vertical viewing angle. This real-time display permits comparison of the original video with the processed video side-by-side on the same monitor. In addition, the program can display a plot of the intensity transfer function associated with the electro-optical media, so that the effects of parameter changes on the intensity distribution can be monitored; this curve can be displayed separately or overlaid on the image. The Kerr-effect display simulator is serving as a developmental tool for future simulators of display technologies having more complex underlying physics or for which transfer functions may be obtainable only empirically. Under development is a model for a twisted nematic liquid-crystal display, used in displays for some lap-top computers and portable television sets.

FINDING THE ELUSIVE EDGE OF AN X-RAY MASK LINE

NIST scientists are developing methods for objectively and accurately measuring the width of sub-micrometer-wide lines on the masks used in x-ray lithography. The goal of the project is to obtain a high level of agreement between theoretical and experimental image profiles of actual lines on x-ray masks. Good agreement would confirm that the theoretically determined position of the edge in the image is, in fact, its actual position. The desired width of a line would then be the distance between its theoretically determined left and right edges. Agreement achieved so far between theoretical and experimental image profiles of lines is good enough to conclude that using the theoretically determined edge position will be an improvement over using a subjectively determined edge position. Further refinements of theory and experiment are expected to bring the results to agree within experimental error.

The widths of x-ray mask lines are typically measured by using a scanning electron microscope (SEM), but electron scattering causes the edges of features smaller than several tenths of a micrometer to appear indistinct in the SEM image, with the result that the accuracy of the measurement is compromised. One of the scientists is developing a theoretical model of image formation in the SEM using as a basis proven image-modeling methodology developed earlier at NIST with respect to an analogous optical diffraction problem in the optical microscope. He is combining this approach with a Monte Carlo model of electron scattering previously developed at NIST for x-ray microanalysis applications. The scientists have designed and constructed a unique laser-interferometer controlled stage and modified a conventional SEM so that it will operate in a more easily modeled transmission mode which can be used on x-ray masks.

NOISE CANCELLATION IN UV/VISIBLE FOURIER TRANSFORM SPECTROSCOPY

NIST scientists have demonstrated a tenfold improvement of the signal-to-noise ratio (SNR) in high-resolution UV/visible Fourier Transform (FT) spectra of an analytical Inductively-Coupled Plasma (ICP), normally used for spectrochemical analysis. This is the largest known experimental SNR enhancement in broadband UV/visible FT spectroscopy, a technique that is especially susceptible to additive or multiplicative noise in the

source. The noise cancellation technique utilizes a unique optical design to remove a substantial fraction of the multiplicative noise in the ICP, even if the noise is dependent upon the emitting frequency. The resulting increased dynamic range of the ICP/FTS combination is essential for an ongoing collaborative effort with another Laboratory. The goal of this effort is to issue a new ICP spectral atlas and to provide spectroscopic data for diagnostic studies of the ICP. The noise reduction technique should also be applicable to ground-based UV/visible FTS of stars and of practical combustion systems.

ATOMIZATION CFD

A NIST scientist recently has worked with the Supersonic Inert Gas Metal Atomization (SiGMA) Consortium to implement successfully an important example of technology transfer. The objective of the SiGMA project is to characterize and demonstrate control of this industrially attractive atomization process and to disseminate both the results and the technology involved to member companies. The consortium is run by NIST Office of Intelligent Processing of Materials.

The NIST scientist has developed and disseminated to interested consortium members a sequence of computational models to analyze the gas flow field critical to atomization productivity. The latest model uses computational fluid dynamics (CFD) to describe the flow field near the atomization die.

One member of the consortium reports that a 40 percent increase in their product yields is attributable to the gas flow improvements they have made through a combination of the CFD results and associated techniques obtained via their participation in this NIST project. Several years ago, the consortium member reported that a 40-percent improvement in product yield was considered to be the maximum possible that could be obtained using atomization.

HOT-ELECTRON CASCADES IN COLD-SURFACE PHOTOCHEMISTRY

An exciting new area of photochemistry, which could have potential applications within a broad spectrum of delicate surface fabrication processes, is being led by both experimental and theoretical studies at NIST. The new hot-electron (or excited-electron) surface photochemistry is based on a mechanism in which ultraviolet laser light is directed onto a surface or interface upon which a chemical bond-making or bond-breaking reaction is to occur.

According to recent theoretical modeling by a NIST scientist photon absorption by valence electron excitation of the substrate is followed by a cascade process in which a distribution of hot electrons is produced. These electrons in turn undergo ultrafast reactive charge-transfer scattering at the surface. The highly non-equilibrium distribution of products forms rapidly compared to the time scales required for thermal chemistry. This distinguishing characteristic of hot-electron photochemistry not only opens new possibilities for the formation of metastable products but also limits heating and the consequent thermal degradation of the material.

The present theory is adapted from a model of hot-hole-induced cascades first developed at NIST for tunneling spectroscopy and from a theory of inelastic resonance scattering used to explain a broad range of surface-related phenomena (including electron-molecule scattering, quantum well tunneling, and resonant desorption of atoms and ions from surfaces). The latest results were presented in an invited talk at the workshop, "Photo-Induced Processes at the Gas-Solid Interface," sponsored by the European Science Foundation.

CITATIONS FOR ELECTRON MEAN FREE PATH PAPERS TOP 1000

A knowledge of the distance a hot electron travels in a solid before making a collision and losing energy is of utmost importance in interpreting experimental data. The surface sensitivities of most spectroscopic techniques are strongly dependent upon the electron mean free path, and knowledge of the mean free path is critical for quantitative determination of elemental compositions of materials by Auger- and photoelectron spectroscopy.

Ideally, the mean free path as a function of electron energy for a given material should be determined by experiments. Unfortunately, such experiments are subject to large errors and relatively few have been carried out. There have been no systematic experimental studies that cover a wide range of electron energies and materials.

For more than a decade a NIST scientist has developed theoretical methods to calculate electron mean free paths with increasing accuracy. Calculations of electron mean free paths have been published for a wide variety of solids and compounds at many electron energies. This work constitutes the only comprehensive study of the electron mean free path in solids and is cited widely in the scientific literature: the number of citations recently exceeded 1000.

THEORY OF "OPEN" QUANTUM COLLISIONS STIMULATES NEW EXPERIMENTS

The quantitative description of the novel physics of ultracold collisions requires completely new collision theories to describe the dissipation introduced by excited state decay during the very long time scale of the collision. Ultracold collisions are proto-types of the general phenomena of "open" quantum collisions in which energy is exchanged with the environment of the colliding system. In this case, the environment is the vacuum of the radiation field, to which the excited state decays by spontaneous emission. A new optical Bloch equation methodology, developed by a NIST scientist and a foreign collaborator has been applied to associative ionization of Na atoms in magneto-optical traps and atomic beams at low temperature. The theory predicts the change of the associative ionization rate as the collision temperature and the laser detuning and intensity are varied. Good agreement is found with the results of recent experiments at the University of Maryland, which measured the associative ionization rate as a function of laser intensity both in a magneto-optical trap at 0.3 mK and in an atomic beam at 12 mK. This demonstrates that the new methods describing "open" collisions show promise for predicting the new collision dynamics.

NIST TO CALIBRATE USDA NETWORK FOR MONITORING SOLAR ULTRAVIOLET

The U.S. Department of Agriculture (USDA) is currently establishing a national solar ultraviolet (UV) measurement network. This network is primarily charged with radiometric measurements of the solar UV-B (280-320 nm) irradiance. Current stratospheric ozone models predict that, with a loss of ozone, the UV-B irradiance will increase substantially. Since UV-B radiation can cause skin cancer and cataracts in humans and is deleterious for plants, animals, and materials, this ozone loss scenario could have severe ecological, health, and economic costs. The accurate measurement of solar UV-B irradiance requires state-of-the-art radiometry. NIST will characterize each USDA network instrument and publish the results with a detailed uncertainty analysis. NIST will also carry out a detailed UV-B instrument intercomparison at the first network site. We also are hoping to include in this intercomparison UV-B reference instruments for the NSF Antarctica program, the EPA ozone monitoring program, and other international UV-B networks.

MAGNETIC FLUX MAPPING IN HIGH-TEMPERATURE SUPERCONDUCTORS

Magnetic flux distribution is critical to performance in all applications of superconducting components. Most existing techniques for measuring magnetization yield average properties of a specimen. The few flux mapping methods currently available have limited temperature ranges, poor resolution, or no capability to operate in an applied magnetic field. A new magneto-optical measurement technique for quantitative flux mapping has been set up at NIST which overcomes these limits. This was achieved through a collaborative effort with the inventors from the Institute for Solid State Physics (Russian Academy of Sciences). The specimen is contained in a miniature cryostat wherein temperature may be controlled dynamically from 5 K to room temperature during application of a variable magnetic field. The flux distribution at the surface of the superconductor is detected using a Bi-doped garnet film overlaid on the specimen. Field strength and direction are measured at a spatial resolution approaching 1 μm. Direct, real-time observation of the flux distribution is achieved with a polarizing light optical microscope and a video recording system.

NIST HANDBOOK 146 TRANSLATED INTO JAPANESE

NIST's HAZARD I Fire Hazard Assessment Method software manuals (NIST Handbook 146) have been translated into Japanese by the Japanese Association of Fire Safety Science and Technology. The translation of this two-volume set was undertaken to allow easier utilization of HAZARD I in Japan for establishing the equivalency of unique building designs to the Building Standard Law of Japan (their national building code). Copies of the Japanese version of Handbook 146 will be made available within Japan by the association. A limited number of copies will be available from NIST for use by Japanese guest researchers and others who might be more comfortable with the Japanese text.

NIST HOLDS WORKSHOP ON ELEVATOR USE DURING FIRES

Throughout most of the world, warning signs next to elevators indicate they should not be used in fire situations. Today, elevators are not intended as means of fire egress and should not be used for fire evacuation. However, the idea of using elevators to

speed up fire evacuation and to evacuate persons with disabilities has gained considerable attention in the last few years.

A workshop on elevator use during fires was held at NIST Sept. 29. Participants included representatives of the elevator industry, building owners, fire protection engineers, and the fire service. The workshop consisted of presentations and an open discussion. A NIST scientist presented the results of a study about the feasibility and design considerations concerning elevator evacuation. Speakers presented the results of a human behavior study on elevator evacuation, and emphasized the associated training requirements and the organizational challenges. Industry concerns were also presented, indicating that the elevator code (ASME A17.1) currently allows elevators to be used for emergency evacuation of the disabled by the fire service or building employees.

During the open discussion, it was agreed that elevator evacuation is technically feasible. While many details must be worked out, it was agreed that the fire protection community should have the ability to use elevator fire evacuation as one of many tools (sprinklers, compartmentation, etc.) to protect life in new and remodeled buildings. Because elevator evacuation only for the disabled is much simpler than for the general population, it seems that the next logical step is an application of elevator evacuation for the disabled. Based on what is learned in this step, an application for the general population could follow.

NIST AND THE U.S. NUCLEAR REGULATORY COMMISSION (NRC) COLLABORATE ON SOFTWARE QUALITY ASSURANCE FOR NUCLEAR APPLICATIONS

Under an interagency agreement with the NRC, NIST examined the contents of a software quality assurance standard, ASMENQA2, written by the American Society of Mechanical Engineers specifically for the nuclear industry. NISTIR 4909, Software Quality Assurance: Documentation and Reviews, analyzes the applicability, content, and omissions of the standard and compares it with a general software quality assurance standard produced by the Institute of Electrical and Electronics Engineers. The report includes recommendations for the documentation of software systems and gives information for use in safety evaluation reviews. Many report recommendations are applicable for software quality assurance in general.

A related publication, NIST Special Publication 500-204, High Integrity Software Standards and Guidelines, presents the results of a study of standards, draft standards, and guidelines that provide requirements for the assurance of software in safety systems in nuclear power plants. The study focused on identifying the attributes necessary in a standard to provide reasonable assurance for software in nuclear systems. The report concludes with recommendations for guidance for the assurance of high-integrity systems.

NEW PUBLICATION ADDRESSES DATA MANAGEMENT REQUIREMENTS OF THE DEPARTMENT OF DEFENSE COMPUTER-AIDED ACQUISITION AND LOGISTIC SUPPORT (CALS) PROGRAM

As part of their continuing support for the CALS initiative, NIST researchers have published NISTIR 4902, Database Language SQL: Integrator of CALS Data Repositories. Previous reports to CALS identified the importance of Database Language Structured Query Language (SQL) and its distributed processing counterpart, Remote Database Access, for their ability to address a significant portion of CALS data management requirements. The new report presents the new "Object SQL" facilities proposed for inclusion in SQL3, introduces SQL abstract data types (ADTs), and discusses the benefits of "generic ADT packages" for management of application-specific objects. The document also proposes a new external repository interface that would allow integration of heterogenous, non-SQL data repositories.

NIST DEVELOPS SCORING PACKAGE FOR OPTICAL CHARACTER RECOGNITION TECHNOLOGY

NISTIR 4950, NIST Scoring Package User's Guide, Release 1.0, assists users of optical character recognition technology in evaluating and selecting the commercially available product best suited to their requirements. Application requirements germane to a specific automated character recognition problem are embodied in a representative set of referenced images. Along with image data, a referenced image has associated with it the ASCII textual information to be recognized in the image. This reference information serves as ground truth for measuring recognition performance. Images are presented to a recognition system, results are returned, and the scoring package reconciles hypothesized text with the referenced text. Accumulated statistics measure computer performance.

PROGRAMS FOR NEURAL NETWORK CALCULATIONS

Software developed by NIST will enhance the efficiency, and thus the feasibility, of industrially important systems based on neural network computations. Neural networks are an active area of research and development for numerous applications, particularly for automatic character recognition systems. For example, at least a dozen U.S. companies, several companies in Europe, and other research groups are developing optical character recognition systems for deciphering handwritten characters. The time-consuming task of "training" the neural networks has for some years been done by a method known as backpropagation. Mathematically, "training" corresponds to minimizing an error function. Backpropagation is known to be a slow method, and better methods (such as conjugate gradient methods) have been known for years, but backpropagation continues to be used.

A NIST scientist has written an easy-to-use training program using conjugate gradients, which runs from 10 to 100 times faster than backpropagation. He has made the program available to users via electronic mail. To date, over 50 copies have been distributed to users in universities, government, and industry in the United States and 11 foreign countries.

Members of the image recognition group, have used his training program as part of a state-of-the-art recognition system that correctly recognizes over 96 percent of handwritten digits.

Standard Reference Materials

NEW STANDARD SHINES FOR PRECIOUS METALS INDUSTRY

A recently created NIST standard for the precious metal rhodium will help mineral processors avoid million-dollar measurement errors and, at the same time, help the auto industry meet stringent Clean Air Act requirements. Working in collaboration with private industry, NIST scientists have prepared a rhodium solution standard. Rhodium, a silvery white metal, is used along with platinum and palladium in automobile catalytic converters. Rhodium catalyzes the conversion of nitrogen-oxide emissions to harmless nitrogen gas. Metal reclaimers had requested that NIST create a Standard Reference Material for rhodium to help

eliminate collective measurement errors amounting to $50 million on the world market. An accurate rhodium standard also will ensure that catalytic converters contain the proper amount of the metal. The NIST rhodium Standard Reference Material (SRM 3144) will be available in early 1993 from NIST's Standard Reference Materials Program, Room 204, Building 202, Gaithersburg, MD 20899, (301) 975-6776, fax: (301) 948-3730.

STANDARD REFERENCE MATERIAL 2724— SULFUR IN DISTILLATE (DIESEL) FUEL OIL

EPA proposal (54 FR 35276, Aug. 24, 1989) requires refiners to reduce the sulfur content of on-highway diesel fuel from current average levels of approximately 0.25 weight percent to levels not exceeding 0.05 weight percent, effective Oct. 1, 1993. Standard Reference Material (SRM) 2724 was developed to help industry and the U.S. government implement this new national program of diesel fuel quality control. It is intended primarily for use in the determination of total sulfur in diesel fuels or material of similar matrix. SRM 2724 will allow industrial laboratories to evaluate their test methods and calibrate their equipment that will be used to verify the compliance requirements of their products almost a year in advance of the effective date of the ruling.

SRM 2724 is a commercial "No. 2-D" distillate fuel oil as defined by the American Society for Testing and Materials. It consists of 100 mL of diesel fuel oil; the certified sulfur content is (0.0425 ± 0.0004) weight percent. This value is based on NIST's most accurate method for the determination of sulfur, isotope dilution thermal ionization mass spectrometry. In addition to the certified sulfur content, supplemental physical property data are provided to enable the analyst to better match the matrix of the SRM to that of the sample being analyzed.

Standard Reference Data

NIST STRUCTURAL CERAMICS DATABASE UPDATED

Standard Reference Database 30 contains state-of-the-art materials property data for both research and commercial grades of silicon carbides and silicon nitrides. This new version updates the documentation of data sources through 1991 and adds new mechanical and corrosion properties. Silicon

carbides and silicon nitrides are primary candidates for the manufacture of heat exchangers, ceramic engine components, sensors, and cutting tools because of their high strength, dimensional stability, chemical inertness, and wear resistance.

NIST THERMOPHYSICAL PROPERTIES OF PURE FLUIDS UPDATED

Standard Reference Database 12 is a major update of Interactive FORTRAN Programs to Calculate Thermo-physical Properties of Fluids—MIPROPS. This new update computes thermophysical properties according to the extremely accurate and wide-ranging NIST standard reference equation of state correlations to cover the range from the triple point to the critical point. Properties at the desired state points or tabular information, in the form of isochores, isobars, isotherms, and isentropes, may be displayed and saved in a file for further use. The five new fluids included in this upgrade are carbon dioxide, carbon monoxide, deuterium, normal hydrogen, and xenon. The number of thermophysical properties now has been increased to 34. This database has generated great interest in the cryogenic, aerospace, and bulk chemicals industries.

Subject Index to Volume 97

Numbers in parenthesis after the page number are the issue numbers

No. 1 January-February
No. 2 March-April
No. 3 May-June
No. 4 July-August
No. 5 September-October
No. 6 November-December

Author Index to Volume 97

Numbers in parenthesis after the volume number are the issue numbers

No. 1 January-February
No. 2 March-April
No. 3 May-June
No. 4 July-August
No. 5 September-October
No. 6 November-December

A

Acquista, N.

Atlas of the Spectrum of a Platinum/Neon Hollow-Cathode Reference Lamp in the Region 1130-4330 Å. Sansonetti, J. E., Reader, J., Sansonetti, C. J., and Acquista, N. 97(*1*), 1 (1992).

Alarie, Y.

The Development of a Standard Reference Material for Calibration of the University of Pittsburgh Smoke Toxicity Method for Assessing the Acute Inhalation Toxicity of Combustion Products. Levin, B. C., Alarie, Y., Stock, M. F., and Schiller, S. B. 97(2), 245 (1992).

Albus, J.

The NIST SPIDER, a Robot Crane. Albus, J., Bostelman, R., and Dagalakis, N. 97(*3*), 373 (1992).

B

Babić-Ivančić, V.

Precipitation and Solubility of Calcium Hydrogenurate Hexahydrate. Babić-Ivančić, V., Füredi-Milhofer, H., Brničević, N., and Marković, M. 97(*3*), 365 (1992).

Bar-on, I.

Fracture Toughness of Advanced Ceramics at Room Temperature. Quinn, G. D., Salem, J., Bar-on, I., Cho, K., Foley, M., and Fang, H. 97(*5*), 579 (1992).

Beetz, C. P.

Workshop on Characterizing Diamond Films. Feldman, A., Beetz, C. P., Drory, M., and Holly, S. 97(*3*), 387 (1992).

Belzer, B.

Optical Calibration of a Submicrometer Magnification Standard. Geist, J., Belzer, B., Miller, M. L., and Roitman, P. 97(2), 267 (1992).

Erratum: Optical Calibration of a Submicrometer Magnification Standard. Geist, J., Belzer, B., Miller, M. L., and Roitman, P. 97(*5*), 609 (1992).

Blaise, J.

Energy Levels of Neutral Platinum. Blaise, J., Vergès, J., Wyart, J.-F., and Engleman, R., Jr. 97(*1*), 213 (1992).

Energy Levels of Singly-Ionized Platinum. Blaise, J., and Wyart, J.-F. 97(*1*), 217 (1992).

Bostelman, R.

The NIST SPIDER, a Robot Crane. Albus, J., Bostelman, R., and Dagalakis, N. 97(*3*), 373 (1992).

Brničević, N.

Precipitation and Solubility of Calcium Hydrogenurate Hexahydrate. Babić-Ivančić, V., Füredi-Milhofer, H., Brničević, N., and Marković, M. 97(*3*), 365 (1992).

C

Cernyar, E. W.

System for Measuring Conditional Amplitude, Phase, or Time Distributions of Pulsating Phenomena. Van Brunt, R. J., and Cernyar, E. W. 97(*6*), 635 (1992).

Chang, S.-S.

Heat Capacity and Thermodynamic Properties of Poly(chlorotrifluoroethylene) From 2.5 to 620 K. Chang, S.-S., and Weeks, J. J. 97(*3*), 341 (1992).

Cho, K.

Fracture Toughness of Advanced Ceramics at Room Temperature. Quinn, G. D., Salem, J., Bar-on, I., Cho, K., Foley, M., and Fang, H. **97(5)**, 579 (1992).

D

Dagalakis, N.

The NIST SPIDER, a Robot Crane. Albus, J., Bostelman, R., and Dagalakis, N. **97(3)**, 373 (1992).

Di Marzio, E. A.

Workshop on Polymer Blends. Di Marzio, E. A., and Han, C. C. **97(4)**, 487 (1992).

Doiron, T. D.

Certification of NIST SRM 1962: 3 μm Diameter Polystyrene Spheres. Hartman, A. W., Doiron, T. D., and Fu, J. **97(2)**, 253 (1992).

Drory, M.

Workshop on Characterizing Diamond Films. Feldman, A., Beetz, C. P., Drory, M., and Holly, S. **97(3)**, 387 (1992).

E

Engleman, R., Jr.

Energy Levels of Neutral Platinum. Blaise, J., Vergès, J., Wyart, J.-F., and Engleman, R., Jr. **97(1)**, 213 (1992).

F

Fang, H.

Fracture Toughness of Advanced Ceramics at Room Temperature. Quinn, G. D., Salem, J., Bar-on, I., Cho, K., Foley, M., and Fang, H. **97(5)**, 579 (1992).

Feldman, A.

Workshop on Characterizing Diamond Films. Feldman, A., Beetz, C. P., Drory, M., and Holly, S. **97(3)**, 387 (1992).

Foley, M.

Fracture Toughness of Advanced Ceramics at Room Temperature. Quinn, G. D., Salem, J., Bar-on, I., Cho, K., Foley, M., and Fang, H. **97(5)**, 579 (1992).

Fu, J.

Certification of NIST SRM 1962: 3 μm Diameter Polystyrene Spheres. Hartman, A. W., Doiron, T. D., and Fu, J. **97(2)**, 253 (1992).

Füredi-Milhofer, H.

Precipitation and Solubility of Calcium Hydrogenurate Hexahydrate. Babić-Ivančić, V., Füredi-Milhofer, H., Brničević, N., and Marković, M. **97(3)**, 365 (1992).

G

Geist, J.

Optical Calibration of a Submicrometer Magnification Standard. Geist, J., Belzer, B., Miller, M. L., and Roitman, P. **97(2)**, 267 (1992).

Erratum: Optical Calibration of a Submicrometer Magnification Standard. Geist, J., Belzer, B., Miller, M. L., and Roitman, P. **97(5)**, 609 (1992).

Ghosh, R. N.

Measuring the Electron's Charge and the Fine-Structure Constant by Counting Electrons on a Capacitor. Williams, E. R., Ghosh, R. N., and Martinis, J. M. **97(2)**, 299 (1992).

H

Han, C. C.

Workshop on Polymer Blends. Di Marzio, E. A., and Han, C. C. **97(4)**, 487 (1992).

Harris, G. L.

ITS-90 Density of Water Formulation for Volumetric Standards Calibration. Jones, F. E., and Harris, G. L. **97(3)**, 335 (1992).

Hartman, A. W.

Certification of NIST SRM 1962: 3 μm Diameter Polystyrene Spheres. Hartman, A. W., Doiron, T. D., and Fu, J. **97(2)**, 253 (1992).

Holly, S.

Workshop on Characterizing Diamond Films. Feldman, A., Beetz, C. P., Drory, M., and Holly, S. **97(3)**, 387 (1992).

J

Jargon, J. A.

High Power CW Wattmeter Calibration at NIST. Rebuldela, G., and Jargon, J. A. **97(6)**, 673 (1992).

Jones, F. E.

ITS-90 Density of Water Formulation for Volumetric Standards Calibration. Jones, F. E., and Harris, G. L. **97**(*3*), 335 (1992).

K

Kim, Y.-K.

Compact Fitting Formulas for Electron-Impact Cross Sections. Kim, Y.-K. **97**(*6*), 689 (1992).

L

Levin, B. C.

The Development of a Standard Reference Material for Calibration of the University of Pittsburgh Smoke Toxicity Method for Assessing the Acute Inhalation Toxicity of Combustion Products. Levin, B. C., Alarie, Y., Stock, M. F., and Schiller, S. B. **97**(*2*), 245 (1992).

Lozier, D. W.

Symmetric Level Index Arithmetic in Simulation and Modeling. Lozier, D. W., and Turner, P. R. **97**(*4*), 471 (1992).

M

Maki, A. G.

New Wavenumber Calibration Tables From Heterodyne Frequency Measurements. Maki, A. G., and Wells, J. S. **97**(*4*), 409 (1992).

Marković, M.

Precipitation and Solubility of Calcium Hydrogenurate Hexahydrate. Babić-Ivančić, V., Füredi-Milhofer, H., Brničević, N., and Marković, M. **97**(*3*), 365 (1992).

Marks, R. B.

A General Waveguide Circuit Theory. Marks, R. B., and Williams, D. F. **97**(*5*), 533 (1992).

Martinis, J. M.

Measuring the Electron's Charge and the Fine-Structure Constant by Counting Electrons on a Capacitor. Williams, E. R., Ghosh, R. N., and Martinis, J. M. **97**(*2*), 299 (1992).

Mattingly, G. E.

The Characterization of a Piston Displacement-Type Flowmeter Calibration Facility and the Calibration and Use of Pulsed Output Type Flowmeters. Mattingly, G. E. **97**(*5*), 509 (1992).

Miller, M. L.

Optical Calibration of a Submicrometer Magnification Standard. Geist, J., Belzer, B., Miller, M. L., and Roitman, P. **97**(*2*), 267 (1992).

Erratum: Optical Calibration of a Submicrometer Magnification Standard. Geist, J., Belzer, B., Miller, M. L., and Roitman, P. **97**(*5*), 609 (1992).

Muth, L. A.

Probe-Position Error Correction in Planar Near Field Measurements at 60 GHz: Experimental Verification. Muth, L. A. **97**(*2*), 273 (1992).

N

Newton, J.

Data Administration Management Association Symposium. Newton, J. **97**(*5*), 611 (1992).

P

Phelps, J. M.

Accuracy of the Double Variation Technique of Refractive Index Measurement. Verkouteren, J. R., Steel, E. B., Windsor, E. S., and Phelps, J. M. **97**(*6*), 693 (1992).

Q

Quinn, G. D.

Fracture Toughness of Advanced Ceramics at Room Temperature. Quinn, G. D., Salem, J., Bar-on, I., Cho, K., Foley, M., and Fang, H. **97**(*5*), 579 (1992).

R

Reader, J.

Atlas of the Spectrum of a Platinum/Neon Hollow-Cathode Reference Lamp in the Region 1130–4330 Å. Sansonetti, J. E., Reader, J., Sansonetti, C. J., and Acquista, N. **97**(*1*), 1 (1992).

Rebuldela, G.

High Power CW Wattmeter Calibration at NIST. Rebuldela, G., and Jargon, J. A. 97(*6*), 673 (1992).

Roitman, P.

Optical Calibration of a Submicrometer Magnification Standard. Geist, J., Belzer, B., Miller, M. L., and Roitman, P. 97(*2*), 267 (1992).

Erratum: Optical Calibration of a Submicrometer Magnification Standard. Geist, J., Belzer, B., Miller, M. L., and Roitman, P. 97(*5*), 609 (1992).

S

Salem, J.

Fracture Toughness of Advanced Ceramics at Room Temperature. Quinn, G. D., Salem, J., Bar-on, I., Cho, K., Foley, M., and Fang, H. 97(*5*), 579 (1992).

Sansonetti, C. J.

Atlas of the Spectrum of a Platinum/Neon Hollow-Cathode Reference Lamp in the Region 1130-4330 Å. Sansonetti, J. E., Reader, J., Sansonetti, C. J., and Acquista, N. 97(*1*), 1 (1992).

Sansonetti, J. E.

Atlas of the Spectrum of a Platinum/Neon Hollow-Cathode Reference Lamp in the Region 1130-4330 Å. Sansonetti, J. E., Reader, J., Sansonetti, C. J., and Acquista, N. 97(*1*), 1 (1992).

Schiller, S. B.

The Development of a Standard Reference Material for Calibration of the University of Pittsburgh Smoke Toxicity Method for Assessing the Acute Inhalation Toxicity of Combustion Products. Levin, B. C., Alarie, Y., Stock, M. F., and Schiller, S. B. 97(*2*), 245 (1992).

Siegwarth, J. D.

Resistive Liquid-Vapor Surface Sensors for Liquid Nitrogen and Hydrogen. Siegwarth, J. D., Voth, R. O., and Snyder, S. M. 97(*5*), 563 (1992).

Snyder, S. M.

Resistive Liquid-Vapor Surface Sensors for Liquid Nitrogen and Hydrogen. Siegwarth, J. D., Voth, R. O., and Snyder, S. M. 97(*5*), 563 (1992).

Steel, E. B.

Accuracy of the Double Variation Technique of Refractive Index Measurement. Verkouteren, J. R., Steel, E. B., Windsor, E. S., and Phelps, J. M. 97(*6*), 693 (1992).

Stock, M. F.

The Development of a Standard Reference Material for Calibration of the University of Pittsburgh Smoke Toxicity Method for Assessing the Acute Inhalation Toxicity of Combustion Products. Levin, B. C., Alarie, Y., Stock, M. F., and Schiller, S. B. 97(*2*), 245 (1992).

T

Thomas, D. B.

A Radiometer for Precision Coherent Radiation Measurements. Thomas, D. B., and Zalewski, E. F. 97(*3*), 327 (1992).

Turner, P. R.

Symmetric Level Index Arithmetic in Simulation and Modeling. Lozier, D. W., and Turner, P. R. 97(*4*), 471 (1992).

V

Van Brunt, R. J.

System for Measuring Conditional Amplitude, Phase, or Time Distributions of Pulsating Phenomena. Van Brunt, R. J., and Cernyar, E. W. 97(*6*), 635 (1992).

Vergès, J.

Energy Levels of Neutral Platinum. Blaise, J., Vergès, J., Wyart, J.-F., and Engleman, R., Jr. 97(*1*), 213 (1992).

Verkouteren, J. R.

Accuracy of the Double Variation Technique of Refractive Index Measurement. Verkouteren, J. R., Steel, E. B., Windsor, E. S., and Phelps, J. M. 97(*6*), 693 (1992).

Voth, R. O.

Resistive Liquid-Vapor Surface Sensors for Liquid Nitrogen and Hydrogen. Siegwarth, J. D., Voth, R. O., and Snyder, S. M. 97(*5*), 563 (1992).

W

Weeks, J. J.

Heat Capacity and Thermodynamic Properties of Poly(chlorotrifluoroethylene) From 2.5 to 620 K. Chang, S.-S., and Weeks, J. J. 97(*3*), 341 (1992).

Wells, J. S.

New Wavenumber Calibration Tables From Heterodyne Frequency Measurements. Maki, A. G., and Wells, J. S. 97(*4*), 409 (1992).

Williams, D. F.

A General Waveguide Circuit Theory. Marks, R. B., and Williams, D. F. 97(*5*), 533 (1992).

Williams, E. R.

Measuring the Electron's Charge and the Fine-Structure Constant by Counting Electrons on a Capacitor. Williams, E. R., Ghosh, R. N., and Martinis, J. M. 97(*2*), 299 (1992).

Windsor, E. S.

ccuracy of the Double Variation Technique of Refractive Index Measurement. Verkouteren, J. R., Steel, E. B., Windsor, E. S., and Phelps, J. M. 97(*6*), 693 (1992).

Wyart, J.-F.

Energy Levels of Neutral Platinum. Blaise, J., Vergès, J., Wyart, J.-F., and Engleman, R., Jr. 97(*1*), 213 (1992).

Energy Levels of Singly-Ionized Platinum. Blaise, J., and Wyart, J.-F. 97(*1*), 217 (1992).

Z

Zalewski, E. F.

A Radiometer for Precision Coherent Radiation Measurements. Thomas, D. B., and Zalewski, E. F. 97(*3*), 327 (1992).